UNIVERSITÀ DEGLI STUDI DI CASSINO E DEL LAZIO MERIDIONALE

CORSO DI DOTTORATO IN

METODI, MODELLI E TECNOLOGIE PER L'INGEGNERIA

DIPARTIMENTO DI INGEGNERIA ELETTRICA E DELL'INFORMAZIONE

# MEASUREMENT METHODS FOR SUSTAINABLE MOBILITY

**KEERTHANA VELUSAMY**

keerthana.velusamy@unicas.it

In Partial Fulfilment of the Requirements for the Degree of PHILOSOPHIAE DOCTOR

15/04/2026

*SUPERVISOR*

Prof. Gianfranco Miele

Prof. Luigi Ferrigno

*COORDINATOR*

Prof. Fabrizio Marignetti

UNIVERSITÀ DEGLI STUDI DI CASSINO E DEL LAZIO MERIDIONALE

CORSO DI DOTTORATO IN

METODI, MODELLI E TECNOLOGIE PER L'INGEGNERIA

Date: **15/04/2026**

Author: **Keerthana Velusamy**

Title: **Measurement Methods for Sustainable Mobility**

Department: **Dipartimento di Ingegneria Elettrica e dell'Informazione**

Degree: **PHILOSOPHIAE DOCTOR**

Permission is herewith granted to university to circulate and to have copied for non-commercial purposes, at its discretion, the above title upon the request of individuals or institutions.

V. Keerthana

Signature of Author

*To my beloved parents and brother, my constant source of love, strength and courage,*

*and to God, whose grace and guidance light my path in every step I take,*

*and in loving memory of my grandparents, aunt, and uncle, whose blessings and cherished memories continue to inspire and guide me always.*

*ACKNOWLEDGEMENT*

This dissertation is not just the culmination of years of work, but a testament to the love, strength, and unwavering support of so many cherished souls in my life.

First and foremost, I would like to express my deepest gratitude ***to my dear parents***; no words can ever fully capture what I owe you. Your endless love, sacrifices, and belief in me have been my guiding light through every storm. When I faltered, you lifted me up; when I doubted, you gave me strength. This achievement stands on the foundation of your unwavering faith. Thank you for being my rock, my home, and my greatest inspiration. Thank you for always standing by me and encouraging me, even when the path seemed uncertain. This achievement is as much yours as it is mine.

***To my beloved brother,*** your presence has been a quiet but powerful source of comfort and courage. Your belief in me, even from afar, kept my heart steady. I carry you with me in every step, and your support means more than words can express. Thank you for being my emotional anchor. I am truly blessed to have you by my side.

I hold the memories of my late grandparents close to my heart. Though they are no longer with me, their love, wisdom, and blessings continue to light my path every day. Their presence gives me strength and reminds me of the roots from which I grow. To my late aunt and uncle, your kindness and encouragement have been like a warm embrace in times of uncertainty. Your faith in me has helped sustain my spirit and pushed me forward when the road seemed long.

My sincere thanks to my professors and supervisor, especially *Prof. Gianfranco Miele*, for your guidance, patience, and encouragement, which shaped my research. I am also grateful to my home university for its strong

academic foundation and support. Special thanks to the University of Lille for the enriching experience during my visit, which I will always cherish.

*To my friends,* thank you for your laughter, your support, and your unwavering belief in me. You kept me grounded and gave me strength when I needed it most.

Finally, to everyone who has shared this journey with me, through support, advice, or a kind word. I am deeply grateful. I carry your love and encouragement with me always as I step into the future.

*With sincere appreciation and heartfelt thanks,*

*- Keerthi*

## *CONTENTS*

*LIST OF FIGURES*

## ACRONYMS

| | |
|---|---|
| AAIM | Aircraft Autonomous Integrity Monitoring |
| ABAS | Aircraft-Based Augmentation System |
| ADC | Analog-to-Digital Converter |
| AI | Artificial Intelligence |
| AIEEE | Advances in Information, Electronic, and Electrical Engineering |
| AS | Anti-Spoofing |
| ASAS | African Satellite Augmentation System |
| BAC | Blood Alcohol Concentration |
| BDS | BeiDou Navigation Satellite System |
| BDSBAS | BeiDou Satellite-Augmentation System |
| BLE | Bluetooth Low Energy |
| BOC | Binary Offset Carrier |
| BPSK | Binary Phase Shift Keying |
| C/A | Coarse/Acquisition Code |
| CCTV | Closed-Circuit Television |
| C-ITS | Cooperative Intelligent Transport Systems |
| CDMA | Code Division Multiple Access |
| CNAV | Civil Navigation (GPS Navigation Message) |

| | |
|---|---|
| CNAV-2 | Civil Navigation-2 (GPS Navigation Message) |
| $CN_0$ | Carrier-to-Noise Density Ratio |
| $CO_2$ | Carbon Dioxide |
| CR | Coding Rate |
| CSS | Chirp Spread Spectrum |
| DLL | Delay Locked Loop |
| DOP | Dilution of Precision |
| DSSS | Direct Sequence Spread Spectrum |
| EC | European Commission |
| ECEF | Earth-Centred, Earth-Fixed |
| EEA | Europe Environmental Agency |
| EGNOS | European Geostationary Navigation Overlay Service |
| ESP-IDF | Espressif IoT Development Framework |
| EU | European Union |
| EU-27 | European Union (27 Member States) |
| FAA | Federal Aviation Administration |
| FD | Fault Detection |
| FDE | Fault Detection and Exclusion |
| FEC | Forward Error Correction |

| | |
|---|---|
| FLL | Frequency Locked Loop |
| FPGA | Field-Programmable Gate Array |
| GAGAN | GPS Aided GEO Augmented Navigation |
| GBAS | Ground-Based Augmentation System |
| GDOP | Geometric Dilution of Precision |
| GEO | Geostationary Earth Orbit |
| GHG | Greenhouse Gas |
| GLONASS | GLObalnaya NAvigatsionnaya Sputnikovaya Sistema |
| GNSS | Global Navigation Satellite System |
| GPS | Global Positioning System |
| GPSDO | GPS-Disciplined Oscillator |
| GUI | Graphical User Interface |
| HF | High Frequency |
| HOW | Hand-Over-Word |
| ICAO | International Civil Aviation Organisation |
| ICT | Information and Communication Technology |
| IF | Intermediate Frequency |
| IGSO | Inclined Geosynchronous Orbit |
| ILS | Instrument Landing System |

| | |
|---|---|
| INS | Inertial Navigation System |
| IoT | Internet of Things |
| IoV | Internet of Vehicles |
| ITS | Intelligent Transport System |
| IQ | In-phase and Quadrature |
| ISM | Industrial, Scientific and Medical (frequency band) |
| KAAS | Korean Augmentation Satellite System |
| KF | Kalman Filter |
| LAN | Local Area Network |
| LNA | Low Noise Amplifier |
| LNAV | Legacy Navigation |
| LOS | Line-of-Sight |
| LoRa | Long Range |
| LoRaWAN | Long Range Wide Area Network |
| LPWAN | Low Power Wide Area Network |
| LSE | Least-Squares-Estimation |
| LTE | Long Term Evolution |
| M2M | Machine-to-Machine |
| MaaS | Mobility as a Service |

| | |
|---|---|
| MCS | Master Control Station (GNSS Segment) |
| MCS | Mobile Crowd Sensing |
| MEO | Medium Earth Orbit |
| MQTT | Message Queuing Telemetry Transport |
| MSAS | Multi-functional Satellite Augmentation System |
| MSB | Most Significant Bit |
| NB-IoT | Narrowband Internet of Things |
| NCO | Numerically Controlled Oscillator |
| NI | National Instruments |
| NMEA | National Marine Electronics Association |
| $NO_2$ | Nitrogen Dioxide |
| $O_3$ | Ozone |
| OS | Operating System |
| PDOP | Position Dilution of Precision |
| PLL | Phase Locked Loop |
| PM | Particulate Matter |
| $PM_{2.5}$ | Particulate Matter $\leq$ 2.5 μm |
| $PM_{10}$ | Particulate Matter $\leq$ 10 μm |
| PNT | Position, Navigation, and Timing |

| | |
|---|---|
| PPP | Precise Point Positioning |
| PPS | Pulse Per Second |
| PRN | Pseudo-Random Noise |
| PRR | Packet Reception Rate |
| PSD | Power Spectral Density |
| PVT | Position, Velocity and Timing |
| QZSS | Quasi-Zenith Satellite System |
| RAIM | Receiver Autonomous Integrity Monitoring |
| RF | Radio Frequency |
| RHCP | Right-Hand Circular Polarisation |
| RINEX | Receiver Independent Exchange Format |
| RSSI | Received Signal Strength Indicator |
| RTCM | Radio Technical Commission for Maritime Services |
| SACCSA | South America, Central America and Caribbean Augmentation System |
| SBAS | Satellite-Based Augmentation System |
| SDCM | System for Differential Corrections and Monitoring |
| SDG | Sustainable Development Goal |
| SDR | Software Defined Radio |
| SIS | Signal-in-Space |

| | |
|---|---|
| SNR | Signal-to-Noise Ratio |
| SouthPAN | Southern Positioning Augmentation System |
| SPI | Serial Peripheral Interface |
| SPP | Single Point Positioning |
| SPS | Standard Positioning Service |
| SRx | Software Receiver (FGI-GSRx) |
| STSCS | Smart Traffic Signal Control System |
| SUMP | Sustainable Urban Mobility Planning |
| TDCP | Time Differenced Carrier Phase |
| TDCP-RAIM | Time Differenced Carrier Phase RAIM |
| TEN-T | Trans-European Transport Network |
| TLM | Telemetry |
| UART | Universal Asynchronous Receiver-Transmitter |
| UHD | USRP Hardware Driver |
| UN | United Nations |
| USB | Universal Serial Bus |
| USRP | Universal Software Radio Peripheral |
| UTM | Universal Transverse Mercator |
| UUT | Unit Under Test |

| | |
|---|---|
| V2I | Vehicle-to-Infrastructure |
| VDB | VHF Data Broadcast |
| VHF | Very High Frequency |
| VRU | Vulnerable Road User |
| WAAS | Wide Area Augmentation System |
| WAN | Wide Area Network |
| Wi-Fi | Wireless Fidelity |
| WHO | World Health Organisation |

# *ABSTRACT*

This thesis examines the role of sensing and measurement technologies in supporting smart mobility solutions, with particular emphasis on cost-effective wireless pedestrian activity monitoring and GNSS-derived velocity estimations. The motivation arises from the necessity for transportation systems that enhance safety for vulnerable road users while promoting sustainability and efficiency. Accurate data on movement and pedestrian presence are vital for Intelligent Transport Systems, especially in urban environments, where traditional infrastructure-based approaches may be costly, intrusive, or difficult to scale. Consequently, smart mobility is approached through the development and assessment of sensing techniques that enable data-driven mobility management, pedestrian-centric services, and traffic monitoring.

A central proposition of this work is that GNSS can contribute to smart mobility not solely through positioning but also via velocity estimation. The research explores fundamental principles of GNSS-based motion estimation, focusing on two methodologies: Doppler-based velocity estimation and Time-Differenced Carrier Phase velocity estimation. Although the precision and reliability of these approaches differ, both methods can collect motion-related data without extensive roadside infrastructure, making them highly appropriate for mobility systems that emphasise flexibility, scalability, and low deployment costs.

The first experimental contribution involves the metrological evaluation of GNSS receivers employed for speed measurement. To this end, a software-defined radio (SDR) technique was utilised to establish a laboratory-grade testbed that integrates software-based post-processing with raw I/Q signal capture. This setup allows for a controlled assessment of Doppler-derived velocity estimates and an in-depth analysis of the internal processing chain.

Results indicate that, even for a stationary receiver, the velocity estimate may become unstable when satellite geometry deteriorates significantly, leading to unrealistically high values. To mitigate this issue, a Tikhonov regularisation term was incorporated into the least-squares solution. The regularised formulation stabilised the otherwise ill-conditioned geometry matrix, restoring behaviour consistent with stationary conditions and demonstrating that the regularisation effectively addresses the problem. These findings underscore the importance of controlled SDR-based evaluations in understanding the reliability limits of GNSS speed estimates.

Subsequently, the research shifts focus to pedestrian-oriented applications, where GNSS measurements from smartphones are utilised to characterise waiting pedestrians at crossings. Given the stationary nature of this scenario, the true horizontal velocity is zero; thus, any non-zero estimate indicates measurement error. Two Android devices were tested concurrently under three environmental conditions: open sky, semi-urban crossing, and dense urban traffic intersection. GNSSLogger was employed to record data, which were processed offline and evaluated using a TDCP-based estimator with the RAIM-FDE algorithm. The mean predicted horizontal velocities for both devices remained close to zero across all scenarios. Furthermore, the devices were found to be metrologically compatible at a 68% confidence level. The results confirm the viability of smartphone-based TCP sensing for detecting pedestrian waiting states in real-world settings, despite minor isolated peaks attributed to cycle slips and limitations in fault exclusion at certain epochs.

Another contribution of this thesis involves the development of a low-cost IoT sensor infrastructure for pedestrian and crowd surveillance, utilising BLE scanning and MQTT communication protocols. The proposed system employs ESP32 nodes to passively detect nearby BLE advertising devices and transmit the collected counts via a lightweight telemetry pipeline. The sensing approach is designed to be straightforward, scalable, and privacy-preserving, as it relies on device counts rather than personal identifiers. The system was characterised in a controlled environment, including deployments during a university event, with time-synchronised video recordings serving as ground truth. In real-world evaluations, the BLE device counts did not directly equate to pedestrian counts; however, the two signals exhibited a strong temporal correlation.

The results of this thesis demonstrate that BLE-based crowd sensing and GNSS velocity estimation serve integral roles within smart mobility frameworks. While low-cost wireless sensors can monitor changes in pedestrian presence over time, GNSS technologies are better suited for determining location and velocity. Overall, this research demonstrates that these sensing technologies can underpin intelligent and sustainable mobility systems through practical, flexible, and low-infrastructure solutions, achieved through a combination of theoretical analysis, controlled receiver evaluations, smartphone-based experimentation, and IoT deployments.

## *CHAPTER 1*

## *INTRODUCTION TO SMART AND SUSTAINABLE MOBILITY SYSTEMS*

### 1.1 INTRODUCTION

Modern society depends on mobility, understood as people's ability to move and transport goods, for economic development, social engagement, and access to essential services. Simultaneously, transportation systems are significant contributors to global greenhouse gas (GHG) emissions, air pollution, noise pollution, and road traffic injuries, exerting particularly severe impacts in urban areas worldwide. The conflict between attaining mobility advantages and safeguarding the environment, health, safety, and equity engenders considerable concerns for policymakers and planners. It has paved the way for finding a solution that achieves the benefits without compromising the other values. This motivates researchers worldwide to find new ways to design, manage, and assess transportation systems safely.

### 1.2 EVOLUTION OF MOBILITY

Mobility has progressed from walking to animal-drawn vehicles such as carts and chariots. The Industrial Revolution introduced innovations like railways, ships, motorised road transport, and aeroplanes [1]. The 20th century saw an accelerated shift toward mass transit, heavy motorisation, aviation, and extensive global logistics, making high-speed, long-distance travel a standard part of daily life [2]. Today, mobility is shaped by rapid urbanisation, digitalisation, and other environmental factors such as pollution and road fatalities, which have led to an increased demand for efficient, safe, and low-carbon transport systems [3], [4]. As stated in the introduction, modern society relies heavily on mobility to advance development and improve people's lives. Yet, transport systems also raise concerns such as GHG emissions, pollution, and accidents, which are notably higher in urban areas [4]. This evolution illustrates how mobility has evolved from simple movement to a complex social and technological system with a significant impact on sustainability outcomes.

## 1.3 GLOBAL MOBILITY CHALLENGES

### 1.3.1 Urbanisation

Movement defines human civilisation. From ancient trade routes connecting distant villages to modern cities linking millions of lives, the ability to reach people, goods, and opportunities has always shaped societies. For most of human history, most people lived in tiny villages. However, this has undergone substantial changes over the last few centuries, particularly in recent decades, as people have shifted massively from rural to urban areas [5]. In 1950, only 30% of the world's population lived in cities. In 2007, the distribution between urban and rural areas was balanced (Figure 1.1). The world is experiencing unprecedented levels of urbanisation, with more than 58% of the world's population now living in urban areas.

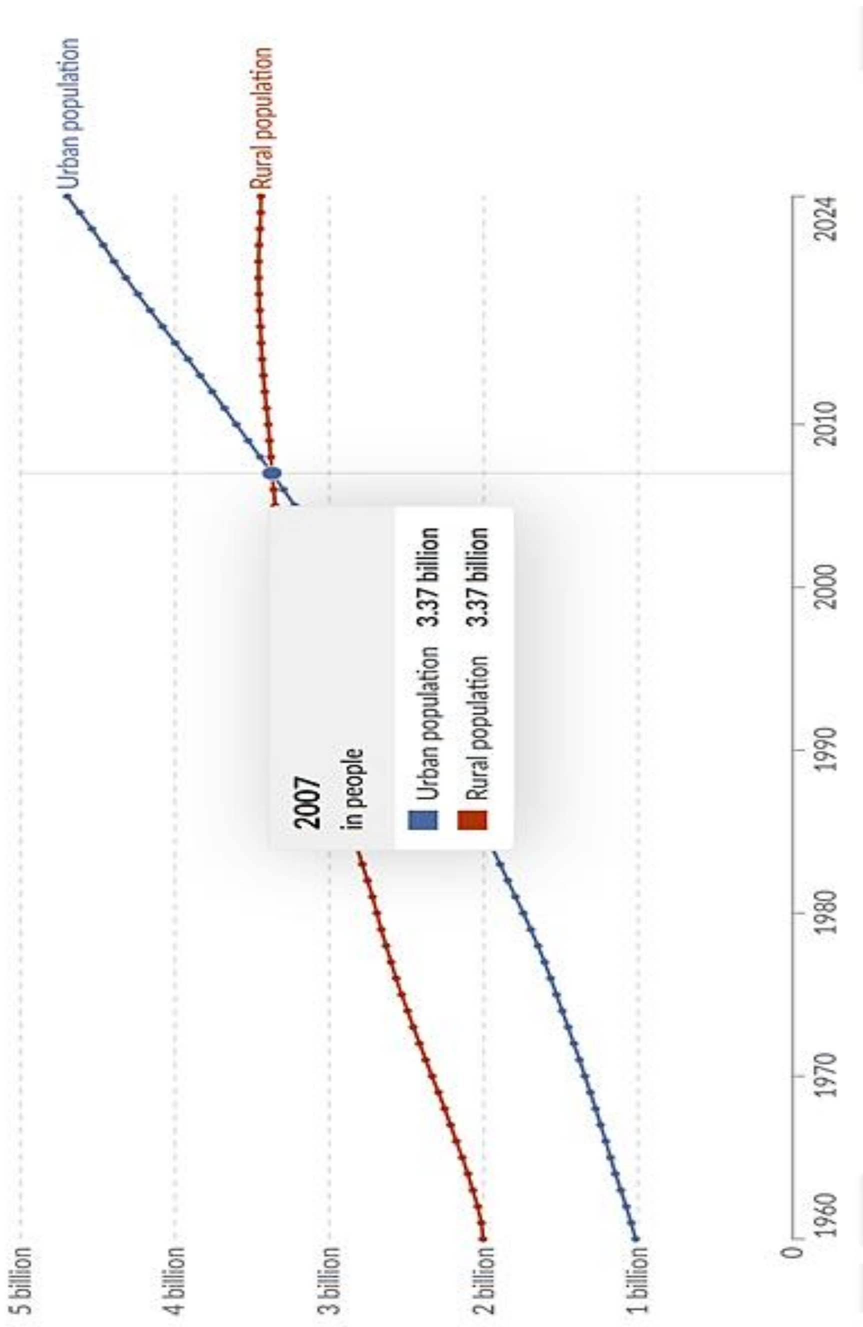


*Figure 1.1 Global urban and rural population trend from 1960 to 2024.*

*Reproduced from Our World in Data [5]*

From Figure 1.2, it is evident that North America (83%) and Latin America and the Caribbean (82%) were the regions with the highest level of urbanisation, with over four-fifths of the population residing in urban areas [6], [7]. Europe has gone further, since over 75% of its inhabitants currently reside in cities, playing a forefront role in global urbanisation. All of these are driven by economic opportunities, better living standards, and structural changes in employment away from agriculture. This is the most common pattern observed across high-income countries, and it is also increasing in middle-income countries such as China and India [5], [7].

According to the UN, by 2050, around 7 out of 10 people will live in cities (which makes up almost 68% of the global population). This results in the addition of nearly 2 billion new urban residents to the world's cities. As a result, the spatial and functional organisation of cities, and the way people move within and between them, have become central determinants of overall sustainability.

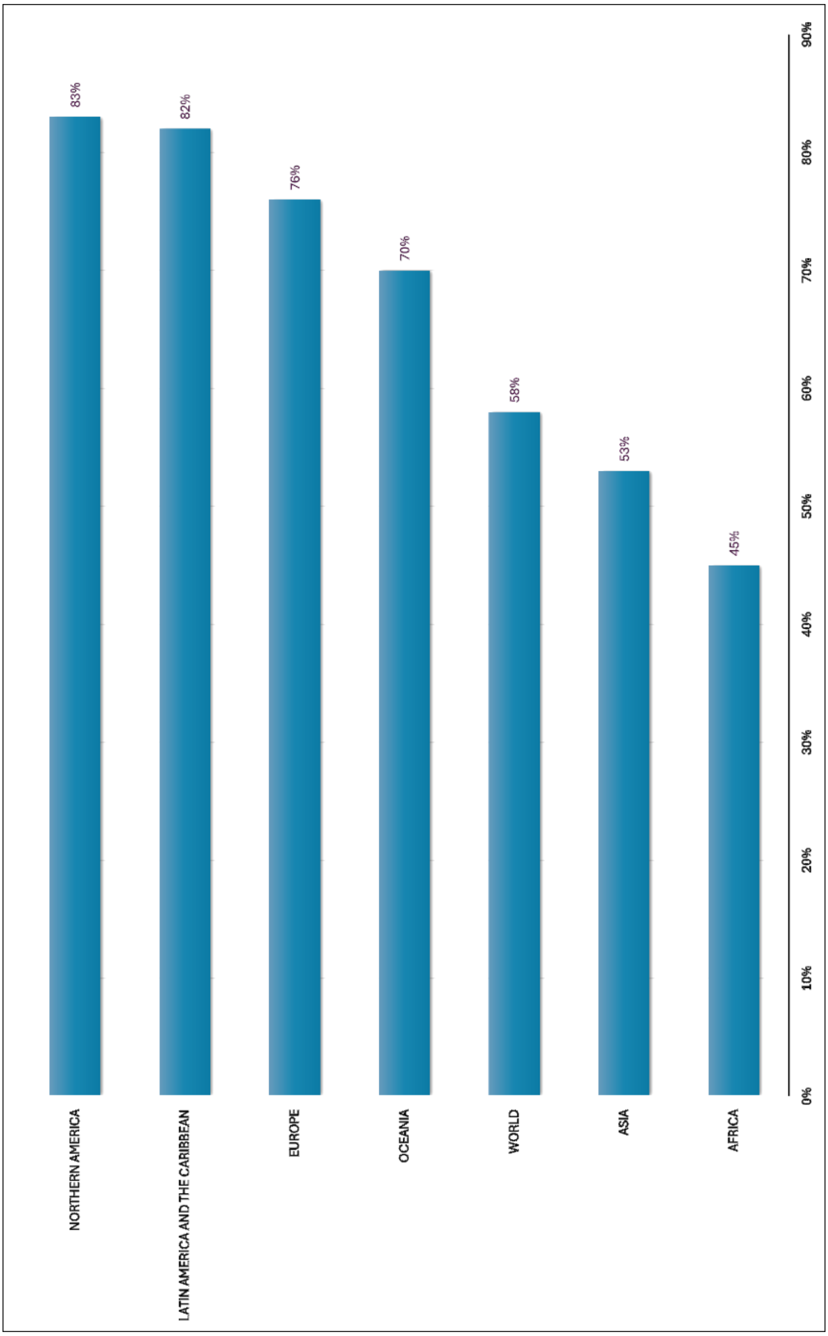


*Figure 1.2 Degree of urbanisation by continents*

*Data Source: Population Reference Bureau[6]*

### 1.3.2 Emission, congestion and environmental impacts

However, this growing urbanisation creates a significant paradox. While cities promote economic growth and enable efficient resource use, they also concentrate the demands of human mobility and the accompanying environmental externalities. Transport is one of the most essential pillars of society and the economy, allowing manufacturers to sell their products worldwide and enabling travellers to reach their leisure destinations. Transportation systems also provide access to crucial public services, such as education and healthcare, thereby enhancing the quality of life. But there is also a downside to our existing transportation network. It also has some negative impacts on the environment and human health [4].

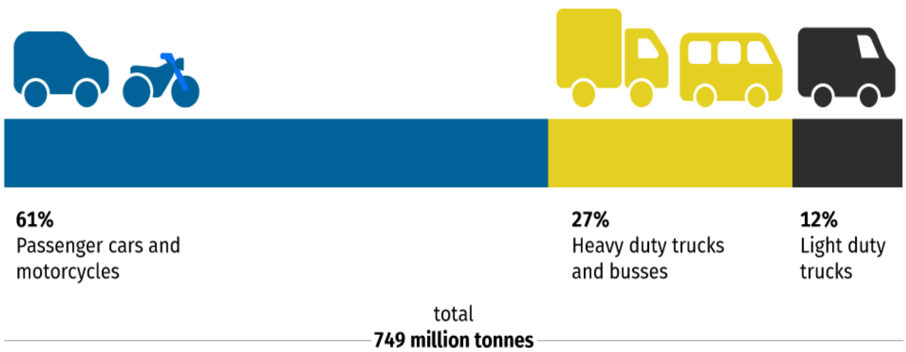


*Figure 1.3 $CO_2$ emissions by road transport*

*Reproduced from Statistisches Bundesamt, 2025*

The transportation sector, vital for moving people and goods within and between cities, has become a key concern for sustainable development. According to the European Environment Agency, transport is one of the primary sources of greenhouse gas (GHG) emissions in the European Union and is expanding more rapidly than other industries. Road transport is the most significant contributor to transport GHG emissions, accounting for roughly 73% of the EU's transport emissions, according to recent data from EEA 2023/2024 [8], [9].

Around 749 million tonnes of carbon dioxide were emitted in the EU in 2023 from the combustion of road transport fuel. Passenger cars and motorcycles accounted for the largest share of emissions (61%). Heavy-duty trucks and buses accounted for 27%, and light-duty trucks for an additional 12%. While worldwide GHG emissions from other sectors, such as energy supply and industry, are decreasing, transportation emissions remain unchanged [10]. The WHO reports that transport is a major contributor to global air pollution and energy-related $CO_2$ emissions, accounting for roughly one-quarter of global totals [10]. It is responsible for approximately 27% of energy-related $CO_2$ emissions and continues to grow, while other sectors begin to decarbonise. In the EU-27, international navigation and aviation are the second and third-largest sources of GHG emissions in the transportation sector. Rail mode, on the other hand, remains the lowest-emitting method of transportation, with emissions falling by 68.1% between 1990 and 2019. According to the EEA, existing EU policies are expected to reduce transport emissions by 14.3% in 2030 and by 37.1% in 2050 [9]. Europe aims to become climate-neutral by 2050 by reducing the GHG emissions from transport. Congestion, particularly in metropolitan areas, further contributes to various environmental impacts by increasing fuel consumption, pollutant concentration, and noise exposure. This goal cannot be reached without establishing a sustainable mobility system that relies on cleaner, more active transport options, greener fuels, and, where feasible, minimising motorised travel.

### 1.3.3 Safety of Vulnerable Road Users

Road accidents are another tragic mortality associated with transportation systems. Worldwide, approximately 1.19 million people die annually in road accidents, making it the leading cause of death among children and young adults. Between 20 and 50 million others sustain non-fatal injuries, many with disabilities. Despite owning more than 60% of the world's vehicles, low and middle-income countries account for nearly 90% of all traffic fatalities [12]. More than half of road accidents involve vulnerable road users, including pedestrians, cyclists, and motorists.

People in the working age range of 18 to 59 account for two-thirds of road injuries. Males are approximately three times more likely to be killed in car accidents than females. According to the report released by WHO, the African region has the highest death rates, while it is lowest in European nations. Crashes are not random; they are linked to particular risk factors such as speeding, alcohol and drug impairment, failure to wear helmets on motorcycles, not using seat belts and child restraints, distracted driving, poor road infrastructure, and unsafe vehicles [11].

Worldwide, powered two- and three-wheeler users make up 30% of fatalities. Vehicle occupants in four-wheelers account for 25%, pedestrians for 21%, and cyclists for 5%. The remaining 19% includes occupants of larger vehicles carrying over 10 people, heavy goods vehicles, "other" user groups, and "unknown" user types [13].

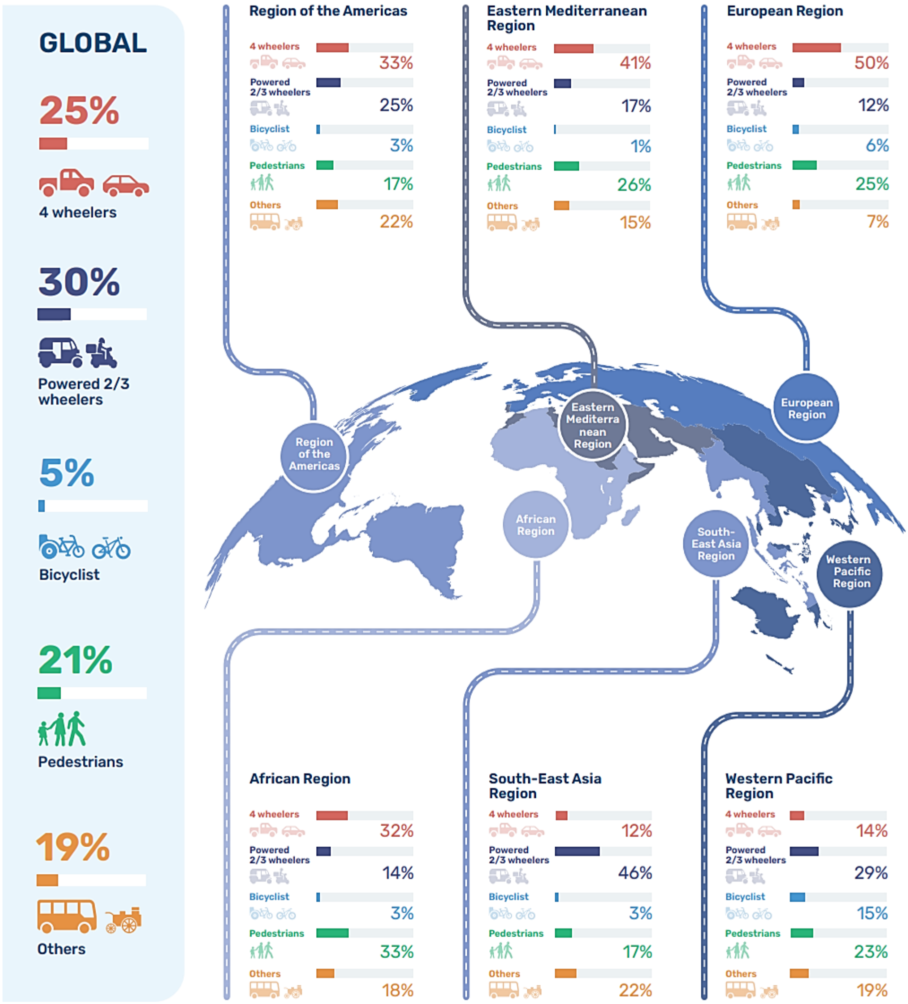


*Figure 1.4 Distribution of road traffic fatalities by user type and WHO region, 2021*

*Reproduced from the World Health Organisation, Global Road Safety Report 2021*

Road injuries can be prevented and controlled through proper preventive measures, rules, and by obeying the laws, ensuring their own and others' safety. For instance, wearing a helmet while riding a motorcycle can decrease the risk of death in a crash by 42% (Claims WHO) and cut brain injury risk by up to 74%. Seatbelt use can lower the chance of death among vehicle occupants by as much as 50%. The adoption of child restraints can result in a 71% decrease in infant deaths [12]. Ideally, road design should prioritise the safety of all users, incorporating adequate facilities for pedestrians, cyclists, and motorcyclists. Implementing features such as footpaths, cycling lanes, safe crossing points, and traffic-calming measures is vital to minimise injuries to other road users. In response, the EU has introduced eight Key performance indicators to support the target of halving the number of road deaths by 2030, including speed compliance, seatbelt use, helmet use, BAC limit compliance, mobile phone use, vehicle and infrastructure safety, and emergency response times [11]. Some nations have witnessed a decline in road traffic fatalities from 2010 to 2021, according to the WHO.

A study indicates a 2% decrease in road mortality in the EU between 2023 and 2024. To meet the EU target to reduce road deaths by half by 2030, an average annual reduction of 6% is required. The figure above shows that Luxembourg leads the way in reducing road accidents by 31%, with Malta following at 25%. However, the total number of road fatalities has remained unchanged in two countries and risen in eight, notably with Israel seeing a 22% increase and Cyprus's deaths rising by 21% [14]. Individuals can lower their accident risk by adjusting their driving speed, obeying traffic signals and rules, avoiding cycling on sidewalks, maintaining a safe distance, and using automated emergency braking systems. In this context, Europe has pledged to achieve climate neutrality by 2050 through its "Green Deal" and aims to significantly reduce road traffic deaths and serious injuries within this timeframe [15].

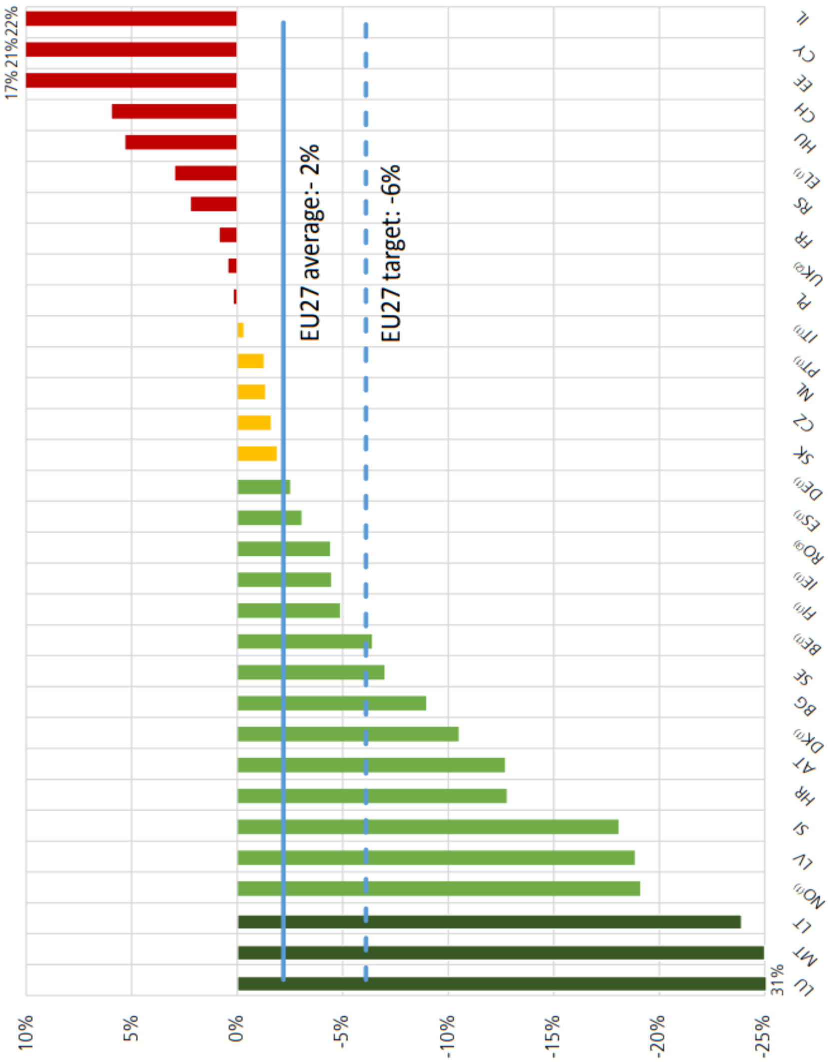


*Figure 1.5 Percentage of reduction in road fatalities between 2023 and 2024*

*Reproduced from European Transport Safety Council, 2025 Annual PIN Report*

These cannot be achieved without a fundamental transition towards sustainable mobility systems, based on cleaner and more active transport modes, cleaner fuels and vehicles, and, where possible, reducing the need for motorised travel altogether [3]. [9]. A central challenge in this transition is that high-level goals on climate, safety, equity, and efficiency must ultimately be realised through individual trips and behaviours, especially speed choice, which directly affects crash risk, fuel use, and emissions.

Traditional statistics and occasional speed checks provide only a limited understanding of actual driving behaviours across urban and rural settings, as well as of the exposure of vulnerable road users to risks at particular spots. These limitations emphasise the need for enhanced mobility sensing, especially for precise, high-resolution speed data, enabled by technologies such as GNSS. In combination with modern data analysis and the Intelligent Transportation System (ITS), such sensing enables assessment of safety and environmental impacts at fine spatial and temporal scales, supporting the design of adaptive, responsive mobility interventions [3],[9].

### 1.3.4 Air Pollution

Air pollution remains the top environmental health risk worldwide, despite regulations and technological improvements. It has been linked to thousands of preventable deaths in the European Union, despite a significant improvement in air quality. The EEA report found that between 2005 and 2023, premature deaths attributable to fine particulate matter fell by 57% [16]. Despite this, unsafe levels of air pollution resulted in a staggering 182,000 deaths in 2023. Still, 95% of urban Europeans are exposed to air pollution levels well above the WHO recommendations for air quality.


*Figure 1.6 Comparison of the share of monitoring locations in Europe meeting current EU air quality limits, future limit values for 2030, and WHO guidelines levels for PM2.5, PM10, NO2 and O3.*

According to the air quality health impact assessment, Italy suffered the most significant loss in 2023, with 43,083 deaths attributed to high PM2.5 concentrations, followed by Poland with 25,268 deaths, and Germany lost 21,640 lives. These numerical figures highlight the significant air quality challenges in densely populated cities, where road transport emissions, particularly nitrogen oxides and fine PM, remain the primary sources of ambient pollution [17]. Air pollution has reduced steadily across Europe over recent decades. Yet it remains the region's most significant environmental health risk, causing disease, lowering quality of life, and leading to preventable deaths. The EU has established air quality standards to mitigate the dangers posed by air pollution. EU air quality standards are still not fully met across Europe, despite ongoing improvements, but many countries have already achieved air quality concentrations below the new EU 2030 standards. Similarly, long-term trend data (Figure 1.7) show a decline in populations exposed to harmful pollutants since 2000, with the most significant reductions occurring after 2016.

However, to meet the new standards everywhere, and based on current progress, additional measures are needed to improve air quality, especially in cities. For some pollutants, such as benzene and cadmium, European countries are already meeting the air quality standards set by the European Union. Positive improvements have also been observed for other pollutants, such as sulphur dioxide, carbon monoxide, lead, and arsenic, with only a few monitoring stations in Europe showing values above the EU set standards. Given the levels of PM2.5 and NO2, there is a need for further progress in reducing them to meet both EU 2030 limits and WHO guidelines [16]. To reduce urban air pollution, it is essential to transform urban mobility through cleaner vehicle technologies, shifting from unnecessary private leisure transport to active and public transport, and implementing intelligent traffic management to optimise routing and reduce unnecessary congestion.

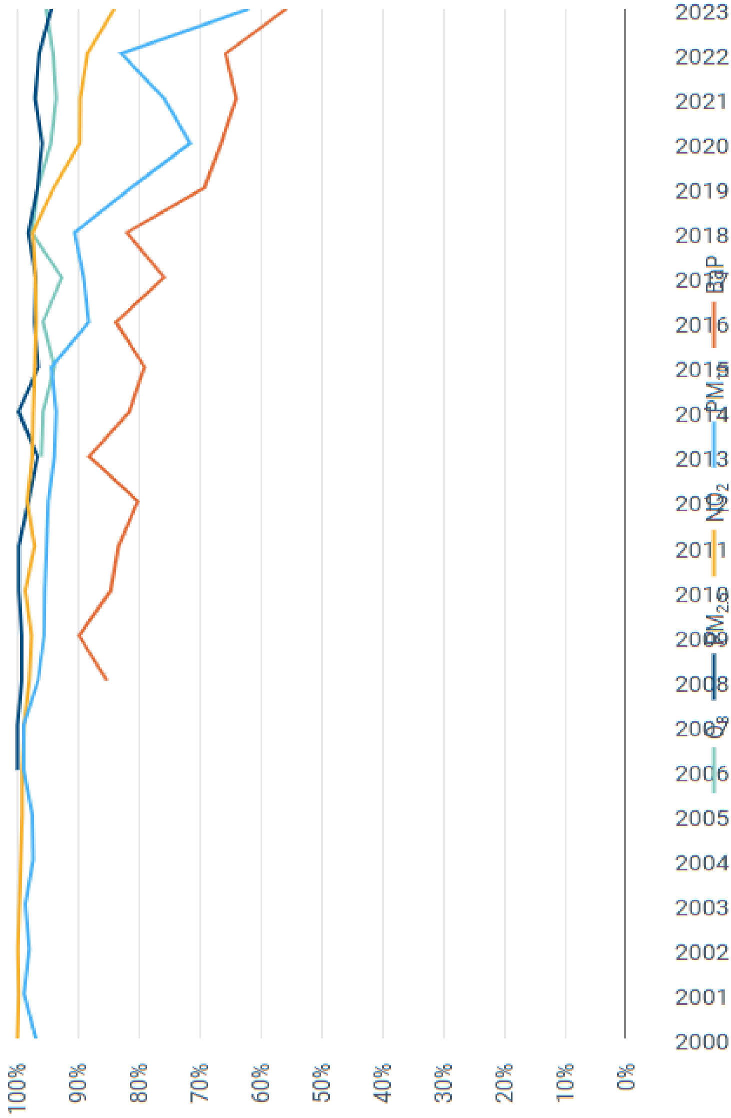


*Figure 1.7 Trends in population exposure to harmful pollutants in Europe, 2000-2023*

*Reproduced from EEA, 2025*

## 1.4 SUSTAINABLE MOBILITY

In 1992, the European Commission (EC) initially proposed the concept of "Sustainable Mobility" in the *EU Green Paper on the Impact of Transport on the Environment*, emphasising the transport sector's environmental impact [18], [19]. Later, in the United Nations' Sustainable Development Goal (SDG) framework, SDG 11, which focuses on 'Sustainable Cities and Communities' [12], introduced the concept of sustainable transport. Its objectives include improving public health, promoting social equity, strengthening urban-rural connections, enhancing societal productivity, and supporting greater economic integration.


*Figure 1.8 Sustainable Development Goals (SDGs) created by the United Nations*

### 1.4.1 SDG Goals

The 17 Sustainable Development Goals, which are a global framework for addressing poverty, inequality, environmental degradation, and sustainable development from a social, economic and ecological perspective, are shown in Figure 1.8. The goals of SDG 11 are:-

- Safe and affordable housing- basic housing services for people in slums
- Affordable and sustainable transport systems- expanding the transport systems for women, children, disabled and older people.
- Inclusive and sustainable urbanisation
- Protect the world's cultural and natural heritage- safeguard the cultural and natural heritage in the world.
- Reduce the adverse effects of natural disasters
- Reduce the environmental impact of cities
- Provide access to safe and inclusive green and public spaces
- Strong national and regional development planning
- Implement policies for inclusion, resource efficiency, and disaster risk reduction
- Support the least developed countries in sustainable and resilient building.

### 1.4.2 Traditional Mobility Vs Sustainable Mobility

Sustainable mobility, as defined by EEA, refers to the transportation system designed to limit environmental damage while maintaining safety, resource accessibility, and economic efficiency. This involves reducing the GHG emissions, improving the air quality by shifting towards active and public transport, reducing travel times, and boosting system reliability. Therefore, in addition to cleaner technology, sustainable mobility also includes long-term resilience, multimodal accessibility, and behavioural change [9]. To better understand the necessary changes, it is helpful to compare and contrast traditional mobility with sustainable mobility.

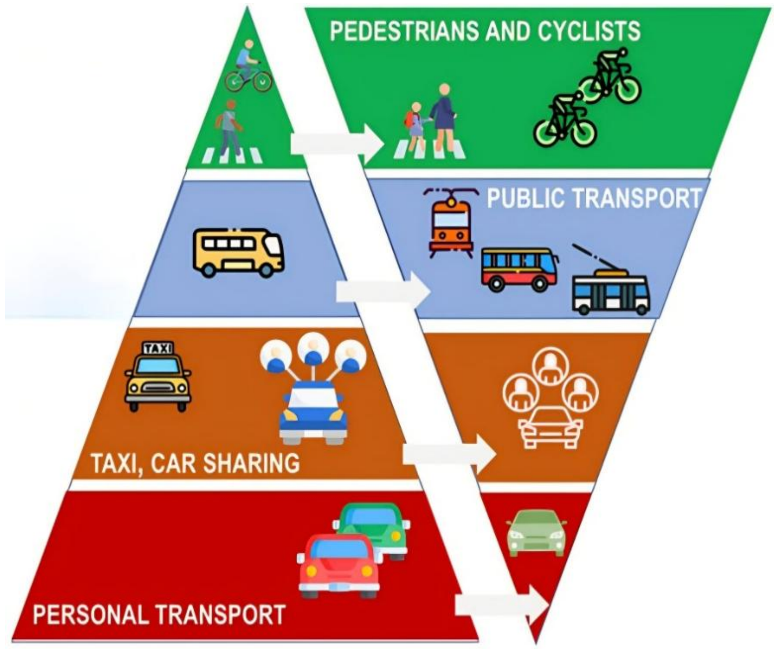


*Figure 1.9 Pyramid of Sustainable Mobility*

| ***Traditional Mobility*** | ***Sustainable Mobility*** |
|---|---|
| It is a type of transportation that uses private vehicles and consumes fossil fuels. | Sustainable mobility describes a system that satisfies society's needs while reducing environmental, social, and economic impacts. |

| | |
|---|---|
| The dominant modes of transportation are private cars and motorcycles. | It suggests using public transport, cycling, walking, shared mobility, and low-carbon-emission vehicles. |
| The environmental impact it can cause is high emissions, air pollution, and noise pollution. | It reduces emissions, provides cleaner, safer, and more accessible modes of transportation, and improves energy efficiency. |
| The social effects include inequitable access and safety risks for road-vulnerable users. | Better access and improved safety for vulnerable people groups |
| Traditional mobility makes policies only after problems arise rather than anticipating them. | SM anticipates future mobility needs and climate risks, making decisions that prioritise emission reduction, public health, and urban liveability. |
| Solutions rely on building more roads, parking, and highways. | It is based on the Sustainable Development Goals, such as SDG 3, SDG 11, and SDG 13. |

*Table 1.1 Comparison of Traditional and Sustainable Mobility*

### 1.4.3 Dimensions of Sustainable Mobility

A key feature of sustainable mobility is its multidimensional nature. It is not only about technological advances or modal shifts; it also involves a systematic change in how societies plan mobility, allocate space, and prioritise public needs. The three fundamental pillars of sustainable mobility are shown in the following figure.

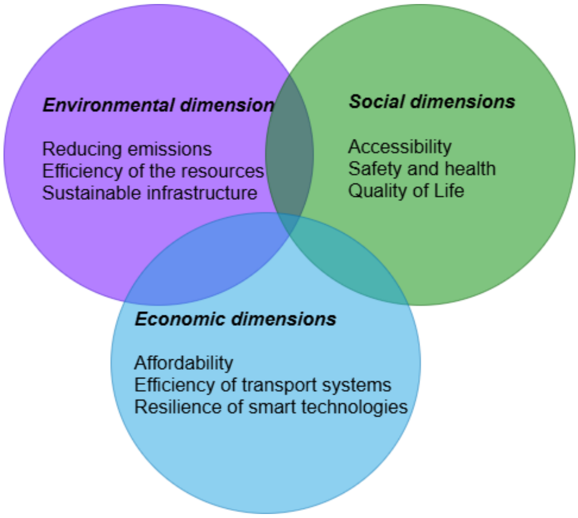


*Figure 1.10 Dimensions of sustainable mobility*

**a) Environmental Dimension:**

The primary focus of the environmental dimension is to reduce greenhouse gas (GHG) emissions, air and noise pollution, and land use. It emphasises the shift towards low-emission transport of walking, cycling, and using public transport and the incorporation of renewable energy in mobility systems [20]

**b) Social Dimension:**

It prioritises safety, accessibility, equity, and health by ensuring that all age groups, including children, older people, and people with disabilities, can access mobility services affordably and safely [20].

**c) Economic Dimension:**

The economic dimension concerns the affordability, efficiency, and productivity of transport systems. IT includes the cost-effective infrastructure improvements, reduced travel time and support for economic growth through enhanced connectivity [20].

Several frameworks add governance as a fourth dimension alongside institutions and stakeholders, as it can be an enabler of development or a barrier [20], [21].

## 1.5 POLICY TARGET TO ACHIEVE SUSTAINABLE MOBILITY

Governments and other international bodies have set a few key targets related to climate neutrality, safety, digitalisation, and modal shift to achieve innovative and sustainable mobility.

The following are the goals set by the EU Transport sector:

*a) By 2030,*

- There will be at least 30 million zero-emission vehicles on the European roads.
- 100 cities in Europe will be climate neutral.
- Europe's high-speed train counts will be doubled.
- Automated mobility will be widely adopted.
- Marine boats with zero emissions will be prepared for sale.

b) *By 2035*, Large zero-emission aircraft will also be available for the market.

c) By 2050

- Almost every automobile, van, bus, and other new heavy-duty vehicle, like a truck, will have zero emissions.
- Rail freight traffic will be doubled.
- A multimodal, fully functional Trans-European Transport Network (TEN-T) for intelligent, sustainable transport with fast connections.

The plan includes 82 initiatives across 10 main action areas (referred to as "flagships"), each with specific measures needed to achieve this goal. They are:

1. Sustainable – Transport becomes sustainable.
2. Smart – Innovation and digitisation, and the use of data and artificial intelligence for more intelligent mobility.
3. Resilient – Mobility fair and for all, transport safety, security [22], [23].

## 1.6 SUSTAINABLE MOBILITY FOR VULNERABLE ROAD USERS

Vulnerable Road users, including pedestrians, cyclists, motorcyclists, children, older people, and people with disabilities, are exposed to a share of risk in transport systems. Even though these people depend on a secure, accessible, and reasonably non-motorised mode of travel, their mobility needs are frequently disregarded as cities expand and motorisation increases. Notably, in low- and middle-income countries, where infrastructure is often car-centric and lacks facilities for safe walking and cycling, these hazards tend to rise [12].

| ***Road Users*** | ***Sustainability Issue*** | ***Solution*** |
|---|---|---|
| Private Car Owners | Causes congestion and emissions | Electric Vehicles and mixed mode of transport |
| Cyclists | Safety risks, especially at the turns | Protected infrastructure, bike lanes, E-Bike |

| | | |
|---|---|---|
| Pedestrians | Safety and accessibility | Continuous pedestrian path and speed limit of cars at the junction |

*Table 1.2 Sustainability issues and solutions for different road users*

Therefore, the design concept that can minimise the exposure to high-speed traffic, improve safety, and create surroundings where active transport is both feasible and inviting is given priority in the field of sustainable mobility. The WHO emphasises that safe infrastructure, including protected bike lanes, traffic-calming measures, and safe pedestrian crossings, can significantly reduce VRU-related injuries and fatalities [24], [25].

Promoting walking and bicycling is among the most popular sustainable policies in urban areas. These forms of movement are related to the urban environment, which must also be well redesigned. [26], [27]. Therefore, VRU-friendly infrastructure can be integrated into sustainable mobility initiatives as a means of climate action and a safety measure. A high number of walkers and cyclists is possible in cities that emphasise active mobility, such as Copenhagen, Amsterdam, and Vienna, given that their infrastructure is continuous, secure, and well-connected [28]-[32].

Therefore, it is important to design safer streets, deploy Intelligent Transport Systems (ITS) for speed management, improve data-driven monitoring of VRUs' behaviour and exposure, and incorporate safety-by-design principles into Sustainable Urban Mobility Planning (SUMP).

## 1.7 CHALLENGES OF SUSTAINABLE MOBILITY IN URBAN AREAS

Urban areas provide particular difficulties that make the transition towards sustainable mobility more difficult. These difficulties are not only technological but also reflect the complexities of protecting cultural heritage in historical areas and managing dense, diverse, dynamic networks.

Some of the main issues are discussed below:

a) Infrastructure Limitations – Many cities don't have enough space to build more transportation infrastructure. Relocating the main road space to create bike lanes, bus corridors, and pedestrian paths might create a big problem [34].

b) Different traffic patterns – Traffic in urban areas is very dynamic and affected by events, weather and the peak time of the day. This variability affects modelling, forecasting, and real-time management [33].

c) Poor quality of data – Even though there are several sensors widespread across, continuous mobility data is still lacking in most places. Especially for VRUs, it is more difficult to record their movements because traditional sensors leave large data gaps [35].

d) Privacy concerns – Sometimes, sensitive details about people's daily routines may be exposed by high-resolution mobility data, which raises concerns around data regulation, permission and monitoring.

e) Monitoring the VRUs – Traditional traffic monitoring systems do not sufficiently measure bikes, pedestrians, or other micro-mobility users.

So, there is a need for high-resolution sensing, including GNSS, inertial sensors, to precisely record their speeds and interactions.

f) Protecting the cultural heritage – Because of the conservation rules that prioritise the preservation of architectural integrity and authenticity of historical areas, the installation of technologies in historical places is severely limited.

Smart mobility measures such as adaptive traffic control, dynamic speed regulation, and safety alerts require real-time data. Communication and network technologies such as Wi-Fi, LTE, 5G, LoRa WAN, and Global Navigation Systems (GNSS) such as GPS, Glonass, and Galileo, along with cost-effective sensing hardware and computational platforms, directly address this issue by enabling continuous, scalable, low-power, and low-cost monitoring.

## 1.8 SMART MOBILITY

The term "Smart Mobility" refers to the integration of digital technologies, including sensors, networking, data analytics, and intelligent infrastructure, that improve responsiveness, efficiency, and a human-centric approach for transportation networks. Modern technologies such as Intelligent Transport Systems, electric and autonomous vehicles, and Mobility as a Service (MaaS) support sustainability and low-carbon emissions, making transportation both smart and environmentally friendly [36]-[38].

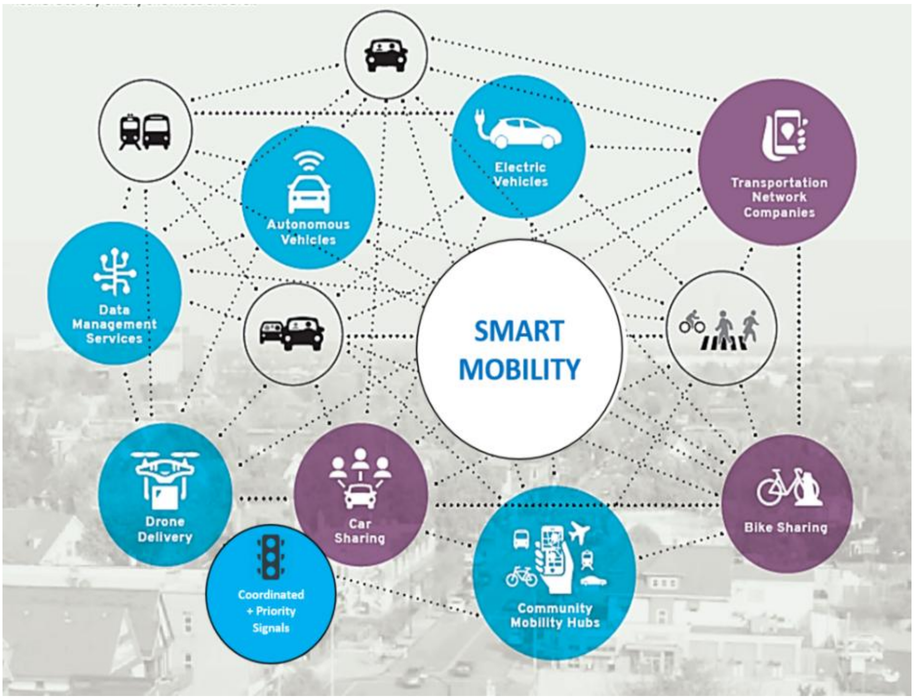


*Figure 1.11 Conceptual representation of a smart mobility system*

Mobility-as-a-Service (MaaS) means combining public transport, bike-sharing, carpooling, and micro-mobility into a single digital platform (see Figure 1.12). In smart mobility, intelligent safety measures and automation are essential. Technologies such as adaptive traffic signals, connected vehicle alerts, pedestrian detection, and automated braking systems enhance safety and efficiency by enabling vehicles and infrastructure to communicate faster than humans. Thus, smart mobility enhances the transportation environment through digital technologies and infrastructure design, making streets and people safer.

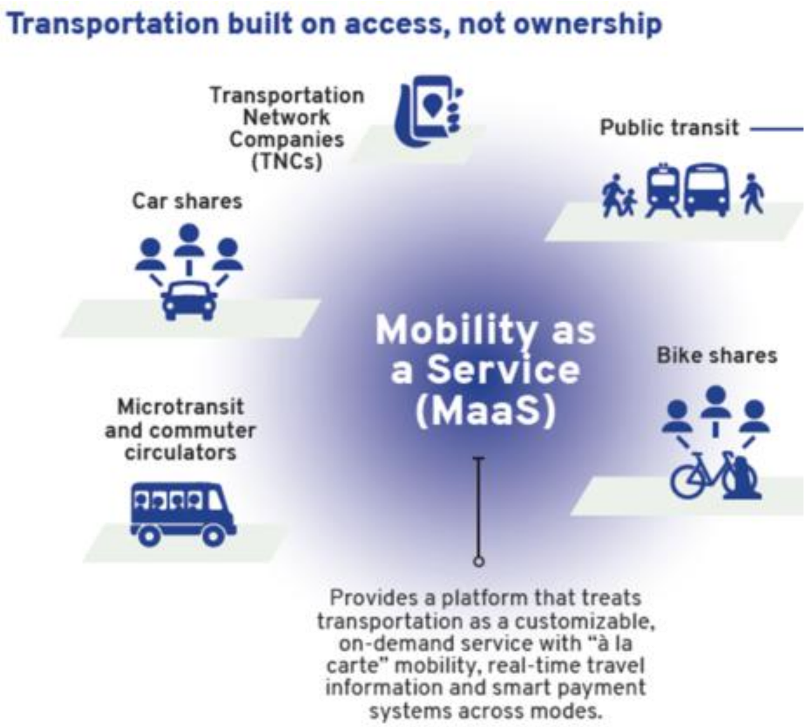


*Figure 1.12 Representation of Maas*

Smart mobility is a user-focused approach that enhances accessibility, reliability, and the overall experience by customising transportation services to meet individual needs. When implemented carefully, it enhances the quality of urban life by making transportation systems more intuitive, responsive, and equitable. Basically, sustainable mobility driven by technology not only characterises smart mobility but also signifies a move toward intelligent, connected, and flexible systems that leverage digital innovations to improve efficiency, safety, and the user experience across transportation networks.

## 1.9 STRUCTURE OF THE THESIS

This thesis addresses sustainable mobility and GNSS-based and IoT-enabled solutions for smart mobility. In particular, it progresses from the theoretical foundations of GNSS and velocity estimation methods, to the metrological verification of GNSS receivers, then to the characterisation of pedestrian velocity using smartphone-based GNSS measurements, and finally to the design and assessment of a wireless sensor network for crowd sensing. It is organised as follows:

***Chapter 2*** provides a theoretical background on Global Navigation Satellite Systems (GNSS). It introduces the main GNSS constellations, signal structures, receiver architecture, and navigation observables. This chapter also emphasises that GNSS is not only used for positioning and navigation but also for estimating the velocity of vehicles, pedestrians, and other users equipped with GNSS receivers. Additionally, the principal GNSS-based velocity estimation methods are presented and compared, establishing the theoretical framework for the application-related analyses in Chapters 3 and 4. In particular, the Doppler-based approach is explored in Chapter 3, and the TDCP approach is examined further in Chapter 4.

***Chapter 3*** describes a method for the metrological verification of GNSS receivers used for velocity measurement. It details the development of a laboratory-grade testbed to assess the accuracy and reliability of GNSS-based speed estimation under controlled, repeatable conditions. Within this framework, Doppler-based velocity estimation is examined as a suitable approach for verifying controlled-speed measurements and Tikhonov regularisation is introduced to stabilise the velocity solution under degraded satellite geometry. This verification methodology aims to support the reliable use of GNSS receivers in sustainable mobility and ITS applications.

***Chapter 4*** focuses on the experimental characterisation of pedestrian velocity using GNSS receivers embedded in smartphones. It investigates the feasibility of using such devices in pedestrian-oriented smart mobility applications, particularly in the context of Intelligent Traffic Light Systems. The chapter presents an experimental evaluation of pedestrian movement through Time-Differenced Carrier Phase velocity estimation under stationary conditions, applied in three diverse urban settings. It also assesses the measurement consistency of the results across two commercially different devices.

***Chapter 5*** presents the wireless sensor network architecture developed for pedestrian crowd sensing. It describes the design of the sensor node based on low-cost IoT technologies, including its cobblestone-shaped enclosure developed for deployment in historically protected urban areas, and explains how pedestrian presence can be estimated using BLE-based sensing and wireless communication. The chapter also reports the experimental characterisation of the crowd sensor and discusses its performance under both controlled and real operational conditions.

Together, these chapters implement, validate, and experimentally demonstrate the three original scientific contributions outlined in Section 1.10, progressing from theoretical foundations to controlled laboratory validation to real-world experimental deployment.

## 1.10 CONTRIBUTION OF THE THESIS

This thesis addresses the need for reliable, low-cost, and scalable sensing methods for smart and sustainable mobility by proposing, implementing and experimentally validating measurement methodologies based on GNSS and low-cost IoT technologies. The work makes three original scientific contributions with respect to the existing literature, each motivated by a specific gap identified in current research.

***Contribution 1 – GNSS Systems and Velocity Estimation Methods for Smart Road Applications***

Research on GNSS-based velocity estimation using Doppler shift and TDCP methods is extensive, and many studies show that GNSS receivers in smartphones can achieve sub-decimeter-per-second accuracy under ideal conditions. However, most studies base their performance assessment on statistical field data collected in favourable sky conditions and use commercial receivers with proprietary firmware, concealing their internal signal processing. Consequently, the internal mechanisms that lead to sudden velocity instability during poor satellite geometry are difficult to observe and are rarely analysed within a unified mechanistic framework, particularly with respect to how the ill-conditioning of the Doppler least-squares matrix can cause abrupt velocity spikes observed in practice.

This thesis presents a metrological verification framework at the laboratory level based on an SDR testbed that processes live-sky raw in-phase and quadrature data entirely through software. It employs a transparent MATLAB-based signal processing chain, making every processing step fully observable, from signal acquisition to the Doppler-based velocity estimation. This allows for an analytical depth not possible with commercial receivers.

The study shows that a stationary receiver can produce unrealistically high velocity estimates when satellite geometry worsens, because the least-squares velocity estimator's design matrix becomes ill-conditioned. To address this, Tikhonov regularisation is applied to the Doppler velocity estimator, successfully limiting the solution to realistic, stationary values. This work provides a reproducible, transparent methodology for improving the reliability of GNSS velocity data, which is crucial for ITS and sustainable mobility.

***Contribution 2 – Experimental Characterisation of Pedestrian Velocity Using GNSS Receivers***

Existing approaches for detecting pedestrians at road junctions primarily rely on fixed infrastructure, such as video cameras, push-button signals, and radar sensors. Although video-based systems offer high spatial resolution, they require costly installation at each intersection, depend on lighting and environmental conditions, and raise significant privacy concerns. Studies on GNSS-based velocity estimation using smartphones have primarily focused on vehicle-centric use cases, such as fleet management and eco-driving. The limited number of studies addressing pedestrian scenarios either rely on simulated trajectories or report only average accuracy without a detailed metrological characterisation of the stationary pedestrian case, which is central to identifying a pedestrian waiting at a road junction.

This thesis provides a systematic experimental characterisation of the TDCP velocity estimator implemented on two contrasting commercial smartphones across three urban scenarios, ranging from open sky to semi-urban and dense urban environments. All measurements were conducted simultaneously under stationary conditions, so that the ground-truth velocity is zero and any non-zero output represents the absolute estimation error. Results show that the estimator produces mean horizontal velocity values consistently close to zero across all tested environments, and that metrological compatibility between the two devices is confirmed at a 68% coverage probability in all three scenarios. These findings demonstrate that the method's performance is governed by the physical environment rather than the specific chipset and provide measurement-based evidence that consumer smartphones can reliably support pedestrian detection in Intelligent Traffic Light Systems as a scalable, infrastructure-free alternative to camera- and radar-based solutions.

***Contribution 3 - A Wireless Sensor Network for Crowd Sensing: Architecture and Experimental Characterisation***

Traditional pedestrian monitoring technologies, including manual counts, fixed video cameras, pressure-sensitive floors, and turnstile counters, require costly or invasive installation and cannot be deployed in historically protected urban areas where excavation and the installation of large roadside hardware are prohibited by conservation regulations. Existing BLE-based pedestrian sensing systems have been designed primarily for indoor environments and focus on instantaneous crowd counting as their primary output metric. To the best of the author’s knowledge, previous work has not jointly addressed a BLE sensor node embedded in a heritage-compatible cobblestone enclosure for outdoor deployment, experimentally validated wireless link quality through the enclosure material under controlled conditions, or demonstrated that monitoring temporal variations in pedestrian activity yields a more robust and operationally meaningful output than precise instantaneous counting for urban mobility planning.

This thesis designs and validates a two-tier, non-invasive BLE-based wireless sensor network in which the sensor node is housed in a ceramic cobblestone enclosure that visually blends with the paved surfaces of traditional historical city centres, without requiring any structural intervention. A controlled semi-anechoic chamber evaluation confirms that the enclosure causes negligible attenuation of the BLE signal and maintains a 100% Packet Reception Rate across all tested orientations and antenna polarisations. A subsequent field deployment demonstrates that the BLE crowd index, derived from the passive scanning of nearby device advertisements, tracks temporal variation in pedestrian activity with strong correlation to the ground-truth observations, without storing any personal identifier. This work reframes BLE-based crowd sensing from an absolute-counting problem to a trend-monitoring approach, offering a more reliable, practically deployable solution for pedestrian safety planning and urban traffic management.

Overall, the novelty of this work lies in integrating transparent GNSS signal processing, smartphone-based pedestrian sensing, and non-invasive IoT crowd monitoring within a unified experimental framework for smart mobility applications.

*CHAPTER 2*

# *GNSS SYSTEMS AND VELOCITY ESTIMATION METHODS FOR SMART ROAD APPLICATIONS*

## 2.1 NAVIGATION SYSTEM

Navigation is the process of determining one's speed, direction, and position while travelling. In ancient times, navigation was carried out using tools such as compasses, maps, and azimuths, primarily through visual observations and terrestrial references. As science and technology advance, satellites, GNSS (Global Navigation Satellite System), and INS (Inertial Navigation Systems) are used to estimate precise locations and speeds [38].

These navigation systems can display digital maps in either text or graphical mode; locate the vehicle by integrating sensor data, stored maps, and data from other sources; and guide the owner with text or voice-based directions. They offer additional functionalities, such as real-time traffic updates, route optimisation, and the recommendation of alternate routes when needed, along with related services [39].

This chapter covers fundamentals of GNSS constellations, signal structures, GNSS receiver design, and signal processing algorithms, which are the basis for innovative mobility applications. The introduction of GNSS observables, error sources, and dilution of precision follows this. Lastly, we outline the key applications of GNSS systems in transportation and smart mobility. Together, this chapter provides the theoretical foundation for GNSS-based velocity estimation (Chapter 3) and for testing the accuracy of GNSS-based speedometers (Chapter 5), along with their testbed design and architectures.

## 2.2 METHODS OF NAVIGATION

Navigation methods can be classified by application domain, underlying principles, and level of technological advancement. Table 2.1 summarises the commonly used navigation methods, their types, and the application.

| *NAVIGATION METHOD* | *APPLICATION* | *PRINCIPLE* | *TYPE OF NAVIGATION* |
|---|---|---|---|
| Land Navigation | Land-based travel | Maps, landmarks, and a compass | Traditional |
| Marine Navigation | Sea and Oceans | Charts, compass, celestial bodies and electronics | Traditional and Modern |
| Piloting (Pilotage) | In Air | Visual References, radio aids and satellites. | Traditional and Modern |
| Celestial Navigation | Sea and Air | Sun, Moon, and stars to find the position | Traditional |
| Dead Reckoning | Land, Sea and Air | Estimates the position using speed, time and direction | Traditional and Modern using INS |

| | | | |
|---|---|---|---|
| Radio Navigation | Air and Sea | Radio-signal-based positioning | Modern |
| Space Navigation | Outer Space | Onboard systems and earth-based tracking | Modern |
| Radar Navigation | Air and Sea | It uses radar to measure the distance and the direction | Modern |
| Satellite Navigation | Land, Sea and Air | Satellite-based positioning | Modern |
| Underwater Navigation | Underwater | INS and acoustic systems | Modern |
| Acoustic Navigation | Underwater | Sonar-based positioning | Modern |

*Table 2.1 Classification of navigation methods based on their application domain, principles and their navigation type*

Table 2.1 lists the different types of navigation methods, which can vary in terms of coverage, accuracy, infrastructure implications, environmental properties, and applicability to various situations and scenarios. Traditional navigation systems, such as celestial navigation and dead reckoning, rely heavily on manual observations (except for dead reckoning using INS), accumulated motion estimates and are therefore limited in accuracy and long-term reliability. Similarly, terrestrial and radio-based navigation systems suffer from restricted coverage, signal blockage or dependence on local infrastructure. Modern navigation techniques aim to overcome these limitations by leveraging external reference signals and advanced signal processing.

On the contrary, the satellite navigation systems provide continuous, global positioning, and timing information independent of local infrastructure. Satellite navigation operates by transmitting signals from multiple satellites with precisely known orbits and timing, thereby enabling the accurate determination of position, velocity, and time (PVT) across terrestrial, maritime, and aerial environments. This technological advancement has established itself as the predominant method for positioning within contemporary transportation and mobility industries.

## 2.3 SATELLITE NAVIGATION SYSTEM

Satellite navigation systems offer a great technological forefront in navigational aids, due to their remarkable accuracy in delivering the precise location, time and speed of the equipped receiver [40]. Small electronic receivers, including those incorporated in smart gadgets of consumer devices, vehicular platforms,  use this technique to compute their position with extreme precision, including latitude and longitude and altitude above sea level, by measuring signal propagation from multiple satellites. In addition to positioning, the radio signals allow the receiver to compute the current local time with high accuracy,  which permits time synchronisation. This combined functionality is commonly referred to as PNT (Position, Navigation, and Time) [41] – [43]

It is also known as Sat Nav. It is the most widely used global navigation technology and is commonly called the Global Navigation Satellite System, which refers to the several independent constellations. Due to the capabilities of PNT services, these systems are widely used in transportation, surveying, and mobility monitoring platforms [42].

### 2.3.1 Classification of Satellite Navigation Systems

From an engineering viewpoint, the term "Satellite Navigation" means more than just GNSS constellations. Because they also include standalone core global constellations, regional constellations, and augmentation systems.


*Figure 2.1 Types of Satellite Navigation Systems*

Core global constellations broadcast range signals and detailed navigation data that enable all users worldwide to compute their PVT. On the other hand, a regional navigation satellite system is designed for coverage in only a limited geographical area. Lastly, the augmentation system is treated as an overlay to improve the performance of the global constellations and provide integrity [44],[45].

### 2.3.2 Error Sources in the Satellite Navigation System

Despite their wide global coverage and high accuracy, their performances can be affected by different types of errors. Such errors include satellite clock bias, errors in orbital parameters, atmospheric delays (ionospheric and tropospheric), multipath propagation, receiver noise, tracking errors, and receiver- or antenna-dependent factors. The effects of these errors are particularly significant in applications that require high precision, consistency, and traceability, such as the calibration and validation of navigation-dependent measuring systems, because the errors can vary with the environment and be correlated across measurements. [41]–[43], [46]–[48].

### 2.3.3 Role in smart mobility

In the development of sustainable and innovative mobility, a navigation system is needed to provide precise position, velocity, and time. Additionally, accurate and reliable navigation solutions are crucial for mobility-related measurement and monitoring systems. This enhances travel efficiency, facilitates easier traffic management with access to real-time traffic data, improves road safety, and reduces fuel consumption and emissions. Therefore, understanding modern navigation technologies, particularly satellite-based navigation systems, is essential for developing, evaluating, and calibrating mobility-related systems, which are the focus of this thesis.

## 2.4 GLOBAL NAVIGATION SATELLITE SYSTEM

A Global Navigation Satellite System is a broad term for a satellite-based system capable of providing continuous PNT services worldwide. In general, it refers to one or more global constellations, including GPS, Galileo, GLONASS, and BeiDou, and their respective Signal-in-Space (SIS) interfaces, which are supported by the ground control segments and ground receivers. [66], [49]. Each constellation consists of multiple satellites in Medium Earth Orbit (MEO), along with a control segment that handles clock and orbit determination and uploads navigation messages, and a user segment embedded in smartphones, vehicles, and surveying equipment. These systems can provide Positioning, Navigation and Timing services for civilian, commercial and military purposes [41]–[43].

### 2.4.1 Working principle of GNSS system

The core working principle of GNSS systems is to estimate the time of flight of the satellite's radio signals from the known satellite locations to the ground receiver. By multiplying the measured signal transmit time by the speed of light, the receiver obtains pseudo-range measurements. The receiver uses this information and the trilateration method to determine its three-dimensional location and a time reference. It is considered that, with measurements from at least 4 satellites, the receiver can calculate its 3D position and compensate for any clock bias. This process relies on geometric estimation based on online-of-sight signals and satellite-receiver geometry, with performance strongly influenced by measurement noise and other factors such as the space environment, signal propagation, and receiver segments [41]-[43]

### 2.4.2 Evolution of GNSS systems

The history of GNSS systems shows an evolution over several decades from ancient to modern navigation technologies, involving numerous advancements. This development has not followed a single straight path but has grown in various, customised environmental contexts [50], [51]. Modern GNSS began developing with the rise of satellite technology in the 20th century, enabling more accurate PNT services. It is because the industry and society demand safer, more precise, and more efficient positioning [52].

The growth of these systems has not only been driven by their signal design, atomic frequency standards, orbit and clock termination, and receiver processing, but also by application-driven demands for safety, availability, and integrity, especially in aviation, maritime navigation and other related fields [42]–[45]. Similarly, mass-market applications in road transport, logistics, and other location-based services have encouraged the development of low-cost receiver designs that contain multifrequency and multiconstellation solutions.

### 2.4.3 Multi-Constellation Development

At the beginning, satellite navigation systems were designed to function independently, providing the positioning services only to a specific country or region. But due to the advancements in technology and the increasing demand for reliable global positioning, this has led to the development and widespread adoption of multi-constellation GNSS systems [41]-[45]. For mobility-related applications, it is essential to understand the core principles and limitations of these systems. So, the following section discusses the signal properties, sources of navigation errors, and the receiver architecture.

### 2.4.4 Types of GNSS systems

GNSS systems are classified into three categories: Core Global constellations, regional constellations and satellite-based augmentation systems. Each of these constellations has its own orbital placements, signal formats, and service types. Figure 2 illustrates the categories of GNSS systems.

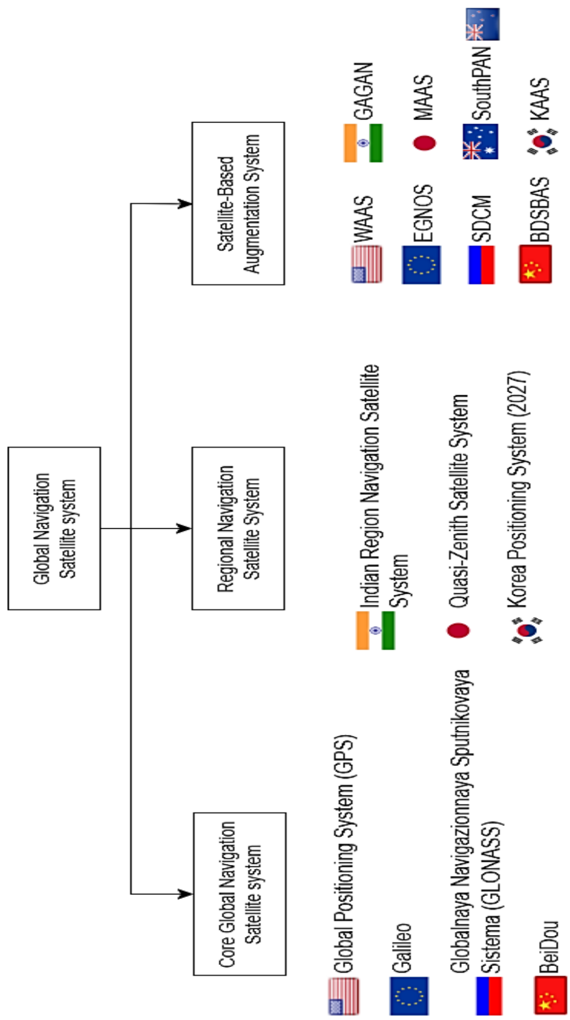


*Figure 2.2 Classification of GNSS system*

#### 2.4.4.1 Core Global constellations

Global constellations are groups of satellites placed in Medium Earth Orbit that continuously broadcast ranging signals and navigation messages, thereby enabling PVT computation services for receivers worldwide. Official Interface documents clearly define the technical specifications of these signals, their structures, modulation methods and also the structure of the navigation method [42], [43].


*Figure 2.3 Core global constellations*

#### 2.4.4.2 Regional Satellite constellations

Regional systems are developed to deliver PNT services within a specific geographical region, especially in their own countries and within a few hundred kilometres of their surrounding areas. These satellites are placed in geostationary orbit because this helps the system achieve better coverage within its coverage area, as it typically uses GEO or Inclined Geosynchronous Orbit (IGSO) satellites. This improves the satellite's visibility to the receiver, attains a favourable elevation angle, and improves the signal geometry [42], [43].

#### 2.4.4.3 Augmentation Systems

These systems are there to enhance the performance of the core global systems, rather than providing an independent navigation performance to the receiver. They are generally classified into three types, and they follow the International Civil Aviation Organisation (ICAO) standards for performance-based navigation systems [53], [54].

The kinds of Augmentation systems are given below:

a) Satellite-Based Augmentation Systems (SBAS)

b) Ground-Based Augmentation Systems (GBAS)

c) Aircraft-Based Augmentation Systems (ABAS)

A simplified comparison of these systems is given in Table 2.2

| Features / Constellations | Standalone PVT solution | Revolutionary Orbit | Navigation message | Integrity service | Coverage area |
|---|---|---|---|---|---|
| Core Global Constellations | Globally | Medium-Earth Orbit | Yes | No | Worldwide |
| Regional Constellations | Regional | Geo-Stationary Orbit/ IGSO | Yes | No | Regional |
| SBAS | No | GEO broadcast | No, but it provides the correction parameters | Yes | Wide-Areas |
| GBAS | No | Ground-based systems | No | Yes | Airport areas |
| ABAS | No | N/A | No | Yes | User-dependent |

*Table 2.2 Comparison of Global, Regional, and Augmentation GNSS Systems by Functional Capabilities*

As we know, when the signal travels through space to reach the receiver, it is more prone to errors introduced by the receiver's performance. This is where the augmentation system plays a significant role, providing atmospheric correction parameters and integrity information to any GNSS receiver. This improves the receiver's performance, particularly in safety-of-life applications such as aviation and maritime navigation, where high reliability and trust in positioning information are critical [53].

The primary objective of the Signal augmentation systems is to improve

a) Integrity – Providing timely warning when the system should not use the signals for navigation.

b) Availability- ensures the reliable positioning services across a wide range of geographical areas.

c) Accuracy – collects the satellite orbit, clock and atmospheric errors.

d) Continuity – maintains the consistent services without having unexpected interruptions.

#### 2.4.4.4 Satellite-Based Augmentation System (SBAS)

An SBAS is a complete differential GNSS augmentation system that uses several geostationary satellites to cover large areas and distribute essential GNSS data, such as ranging, integrity, and correction information, provided by a network of ground stations. The SBAS architecture consists of three elements: a Master Control Station, a Uplink Station, and a GEO satellite that transmits the correction messages. The reference systems within the service area collect GNSS signals and forward them to the master station. The master station knows its exact positions to perform the wide-area adjustments. These correction messages are sent to SBAS satellites, which broadcast them across their coverage areas to improve signal reliability. The GNSS receiver then applies these corrections to its range calculations, resulting in more accurate positioning and enhanced overall performance [57], [58].

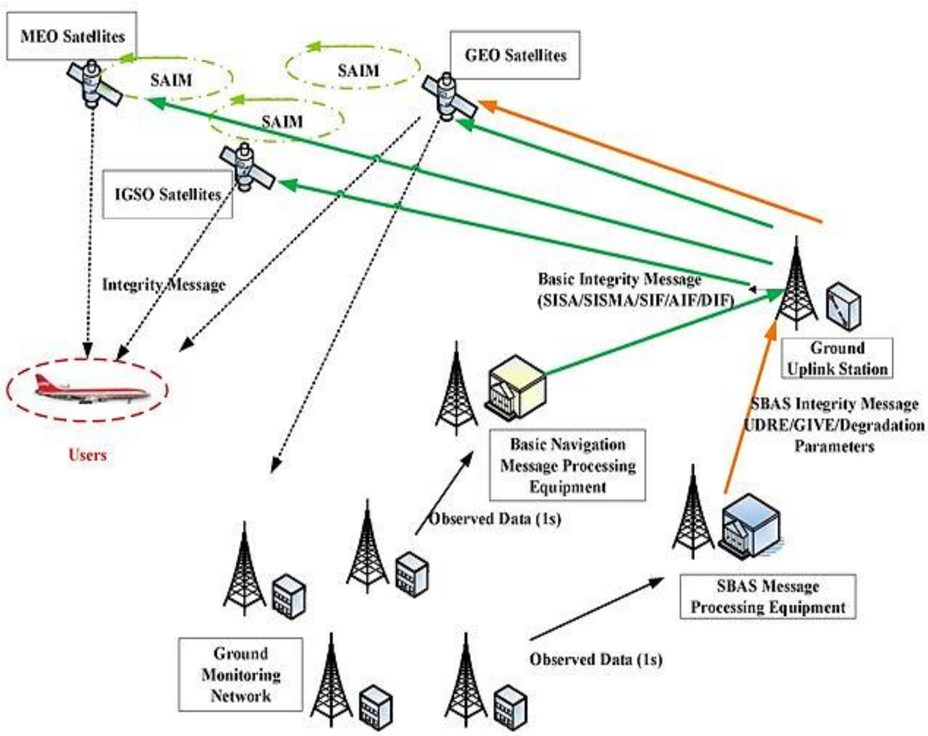


*Figure 2.4 Architecture of SBAS [58]*

Some of the SBAS services that are implemented around the world are given below:

- Wide Area Augmentation System *(WAAS)* - operated by the U.S. Federal Aviation Administration
- European Geostationary Navigation Overlay Service (EGNOS) - owned by the European Space Agency

- BeiDou Satellite-Based Augmentation Systems *(BDSBAS)* - owned by the People's Republic of China to provide support on BeiDou.
- Multi-functional Satellite Based Augmentation Systems *(MSAS)* – operated by Japan's Ministry of Land, Japan Civil Aviation Bureau.
- GPS-Aided GEO Augmented Navigation Systems *(GAGAN)* – operated by the Airports Authority of India.
- System for Differential Corrections and Monitoring *(SDCM)* – developed by the Russian Federation.
- Southern Positioning Augmentation System *(SouthPAN)* – developed to provide SBAS to Australia and New Zealand.
- The Korea Aerospace Research Institute developed the Korean Augmentation Satellite System (KAAS)
- African Satellite Augmentation Systems *(ASAS)* – a SBAS system developed by a group of international public organisations (17 African nations and France)
- South America, Central America and the Caribbean Augmentation System *(SACCSA)*.

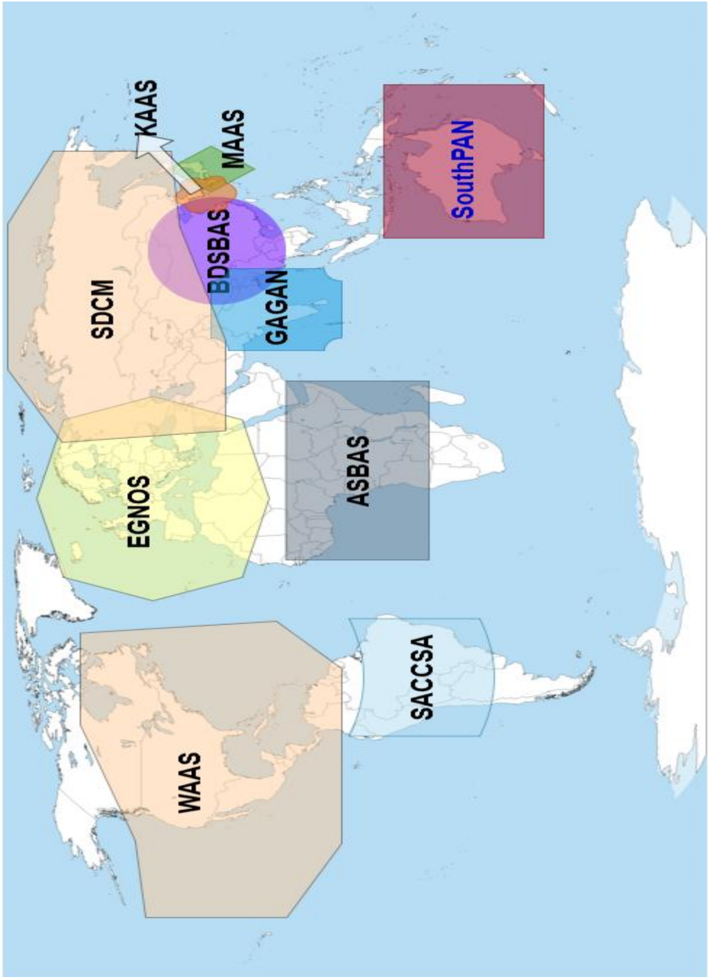


*Figure 2.5 SBAS constellations around the world*

### 2.4.4.5 Ground-Based Augmentation System (GBAS)

A GBAS works in combination with GPS to enhance aircraft safety during approaches and landings by transmitting updated location, route, and integrity information via VHF data. The aircraft's position, along with its lateral and vertical deviations from the intended path, is determined by processing uplinked data through two multimodal receivers installed on the plane [59], [60].

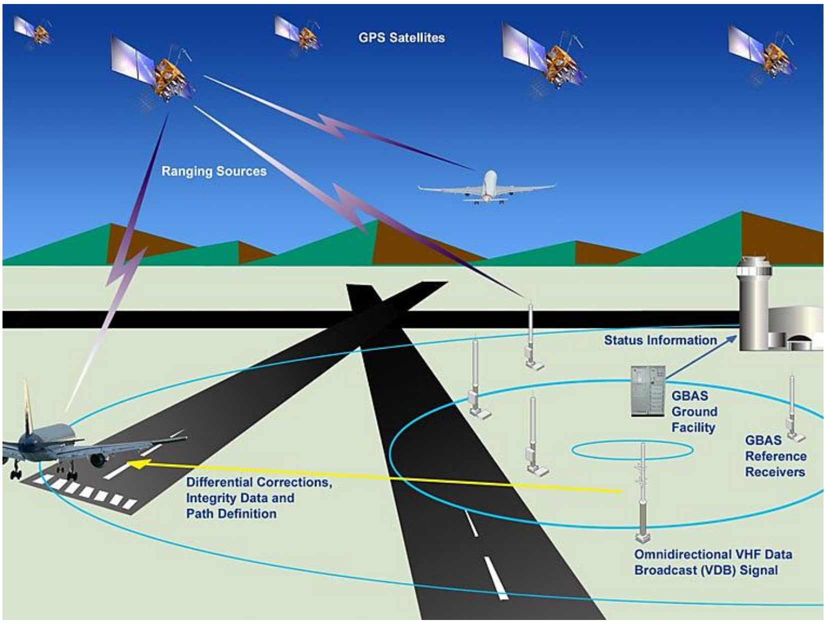


*Figure 2.6 Architecture of GBAS [59]*

The GBAS system comprises three elements: the GBAS ground subsystem, the GBAS Aircraft subsystem, and the GNSS satellites subsystem.

**a) GBAS Ground Subsystem**

It generally consists of at least three GNSS reference receivers with antennas installed at accurately surveyed locations, a central processing unit, and a VHF data broadcast transmitter located at the airport, which operates within the 108-117.975 MHz frequency range [60], [61]. This system handles various tasks, such as receiving and decoding the SIS, performing integrity monitoring, calculating differential corrections for carrier-smoothed codes, and generating and broadcasting GBAS messages [59].

**b) GBAS Aircraft Subsystem**

The GBAS aircraft subsystem includes a GNSS receiver, a GNSS antenna, a VHF antenna, and the processing units. It processes GBAS ground subsystem, GNSS SIS and VDB messages, which apply differential corrections and calculate enhanced position solutions [59], [62]. Using the Final Approach, Existing systems can execute GBAS approaches by segmenting data, establishing the flight path, identifying deviations, and transmitting guidance signals such as Instrument Landing Systems (ILS). [59]-[62]

**c) GNSS satellites subsystem**

The GNSS satellite subsystem primarily comprises core satellite constellations that provide ranging signals for GBAS, such as GPS. These satellites transmit L-band navigation signals containing location data, including accurate time and orbital parameters, enabling ground- and airborne receivers to compute raw pseudo-range measurements [59], [61].

#### 2.4.4.6 Aircraft-Based Augmentation System

ABAS can give GNSS information as needed for additional navigation purposes. It is a system that supplements and/or integrates the information they have collected from the other GNSS elements with the data accessible on the board [63]. There are two forms of Aircraft-based augmentation systems, ***Receiver Autonomous Integrity Monitoring (RAIM)*** *and* ***Aircraft Autonomous Integrity Monitoring (AAIM)*** [64].

***RAIM*** is the most widely used aircraft-based system. It is an algorithm inside the GNSS receiver. It uses redundant pseudo-range measurements from an additional satellite when more than four satellites are in view. This way, it can perform fault detection (FD) and fault detection and exclusion (FDE) if there are six satellites in the receiver's view [65].

In ***Aircraft Autonomous Integrity Monitoring***, the signal is integrated with other navigation sensors, such as the inertial navigation system (INS), which can provide an integrity check for GNSS when RAIM is unavailable. Today, about 70% of European flights are operated by aircraft equipped with GPS and RAIM [63], [65].

## 2.5 ARCHITECTURE OF GNSS SYSTEMS

GNSS systems typically have a three-segment architecture: the space segment, the control segment, and the user segment. This three-segment structure is common to all global constellations.

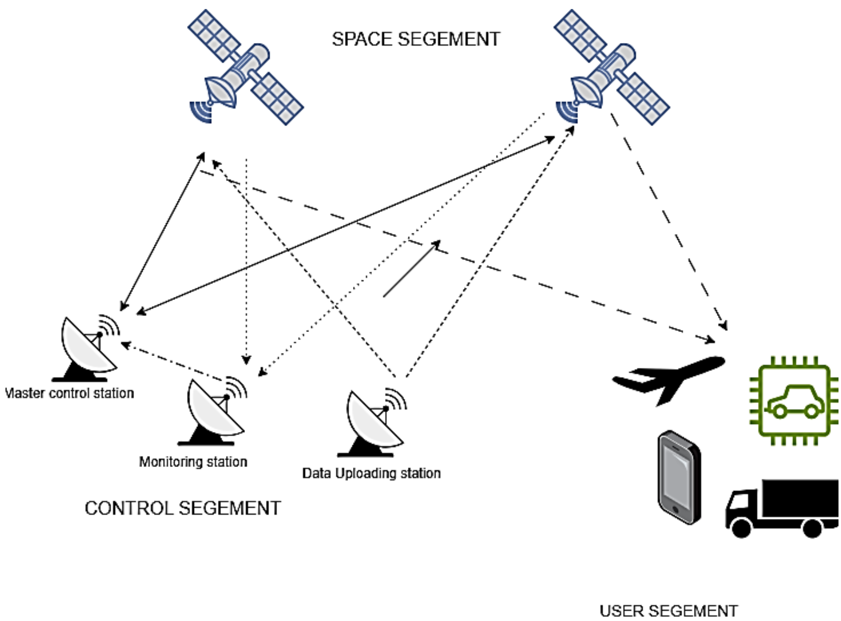


*Figure 2.7 GNSS Segments*

### 2.5.1 Space Segment

GNSS's space segment comprises the satellites that transmit signals receivers use to estimate PNT solutions. They are formed by a group of different constellations, and in order to ensure that a sufficient number of satellites are visible from every location on the Earth's surface. The availability and geometry of these satellites are essential to GNSS performance, as the receiver needs to observe multiple satellites simultaneously to determine its position accurately. The primary function of the space segment is to provide the ranging signals and the navigation data to the user segment. Every satellite continuously transmits radio-frequency signals that include a navigation message and exact time information. These signals enable the receiver to determine the relevant pseudorange by measuring the time of propagation from the satellite to the receiver.

The important factors, including satellite ephemeris, satellite clock corrections, almanack data, and health information, are included in the navigation message broadcast by the satellites. The ephemeris data enables the receiver to determine the satellite's precise location at the time of signal transmission, while the clock correction parameters compensate for deviations in the onboard time reference. On the other hand, almanack data facilitate signal acquisition and satellite selection, and provide coarse orbital information for the entire constellation. A key feature of the space segment is the use of highly stable atomic clocks onboard the satellites. Since timing accuracy is essential for GNSS positioning, satellites are equipped with atomic frequency standards, such as rubidium or caesium clocks, and, in some modern blocks, passive hydrogen masers.

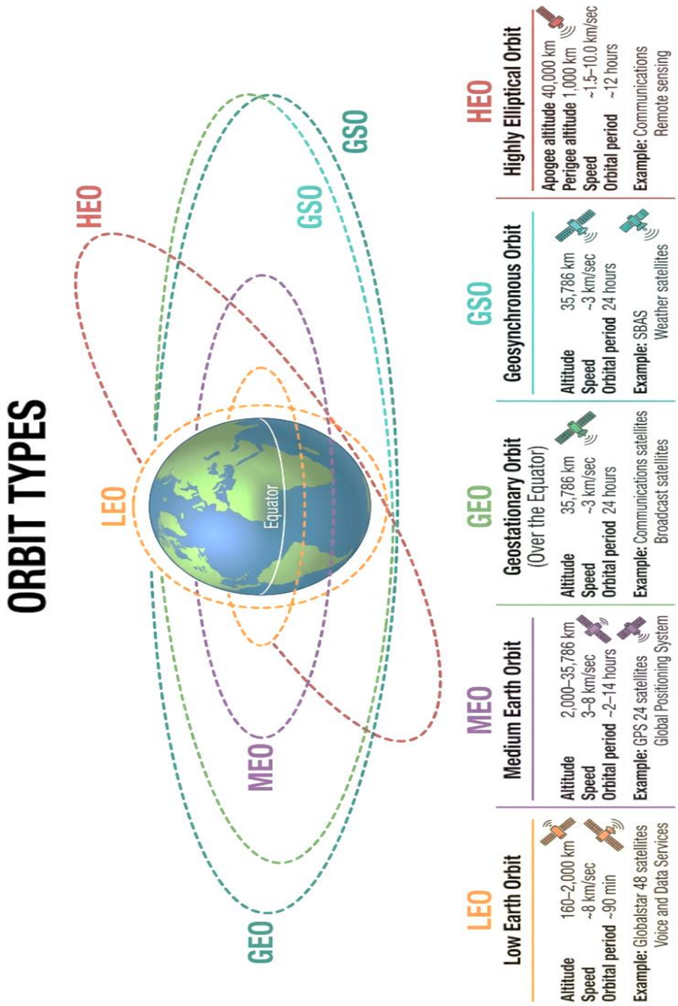


*Figure 2.8 Types of Orbits*

Most GNSS satellites are placed in Medium-Earth Orbit (MEO), typically at an altitude of 20,000 km, which provides a suitable balance between global coverage and operational efficiency. Because the satellites at these altitudes cover a large portion of the Earth's surface, it is possible to achieve worldwide service with a limited but sufficiently redundant number of satellites. To maximise visibility and geometric variation for users at various latitudes, the satellites are distributed across multiple orbital planes with distinct inclinations. To increase regional coverage and continuity, some systems, such as BeiDou, are also placed in Inclined Geosynchronous Orbits (IGSO) and Geostationary Orbit (GEO).

### 2.5.2 Control Segment

The control segment is a distributed ground network that consists of a Monitoring station, Master Control stations (MCSs), and Uplink stations. This is also called the ground segment.

a) *Master Control Stations*

MCSs adjust the orbital parameters of the satellites and onboard clocks to maintain their accuracy. They process the observations, estimate the satellite ephemerids, and clock offsets. MCSs also contribute to the generation of updated navigation messages.

b) *Monitoring Stations*

Monitoring stations, also known as reference stations, continuously observe all visible satellites and measure their range and clock behaviour. They are usually located across a broad geographical area. They monitor and send that information to the MCS, and the master control station analyses the signals and sends orbit and time corrections to the satellites via the uplink stations.

c) *Uplink Stations*

These are installed with the antennas and transmit updates to the satellites, their health/status flags, and control satellite manoeuvres [57], [66].

### 2.5.3 User Segment

The user segment is the last layer of the GNSS PNT services. It analyses satellite signals to obtain position and time information. The type of user means of communication varies from smartphones and handheld devices [57]. After receiving GNSS signals, they determine GNSS observables, such as pseudo ranges, Doppler measurements, carrier phases, and others, to solve the navigation equations [66].

## 2.6 FUNDAMENTALS OF GNSS SIGNALS

GNSS satellites consistently broadcast RF signals on two or more L-band frequencies, typically between 1.1 and 1.6 GHz. These signals utilise a direct-sequence spread-spectrum (DSSS) waveform. The signals are produced by multiplying the low-data-rate navigation information with a high-rate Pseudo-Random Noise (PRN) spreading code, which is subsequently modulated onto the radio frequency (RF) carrier via the DSSS technique [67].

The most common type of access scheme is direct-sequence Code Division Multiple Access (CDMA), because many satellites share the same frequency band. The primary elements of the GNSS signals are:

a) *Carrier Signal:* This is the signal that propagates through the space, and it carries the modulation from the code and the data to the receiver.

b) *Ranging Code / Spreading Code (PRN):* It is a sequence of zeros and ones. The receiver then duplicates the PRN code and adjusts the signal until it aligns with the received satellite code.

c) *Navigation Data:* This is a low-rate binary data that is modulated onto the carrier, with the information on satellite ephemerids, clock bias, satellite health status, and other helpful information [67], [42].

## 2.7 GLOBAL POSITIONING SATELLITE SYSTEM

### 2.7.1 GPS Signal Characteristics

The Global Positioning System (GPS) is the most popular GNSS system, transmitting signals in the L-band, primarily at L1 (1575.42 MHz) and L2 (1227.65 MHz), with the modernised L5 signal centred around 1176.45 MHz also used. Satellites from the space segment provide continuous coverage of Earth using these two RF signals. But lately, a signal band has appeared in L5 [68].

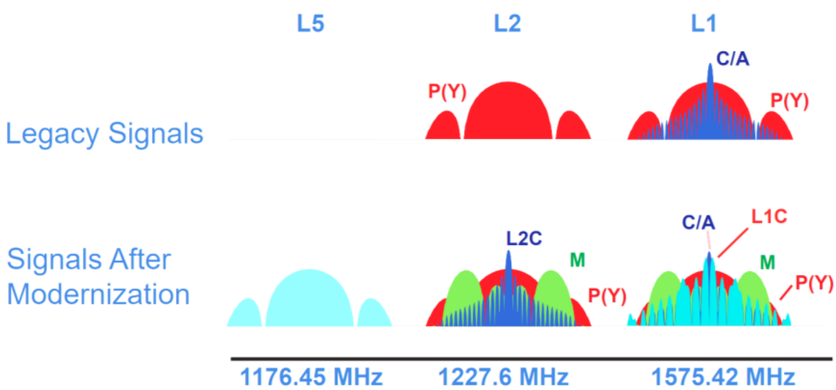


*Figure 2.9 GPS Legacy and modernised signals [69]*

Each GPS satellite has a unique set of PRN codes, also called spreading or ranging codes. While these codes operate on the same carrier frequencies as other GNSS systems, they are distinguishable for each receiver because they are mutually orthogonal, enabling precise correlation. The signals jointly provide civil and military services at different performance levels and with varying degrees of correlation [42], [67], [68].

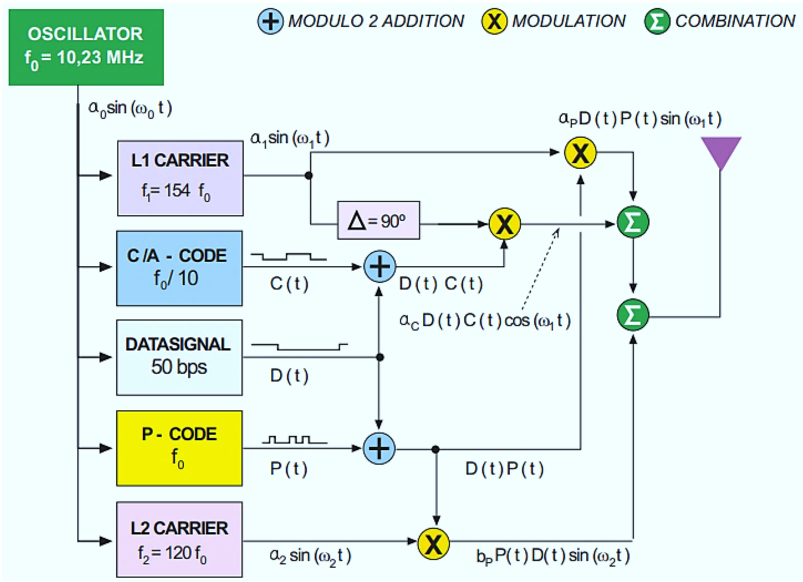


*Figure 2.10 Structure of the GPS Legacy signal*

A generic GPS signal is represented as:

$$s(t) = AD(t)\, C(t) \cos\, (2\pi f_c t + \emptyset) \qquad (2.1)$$

where,

$A$ = Amplitude of the GPS signal

$f_c$ = Carrier Frequency

$C(t)$ = PRN code sequence

$D(t)$ = Navigation Data

$\emptyset$ = Carrier Phase

### 2.7.2 GPS Carrier Signal

L1 and L2 are also known as Legacy Signals. These signals are produced by the highly stable satellite's atomic clock, which operates at 10.23 MHz and is right-hand circularly polarised (RHCP), improving the signal's propagation through the atmosphere and helping reduce losses caused by antenna orientation mismatch. This fundamental frequency is multiplied by two integers, 154 and 120, to generate the frequencies of the L1 and L2 carrier signals [67]. The L-band is chosen because it has lower atmospheric attenuation compared to higher frequencies. When the signal reaches the Earth's surface, its power is usually about -160 dBW, so a sensitive receiver is necessary [42].

The carrier waveform contains no information unless it's modified. The GPS uses different modulation techniques to combine the spreading codes and navigation data, allowing simultaneous signal transmission while maintaining spectral efficiency and correlation performance.

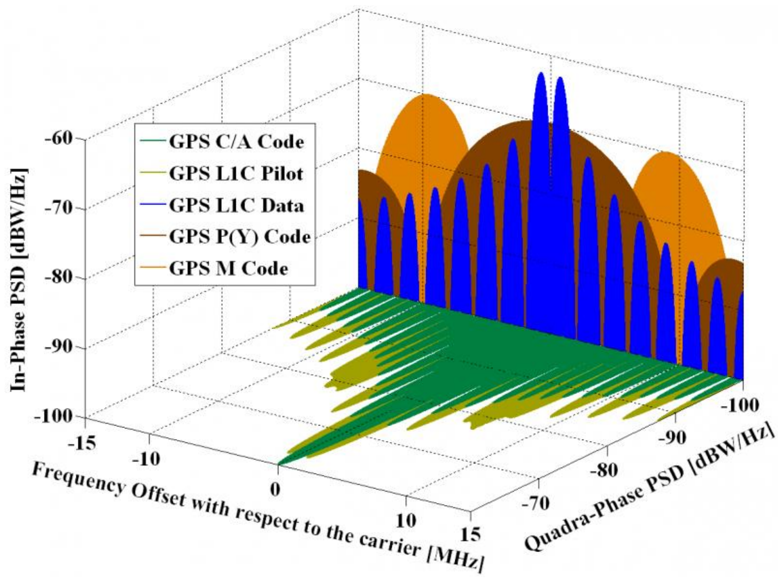


*Figure 2.11 Power Spectral Density of the GPS L1 frequency band*

### 2.7.3 Ranging codes

Ranging codes in GPS are binary pseudorandom noise (PRN) sequences assigned to each satellite and used in CDMA and time-of-flight ranging. Three different PRN codes are transmitted with the carrier signal.

**a) Precision code**

P-code is the original military code that is used for military positioning service or Precise Positioning Service (PPS). This ranging code can be modulated on both the L1 and L2 carrier signals. This code has a chipping rate of 10.23 MHz (the same as the atomic clock frequency), and the P-code wavelength is 29.3 m [70]. This is a 7-day sequence and consists of two subsequences, X1 and X2i, with lengths of 15,345,000 and 15,345,037 chips, respectively. The X2i sequence is deliberately delayed by 1 to 37 chips of X2 [68].

X1 itself is produced by the modulo-2 sum of the outputs of the two 12-stage registers (X1A and X1B), which are short-cycled to 4092 and 4093, respectively. The polynomials for X1A and X1B, used as inputs to the shift register, are provided below:

$$X1A = 1 + X^6 + X^8 + X^{11} + X^{12}$$

$$X1B = 1 + X^1 + X^2 + X^5 + X^8 + X^9 + X^{10} + X^{11} + X^{12}$$

Similarly, for X2i sequences, it first generates X2 and then delays it by a chosen number of chips (1-37). Each of the X2i sequences is then XORed with the X1 sequence, resulting in up to 37 unique P(t) sequences. The polynomials for X2A and X2B that need to be fed into the input of the shift registers are:

$$X2A = 1 + X^1 + X^3 + X^4 + X^5 + X^7 + X^8 + X^9 + X^{10} + X^{11} + X^{12}$$

$$X2B = 1 + X^2 + X^3 + X^4 + X^8 + X^9 + X^{12}$$

### b) Y-code (encrypted P-code)

This is similar to P-code, but it is used only when the anti-spoofing (A/S) mode is activated. It is formed by combining P-code with a classified W-code. Then this is modulated onto the carrier signal in place of the P-code on both L1 and L2. So, only receivers with the keys can generate the code replica and cease the Precise Positioning Service [68], [71].

### c) Coarse/Acquisition code

All GPS satellites broadcast the C/A code on the L1 frequency to offer the Standard Positioning Service (SPS). This civilian-ranging code doesn't need a decryption key like the P(Y) code. It utilises a 1023-chip gold code with a chipping rate of 1.023 MHz. Each satellite broadcasts a signal modulated with a unique C/A code, generated by the modulo-2 sum of two 1023-bit linear patterns G1 and G2i. The formation of G2i is similar to that of X2i, where G2i is delayed by an integer number of chips [68], [71]. There are 10-stage shift registers, and the register inputs are described below :

$$G1 = X^{10} + X^3 + 1 \qquad G2 = X^{10} + X^9 + X^8 + X^6 + X^3 + X^2 + 1$$

### 2.7.4 Navigation Data

Navigation data is an essential component of the GPS signal, as it carries all the information needed to convert raw code measurements into a readable position, including latitude, longitude, and time. There are several types of navigation messages transmitted by the satellites, such as civil L2-CNAV, CNAV-2, L5-CNAV, and MNAV, but Legacy NAV is one of the main ones that GPS relies on. The only difference is that, in the modernised navigation message, the same data as the LNAV is transmitted at a higher rate [68], [72].

#### 2.7.4.1 Structure of LNAV message

In the Legacy GPS Navigation message, the data stream is transmitted at 50 bit/s, that is, modulo-2 added to the PRN ranging code C/A on the L1 channel and to P(Y) on both the L1 and L2 channels. The message is in a basic format of 1500 1500-bit-long frames, divided into 5 subframes, each carrying 300 bits. Each subframe takes 6 seconds, so the total time to transmit one frame of the navigation message is 30 seconds [68], [72].

Each subframe consists of 10 words, each with 30 bits. Each subframe starts with a Telemetry (TLM) word and a Hand-Over-Word (HOW) for synchronisation and time-of-week information, and the MSB words are transmitted first. Subframes 4 and 5 are sub-commutated 25 times each; therefore, a complete data message necessitates the transmission of 25 full frames, for a total of 37500 bits. It will take 12.5 minutes to send the whole navigation message [68].

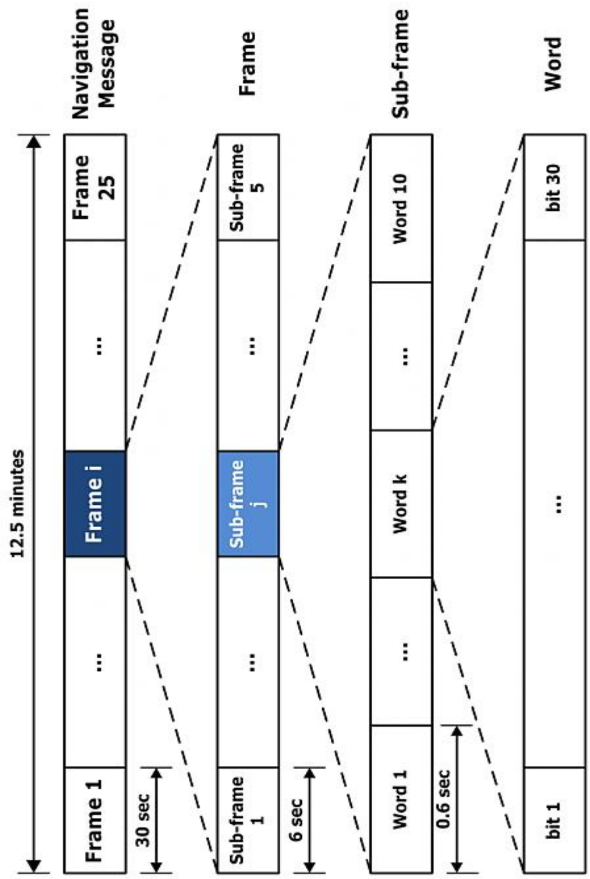


*Figure 2.12 Structure of the GPS L1 C/A navigation message*

Subframe 1 contains the satellite's clock correction parameters, such as af0, af1, and af2, along with other time-related parameters, GPS week number, and the satellite's health/status flags.

Subframes 2 and 3 hold the ephemeris, including Keplerian orbital elements and perturbation terms, such as semi-major axis, eccentricity, inclination, right ascension, argument of perigee, mean anomaly, and correction coefficients. It is possible to calculate the satellite's velocity using these parameters with the formula specified in the official GPS Interface documents.

Lastly, subframes 4 and 5 include almanack data, ionospheric correction parameters, and constellation status, which help the receiver determine the signal source. A total of 25 frames is required to read the entire almanack data [68], [72].

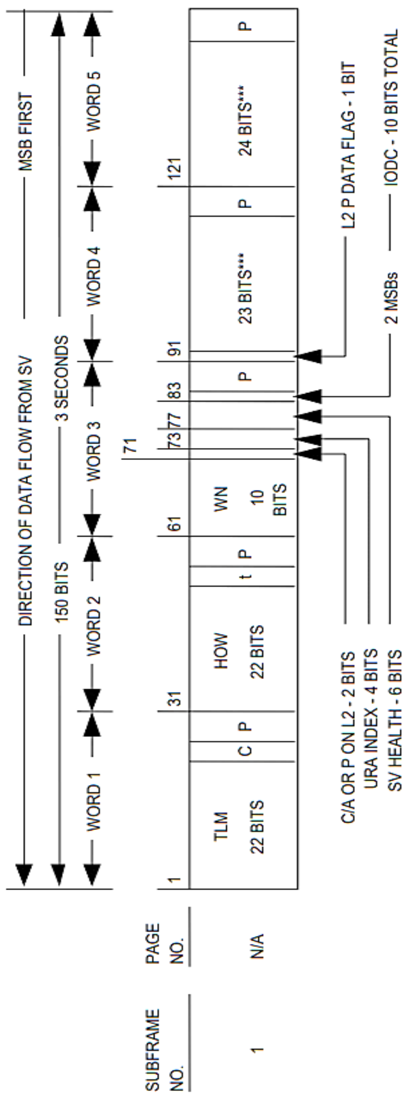


*Figure 2.13 Layout of subframe 1*

### 2.7.5 Modulation

In a GPS signal, modulation refers to how the ranging codes and navigation data are applied to an L-band carrier to create a spread-spectrum signal for transmission. Legacy GPS signals use binary phase-shift keying (BPSK) with DSSS. The PRN and the NAV data result in a 180° phase shift of the carrier signal. Modernised civil signals, such as L5 and L1C, use data/pilot channels and binary offset carrier (BOC) modulation to enhance tracking performance and improve spectrum compatibility with other signals [73].

### 2.7.6 Quality Metrics

A primary quality metric for GPS and other signals is the carrier-to-noise density ratio (C/N0). It is defined as the ratio of the received carrier power to the noise power spectral density and is usually expressed in dB-Hz. Higher C/N0 indicates a stronger, clearer signal, allowing for more precise tracking loops and shorter coherent integration times. Conversely, low C/N0 values indicate attenuation, interference, and multipath effects, which increase measurement noise [74].

These values typically range from 40-50 dB-Hz in clear sky conditions and 20–30 dB-Hz in degraded urban or indoor environments [42]. It is estimated at the tracking stage from the correlator output during signal processing and determines the accuracy of pseudo-range, Doppler, and carrier-phase measurements.

Another significant factor in estimating the quality of the GPS signal is the Signal-to-Noise Ratio (SNR). It is related to C/N0 because it measures the ratio of signal power to noise power. A higher SNR indicates a cleaner and stronger signal.

## 2.8 GNSS RECEIVER ARCHITECTURE

GNSS receivers can process a weak satellite signal as low as -130 dBm to determine the user's position, velocity, and time. Regardless of their variety of commercial and research applications, almost all the GNSS receivers have the same architectural design. It can be described as a cascade of four primary functional blocks: *a) Antenna; b) RF front end; c) baseband signal processor, and the navigation processor* [41], [42]. In modern receiver designs, these functions can be implemented in dedicated hardware, software, or a hybrid mode that divides the processing between programmable logic and a general-purpose processor. The user receiver tracks the presence of radio signals that have travelled through the space, and it tries to synchronise with them [75].

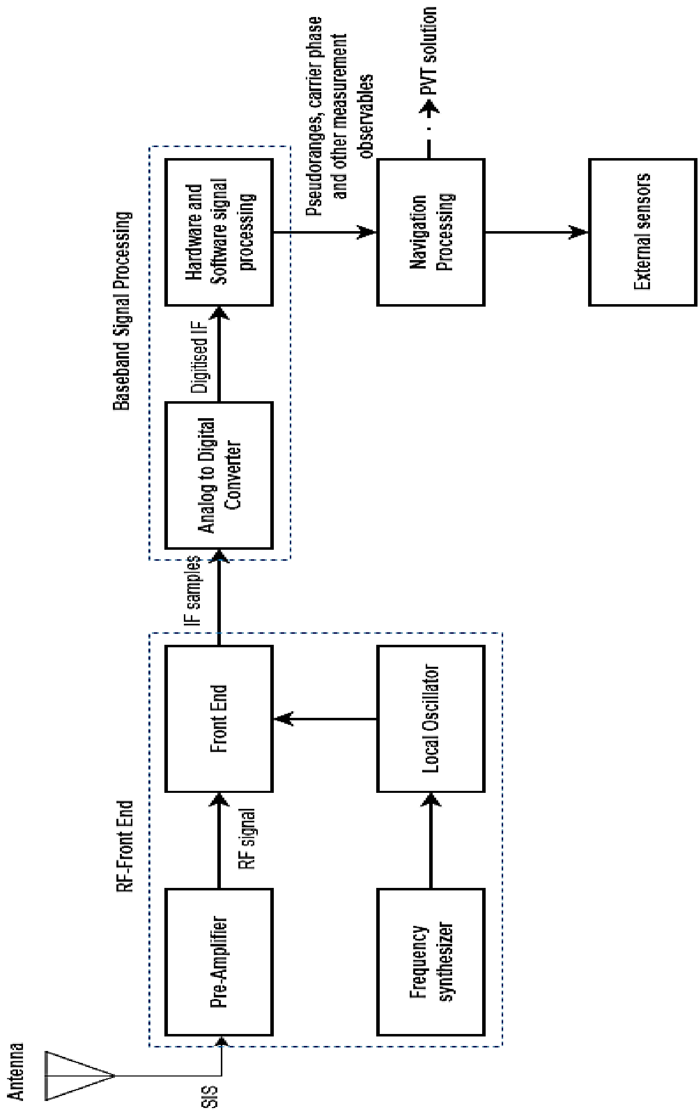


*Figure 2.14 GNSS Receiver Architecture*

### 2.8.1 Antenna

The antenna is the primary source for the GNSS receiver, as it establishes contact between the user receiver and the satellite signal travelling through space. They are designed to receive RHCP signals, which are widely adopted across satellite constellations [41]. Multi-frequency and multi-commutation receivers usually rely on wide-band or multi-band antenna designs to ensure adequate gain in the band of interest.

For applications such as smartphone navigation, patch antennas are used due to their low cost. In contrast, for applications that demand high precision, Choke ring antennas are used, which are necessary for millimetre-level location [42]. These choke-ring antennas can nullify low-elevation signals because their gain is effectively reduced.

### 2.8.2 Radio-Frequency front end

The satellite signal received by the Antenna is fed to the RF front end, which processes it. This is a chain of Low-Noise Amplification, filtering, one or more mixer stages powered by the oscillator, down-conversion, and conversion of an analogue signal [75].

After the antenna, the preamplifier determines the receiver system's overall noise figure, usually providing a gain of about 25-40 dB. It amplifies the incoming signal while adding the least possible noise, typically with a noise figure below 2 dB. When combined with filtering and burnout protection, the total noise figure can be increased to 3-4 dB [76].

The front end subsequently receives the amplified signal and performs down-conversion, either directly from RF to baseband or through heterodyning. This process involves combining the locally generated signal with the incoming RF signal. The rationale for this approach is that high-frequency spread-spectrum signals cannot be digitised efficiently, leading to the shifting of identical information to two distinct frequencies: the sum and the difference of the mixed frequencies [77].

### 2.8.3 Baseband signal processing

In baseband signal processing, two stages are performed to extract the pseudorange, carrier phase, code phase, and Doppler. First is the analogue-to-digital conversion, followed by the signal processing, where acquisition and tracking take place. The downconverted IF signal is fed to the ADC block to provide the digitised IF samples. Sampling and quantisation processes take place to continue with this. During this stage, the sampling frequency fs must be carefully chosen and satisfy the Nyquist sampling theorem [77].

In the signal processing phase, the baseband first performs ***acquisition,*** in which the correlation of the digitised IF samples with the locally generated PRN replica is computed over a grid of code delays and Doppler frequencies to detect the signal in view and obtain the coarse delay and Doppler variables [78].

***Tracking*** takes over the acquired signal, runs continuously, and locks the locally generated code and carrier to the incoming signal, using the Early, Prompt, and Delay correlator outputs. Delay Locked Loop (DLL) is used for code tracking, and Phase Locked Loop (PLL) or Frequency Locked Loop (FLL) is used for carrier tracking [79].

### 2.8.4 Navigation processor

The last step for the receiver is to analyse the pseudorange, carrier, and code measurements from all acquired satellites to calculate the user's Position, Velocity, and Time, and the navigation filters perform this process. The principle of position estimation is called "trilateration" because the satellite's positions are known, which are derived from the navigation message broadcast by each satellite.

The basic principle behind this PVT computation is that the processor first calculates the Earth-centred coordinates of each satellite and their signal transmission times, then applies the clock corrections. It results in a set of observation equations that relate the unknown receiver's position and receiver clock bias. It then uses either the least-squares or Kalman filtering method to estimate the PVT. The navigation processor uses Doppler measurements or time-differenced carrier phase to calculate the receiver's velocity with greater precision than simple position differencing.

## 2.9 GNSS VELOCITY ESTIMATION METHODS

In GNSS navigation, velocity is not an independent measurable quantity, unlike pseudo-range or carrier-phase observables. It is derived from observations of the rate of change of the receiver-satellite range or from measurements of the displacement of the receiver position from point A to point B at two measurement epochs, called the instantaneous velocity (refer to Figure 2.15) [80]. This means that the accuracy of the velocity estimation is linked to the accuracy and continuity of the raw measurements in the receiver. Any disruption, such as cycle slips, can cause the velocity estimation to incur a gross error. Many existing methods for velocity estimation have been studied to determine the best approach for GNSS receiver velocity estimation embedded in smartphones, and TDCP seems quite promising [81]-[90].

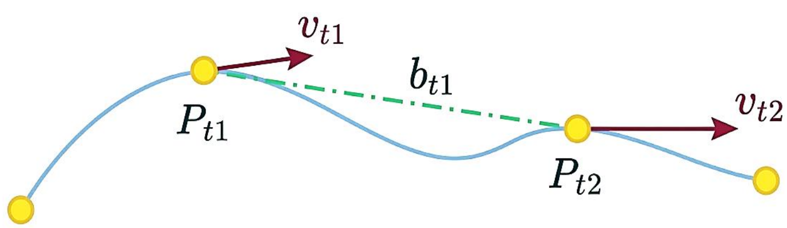


*Figure 2.15 Instantaneous velocity using position change*

Some of the methods are described as follows. The following outlines three principal GNSS velocity methods: Doppler-based velocity estimation, pseudorange differencing, and Time-Difference Carrier Phase (TDCP), along with related techniques such as Carrier-Phase RTK and Kalman filtering.

**a) Velocity estimation using the direct Doppler variable**

This method uses the Doppler shift of the received carrier signal, which is proportional to the velocity of the satellite-receiver along the LOS path. This is then converted to range-rate (the product of the Doppler shift and the carrier wavelength) to obtain the velocity component per satellite, which is combined across multiple satellites to estimate the receiver velocity vector.

In the receiver, the Doppler observable $D$ is reported for each tracked satellite, and the corresponding range-rate $\dot{p}_i$ contribution is expressed as,

$$\dot{p}_i = -\lambda D \tag{2.1}$$

where,

$\dot{p}_i$ is the satellite–receiver range rate

$\lambda$ is the carrier wavelength

$D$ is the Doppler frequency shift measured by the receiver

By combining the range-rate measurements from multiple satellites, it is possible to solve for the 3D velocity vector and the receiver clock drift. This method is widely used due to its real-time capability, but it is sensitive to multipath and requires careful handling of the receiver clock and satellite dynamics [84], [85]. A detailed formulation and implementation of the Doppler-based velocity estimation are provided in Chapter 3.

### b) Pseudorange differentiation

It is a method that estimates the receiver velocity by differencing the two consecutive pseudo-range measurements over time. It is easy to implement but noisier than Doppler-based velocity estimation, especially on the receiver embedded in smartphones, where the pseudorange noise is high [84]. In its simplest form, the line-of-sight range-rate for satellite $i$ between two epochs $t_1$ and $t_0$ is approximated as,

$$\dot{p}_i \approx \frac{\rho_i(t_1) - \rho_i(t_0)}{\Delta t} \tag{2.2}$$

where,

$\rho_i(t_1)$ and $\rho_i(t_0)$ are the pseudorange measurements at two consecutive epochs,

$\Delta t = t_1 - t_0$ is the time interval

The receiver velocity vector is obtained by combining range-rates from multiple satellites in a linear system similar to the Doppler velocity vector. This approach is simple to implement and does not require carrier-phase measurements. However, it is significantly more sensitive to measurement noise, especially in smartphone-based GNSS receivers, where pseudorange errors are substantial, leading to lower accuracy than Doppler- and carrier-phase-based velocity estimation techniques.

### c) Carrier Phase-based velocity estimation

Carrier phase methods use a raw carrier-phase measurement to compute the PVT solution. Among these, the ***Time-Differenced Carrier Phase (TDCP)*** technique is widely used for high-accuracy velocity estimation. The simplified carrier-phase measurement for a single signal is given by,

$$\phi_i(t) = \frac{\rho_i(t)}{\lambda} + N + \epsilon \tag{2.3}$$

where,

$\phi_i(t)$ is the carrier-phase measurement in cycles, for satellite $i$,

$\rho_i(t)$ is the corresponding satellite-receiver range expressed in metres, which includes all the modelled corrections,

$N$ is the integer ambiguity in cycles,

$\epsilon$ represents residual measurement noise and unmodelled errors.

By taking the difference between consecutive epochs, the integer-ambiguity term is eliminated, allowing the change in range to be estimated.

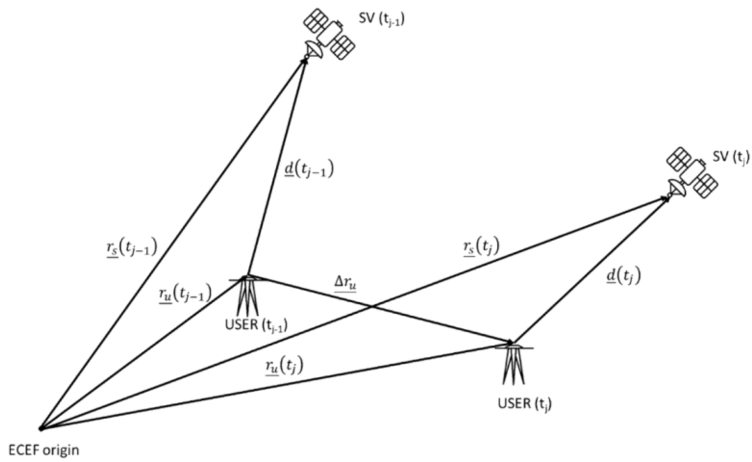


*Figure 2.16 Satellite-Receiver Geometry at two consecutive epochs*

TDCP computes the difference in the carrier phases of the same satellite at two epochs and identifies changes in the satellite receiver geometry over time (refer to Figure 2.16). It achieves mm-level accuracy and is particularly suitable for static or low-dynamic applications. So, TDCP has been adopted as a velocity estimation technique in this work, due to its suitability for low-dynamic applications, such as pedestrian velocity estimation, and its detailed implementation is provided in Chapter 4. [88].

The receiver velocity can be approximated as,

$$v = \frac{\Delta\rho}{\Delta t} \tag{2.4}$$

where,

$\Delta\rho$ is the change in the receiver-satellite range between two epochs

$\Delta t$ is the corresponding time interval

Carrier-phase measurements are often used within RTK. In ***Real-Time Kinematic (RTK)***, double-differenced carrier-phase measurements are used for the estimation, combining carrier-phase measurements from the rover and a base station. Two differences are formed: one between the satellites and the other between the receivers. This results in neglecting common errors such as satellite clock errors and atmospheric delays, leaving an exact measurement of a relative phase [85].

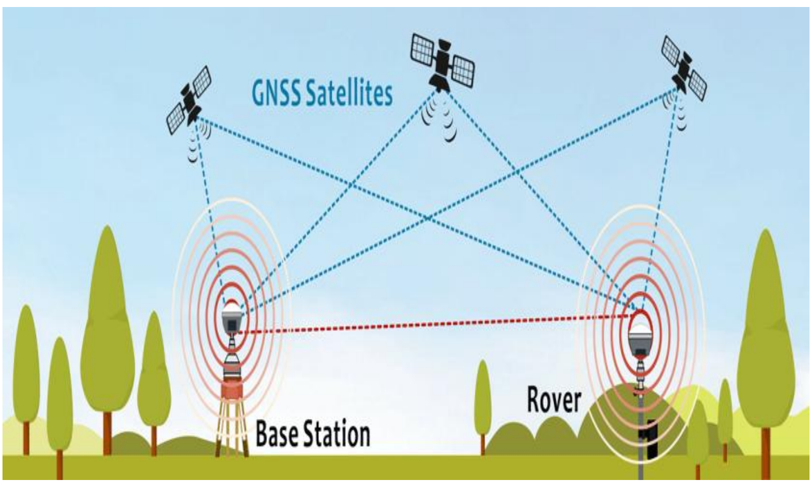


*Figure 2.17 RTK working principle*

**d) Kalman filter**

It is a recursive algorithm that uses and optimally combines all available GNSS measurement data and prior information about the system to estimate all required variables with a statistically minimal error. It uses all available measurements, regardless of accuracy, to assess the current value of the variables of interest. KF processes measurements sequentially and minimises estimation error by accounting for measurement noise and system dynamics. Furthermore, it eliminates the need to save and reprocess all past data with each new measurement, making it suitable for real-time applications [86], [87]. It is commonly used in GNSS receivers to improve the robustness and stability of velocity estimation.

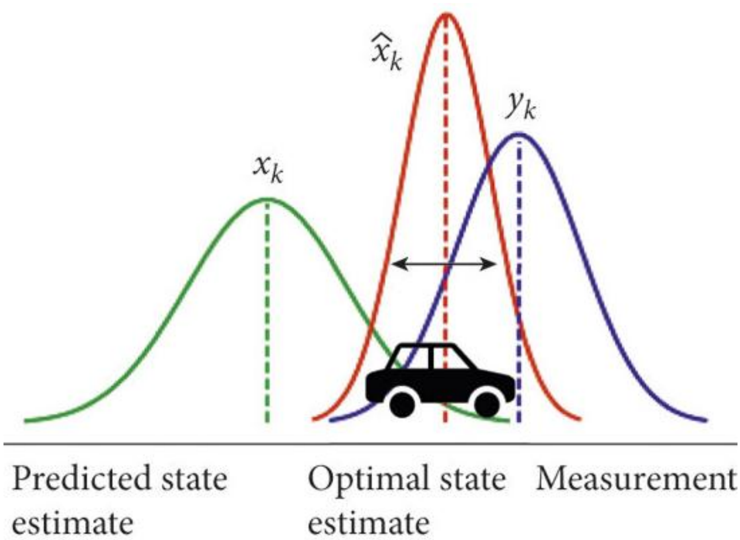


*Figure 2.18 Kalman Filter Estimation*

The GNSS-based velocity estimation discussed in this chapter provides a theoretical framework for the application-oriented analyses detailed in the following chapters. Among these, the Doppler-based approach is used in Chapter 3 for the meteorological verification of GNSS receivers employed for speed measurement, due to its suitability for laboratory-grade assessment of receiver performance. The Time-Differenced Carrier Phase (TDCP) is employed in Chapter 4 for the experimental characterisation of pedestrian velocity using smartphones, where its high precision makes it especially suitable for low-dynamics pedestrian applications.

# *CHAPTER 3*

# *METROLOGICAL VERIFICATION OF GNSS RECEIVERS FOR VELOCITY MEASUREMENT FOR SMART MOBILITY APPLICATIONS*

## 3.1 INTRODUCTION

This chapter describes a laboratory-grade testbed for evaluating the accuracy of GNSS-based speedometers. The testbed consists of a Novatel GPS-702-GG dual-frequency antenna, a USRP 2950R Software-Defined Radio platform from National Instruments, a Ublox M8T as a reference for tracking the number of satellites and other GNSS variables, and a host computer running MATLAB-based Raw IQ acquisition, as well as for post-processing algorithms for signal acquisition, tracking, decoding the navigation message, and estimating velocity using the Doppler method. By processing the raw in-phase and quadrature (IQ) samples entirely in software, this architecture provides complete observations at every signal processing stage, from the initial coarse Doppler search to the final stage of Doppler velocity and speed estimation.

The goal of the work reported in this chapter is to enhance the measurement system for sustainable mobility. While Chapter 1 introduced the concerns of smart urban mobility, such as emissions, urbanisations, road safety, and the policy targets established by the European Union, and Chapter 2 laid a theoretical basis for GNSS systems, their signal characteristics, and the receiver architecture, this chapter bridges the fundamental with metrological validation. It provides a methodology for increasing the credibility of speed data fed into Intelligent Transport Systems, speed enforcement networks, and urban mobility monitoring platforms.

### 3.2 ROLE OF SPEED MEASUREMENT IN SUSTAINABLE MOBILITY

The development of Intelligent Traffic Systems (ITS) depends on accurate speed monitoring, and one of the best ways to increase road safety is to implement reasonable speed restrictions [91]. The foundation of road safety is accurate speed measurement, which significantly impacts the likelihood of road accidents and the risk of injuries and fatalities. A substantial number of traffic accidents are caused by high speeds, according to the assessment conducted inside the safe system framework. Even a slight reduction in the mean speed can dramatically reduce the rate of major crashes and deaths [92].

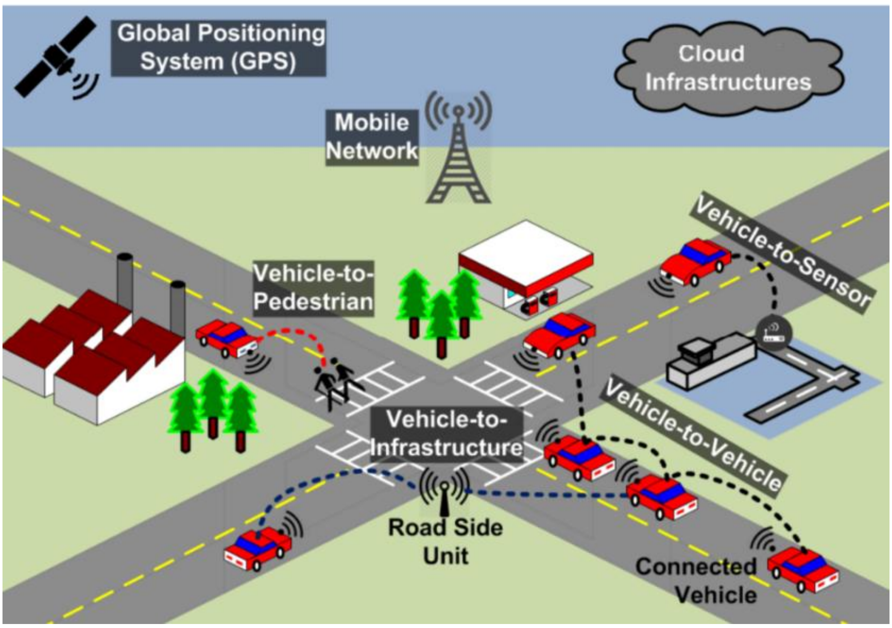


*Figure 3.1 Intelligent Transport System*

Given the strong correlation between speed and risk, a speed assessment is essential for developing environments that account for vulnerable road users, especially pedestrians and cyclists. Speed control is a strategy guided by innovative and sustainable transportation policy, not only to reduce road accidents but also to decrease congestion, energy use, and emissions [93]. Simulation-based research has shown that speed management measures, such as sensor-supported enforcement and variable speed restrictions, may significantly improve the safety performance metrics on the operational road segments. Sustainability concepts in the smart city emphasise protecting VRUs and redistributing street space [94].

### 3.3 GNSS FOR MODERN SPEED MEASUREMENT

Due to the widespread adoption of multiconstellation GNSS chipsets in mass-market smartphones and in-vehicle communication systems, almost every automobile and most road users now have access to satellite-based technologies. The ability of standard Android devices to provide carrier-phase and Doppler measurements enables sub-decimeter-per-second velocity estimates, demonstrating that specialised survey-grade receivers are no longer necessary for high-accuracy speed detection [95]-[98].

GNSS-based speedometers have several advantages for smart mobility: they don't need roadside fixed infrastructure like RADAR or inductive loops, and they operate globally wherever there is satellite visibility. Also, users don't need separate equipment, as GNSS receivers are already integrated into smartphones and are inexpensive [95], [99].

Doppler-based and Time-Differenced Carrier Phase (Chapter 3) techniques can be easily implemented in software on existing hardware, transforming smartphones and connected vehicles into accurate, infrastructure-free speed sensors that require only software rather than heavy public works for installation [96], [98]. Interest in using GNSS-equipped cars as mobile traffic monitoring probes has increased with the growth of autonomous and connected vehicles, as well as IoV concepts. To evaluate traffic conditions and predict congestion at the network scale, mobile crowd-sensing frameworks for the Internet of Vehicles (IoV) assume that vehicles provide position and speed data.

From an innovative and sustainable mobility perspective, GNSS-based speedometers are highly important because they enable scalable, infrastructure-free monitoring of both motorised and non-motorised traffic. This means that GNSS-driven and GNSS-based speed sensing, which are often combined with inertial and other smartphone sensors, support data-driven, low-cost, and quickly deployable measurement systems that align with the objectives of sustainable mobility [96],[99].

## 3.4 PRINCIPLE OF GNSS-BASED VELOCITY ESTIMATION

There are three primary methods that GNSS-based speedometers use to estimate the velocity on the Earth's surface. Still, they all rely on the same basic principle: measuring the change in the distance between the satellite and the receiver over time. The methods are:

a) Doppler-based estimation
b) Time-Differenced Carrier Phase Estimation
c) Position Differencing

Each of these methods has its own unique approaches, error sources, noise characteristics, and applications in innovative mobility systems [100], [101].

### 3.4.1 Doppler method for velocity estimation

The Doppler frequency shift is the change in the receiver frequency caused by the relative motion between the satellite and the receiver. In the raw

Doppler method, the Doppler shift is calculated as the difference between the receiver carrier phase frequency and the transmitted satellite signal frequency [102]. When a GNSS satellite and receiver move relative to each other, the receiver's carrier frequency $f_r$ is shifted from the transmitted signal frequency $f_s$ by a true Doppler term $f_d$ is directly proportional to the line-of-sight (LOS) relative velocity.

$$f_d = f_r - f_s \tag{3.1}$$

The general measurement model of the Doppler can be written as

$$\lambda D = \dot{\rho} + c\left(\delta\dot{t}_r - \delta\dot{t}_s\right) + \dot{I}_s + \dot{T}_s + \epsilon_\eta \tag{3.2}$$

where,

$\lambda$ is the wavelength of the GNSS carrier signal (m),

$D$ is the Doppler observable that is reported by the receiver, which is an estimate of the true Doppler frequency $f_d$ (Hz),

$\dot{\rho}$ refers to pseudorange rate (rate at which the satellite-receiver geometry changes) (m/s)

$c$ speed of light in vacuum (m/s)

$\delta t_r$ receiver clock drift (s/s)

$\delta t_s$ satellite clock drift (s/s)

$I_s$ rate of Ionospheric delay (m/s)

$T_s$ rate of Tropospheric delay (m/s)

$\epsilon_\eta$ Multipath and receiver noise (m/s)

The product $\lambda D$in this model expresses the Doppler measurement in range-rate units, typically in metres per second. The term $\dot{\rho}$ denotes the rate of change of the geometric distance between the satellite and the receiver and contains the information required for velocity estimation. This cannot be observed directly; it is derived from the satellite velocity, the receiver velocity, and the geometric relationship between them.

$$\dot{\rho} = (v_s - v_r)^T . \hat{e}_i \qquad (3.3)$$

where, $v_s$ is the Satellite velocity (will be known from Satellite ephemeris), and $v_r$ is the unknown receiver velocity, and $\hat{e}_i$ is the unit Line-of-Sight vector (LOS) from the satellite *s* to the receiver and is given as,

$$\hat{e}_i = \frac{r_i^s - r_r}{\left\| r_i^s - r_r \right\|} \qquad (3.4)$$

where, $r_i^s$ and $r_r$ are the position vectors of the satellite and the receiver, respectively.

Substituting (3.3), the geometric definition of $\dot{\rho}$, in the equation (3.2), the expanded Doppler observation for a single satellite becomes,

$$\lambda D = (v_s - v_r)^T . \hat{e}_i + c(\dot{\delta t_r} - \dot{\delta t_s}) + \dot{I}_s + \dot{T}_s + \epsilon_\eta \qquad (3.5)$$

where, $v_s$ and $\delta t_s$ are known from broadcast ephemeris, they can be moved to the Left-Hand side to form a corrected pseudorange rate $y_i$,

$$y_i = \lambda D - {v_s}^T . \hat{e}_i + c\dot{\delta t_s} \qquad (3.6a)$$

Rearranging 3.5 according to 3.6a, the observation becomes,

$$y_i = -\hat{e}_i . v_r{}^T + c\delta\dot{t}_r + \epsilon_\eta \tag{3.6b}$$

The Doppler observable $D$ reported by the receiver is an estimate of the true Doppler frequency shift $f_d$. Commercial GNSS-based speedometers measure D for each tracked satellite and convert it to a range rate for velocity estimation. The detailed formulation of the Doppler-based velocity estimation for a multi-satellite constellation and the least-square solution are developed in section 3.9.

### 3.5 Limitations of GNSS-based speedometers

Satellite ephemeris errors, clock inaccuracies, atmospheric delays, receiver clock drift, and multipath are significant sources of GNSS speedometer inaccuracies [100], [101]. Estimating the Doppler base velocity using multi-constellations can reduce high DOP errors, unlike single constellations.

***a) Multipath and Urban Canyon***

Strong building reflections in urban areas can result in significant multipath, which influences Doppler and amplitude measurements, introduces coding delay, and distorts LOS velocity estimations [101]-[103]. Multipath degrades both Doppler and TDCP velocity estimation, especially in crowded areas, leading to large Doppler fluctuations and phase rotations across frequency bands [103].

***b) Satellite geometry***

Satellite visibility also affects the estimation of velocity solutions. It means that when there are fewer satellites in view, or when they cluster in a similar direction, or when they are near the horizon, the receiver's velocity accuracy is distorted [101]. Especially in the urban environment, it leads to variations in the velocity levels.

***c) Receiver clock instability***

In all velocity estimation methods, receiver clock drift is unknown and must be estimated along with the three-dimensional receiver velocity [91]. It is important to note that the low-cost single-frequency receiver typically uses inexpensive crystal oscillators, leading to greater short-term frequency instability and higher Doppler shifts, which reduce velocity estimation accuracy.

Some studies show that integrity monitoring of the signal also reveals unmodeled clock behaviour that can mimic or mask measurement errors, making it more challenging to detect velocity deviations in safety-critical applications.

***d) Low-cost antenna limitations***

Several GNS-based speedometers use consumer-grade patch antennas, which have poor multipath rejection and also limit the bandwidth. This lowers the carrier-to-noise ratio and increases tracking jitter, especially when the antenna is tilted or partially blocked by another user’s body or vehicle structure, because patch antennas are sensitive to tilt [101], [103].

### 3.6 SOFTWARE DEFINED RADIO FOR GNSS VALIDATION

A controlled laboratory testbed helps investigate and address problems encountered by GNSS-based speedometers, such as multipath effects, satellite geometry, receiver clock instability, and antenna constraints. Using the USRP 2950R SDR platform, a high-quality NovAtel antenna, and a MATLAB-based post-processing method enables repeatable experiments that isolate each error source and measure its effect on velocity estimates derived from Doppler data. This controlled environment also allows the evaluation of tracking loop behaviour, Doppler noise sensitivity, and the impact of DOPs on velocity estimation, which cannot be reliably studied in the uncontrolled field settings.

From the perspective of sustainable mobility, network-wide mobility monitoring, eco-driving, traffic modelling, and congestion analysis all depend on improving the meteorological reliability of GNS-derived velocity. These applications rely on a stable and credible velocity estimate rather than enforcement-oriented measurements.

### 3.7 ARCHITECTURE OF THE TEST BED

Designing a testbed to evaluate the accuracy of the GNSS-based speedometers needs more than collecting live-sky data. It means it requires a system that can show its receiver's internal workings, uncover hidden failure mechanisms, and allow the experiment to be repeated under the same conditions, but this is not achievable with traditional field testing. This can be achieved through an architecture that combines hardware with a software-defined signal processing chain. So, the result will not only measure the performance but also explain why performance degrades under certain conditions.  SDR architecture offers a compelling alternative. SDR-based receivers provide complete insight into each step of the signal-processing pipeline by recording raw in-phase and quadrature samples and processing them completely in software. Because it allows for algorithmic experimentation under controlled testing, and in-depth examination of internal factors that commercial receivers usually hide [105], [106].

The testbed developed in this work adopts a hybrid approach of capturing live-sky signals using a high-quality antenna and a good receiver. gradable SDR front end, then the stored data is fed into a MATLAB-based post-processing algorithm. This method offers the transparency and reproducibility of laboratory-based testing while maintaining the reality of the sky data. Also, it allows the system to detect minor abnormalities that would be challenging to identify with a commercial receiver alone, such as velocity spikes observed during bad satellite geometry.

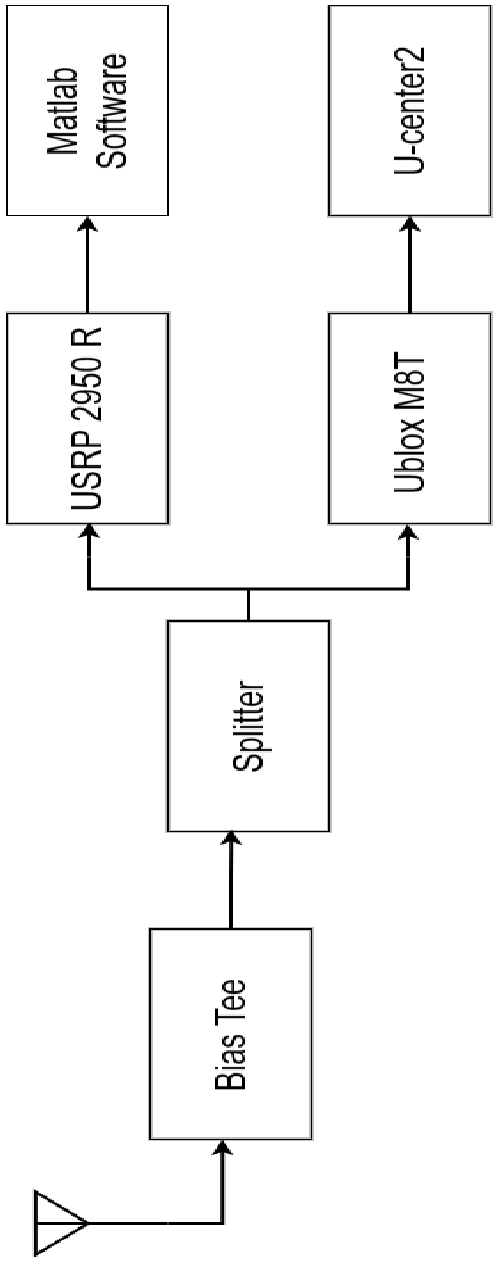


*Figure 3.2 A test bed for testing the accuracy of the speedometers*

### 3.7.1 Hardware components

The hardware presented in the test bed was a high-performance GNSS antenna, a bias tee, a National Instruments USRP 2950R SDR, and a host computer running the software receiver. Also, as a reference location, a U-blox 8T module has been added, and the RINEX files have been logged on the U-blox M8T. The key specifications of each hardware component are given below:

***a) NovAtel GPS-702-GG Dual Frequency Antenna***

The primary component of the testbed in NovAtel Antenna supports two frequency bands (L1 and L2) and the dual constellations of GPS and GLONASS. Its primary role is to capture RF signals transmitted by satellites [107]. A key characteristic of these antennas is their polarisation, which is typically RHCP to match the satellite signal. But the one used in this case was a Novatel GPS antenna (GPS-702 GG), which is a high-precision, dual-frequency, dual-constellation GNSS antenna. It is capable of capturing signals of the GPS constellation. The antenna's design emphasises a highly stable phase centre and exceptional multipath rejection, making it a robust solution for demanding positioning applications.


*Figure 3.3 Novatel GPS Antenna*

***b) Bias Tee***

The second component in line is the Bias Tee. It is a two-port electronic component that injects DC power into the RF signal line without affecting the RF signal itself. It is a key component in many electronic applications, particularly for powering devices such as LNAs and antennas. Bias tee uses a capacitor and an inductor.

It consists of three primary ports:

a) RF Port: It is designed to pass both the HF RF signal and the DC.

b) DC Port: It is used to apply the DC voltage and current.

c) RF + DC Port: This is the combined port where the RF signal and the DC are mixed.


*Figure 3.4 Bias Tee*

***c) NI USRP 2950R SDR***

USRP 2950R is a reconfigurable Software Defined Radio (SDR Platform), designed for prototyping and deploying high-performance wireless communication systems. It has a wide frequency range of 50 MHz to 2.2 GHz and features two independent transmit and receive channels for full-duplex operation. The high-bandwidth range enables it to process a large portion of the radio spectrum. This model also has an integrated GPS-Disciplined Oscillator, called GPSDO, for a time and frequency reference. This means its internal clock is constantly corrected by GPS signals, providing excellent frequency stability and time accuracy for applications that require high precision synchronisation.

The USRP digitises the receiver's analogue RF signal using a 16-bit ADC and streams the resulting I/Q samples to the host computer over a high-speed Ethernet interface. For GPS L1 signal reception, the local oscillator is tuned to the centre frequency of the GPS L1 carrier, 1575.42 MHz, and a sampling rate of several megahertz is chosen to satisfy the Nyquist criterion for the signal. The built-in FPGA architecture and UHD profile are similar to those of the Ettus X310.


*Figure 3.5 Front Panel of NI USRP 2950R*

***d) Host Computer***

The Host computer stores the raw I/Q data and executes the software-defined receiver. In this work, the receiver is based on an Open platform called SoftGNSS, initially developed by Borre et al. [105] and later enhanced by Zhang. MATLAB is used for acquisition, tracking, and navigation processing, providing a flexible environment for algorithm development and visualisation. The host computer must support high data throughput and sufficient computational power to process millions of samples per second during the acquisition and tracking. But this provides only the Position and not the velocity. Later, the code was modified to support Doppler extraction and to estimate both the receiver's velocity and speed.

***e) U-blox M8T timing receiver***

It is a specialised GNSS receiver module, designed for timing applications. Unlike the standard GPS receiver in a car or phone, which focuses on location, the M8T is optimised for providing extremely accurate time and frequency signals, even in challenging signal environments. The Ublox M8T module supports multi-constellation reception, including GPS, Galileo, GLONASS, and BeiDou. It can provide a PPS signal with an accuracy of ≤20 ns or better under clear-sky conditions. M8T delivers a highly stable time pulse, which can also be used to discipline the clock of another device, such as the USRP 2950R. The Ublox GNSS evaluation kit includes UART, USB, I2C/SPI interfaces. The software tool u-centre is used to produce outputs from the processed raw GNSS measurements. It is mainly used for configuration, data visualisation, and analysis. The Ublox M8T used, and the GUI of u-centre are given below:

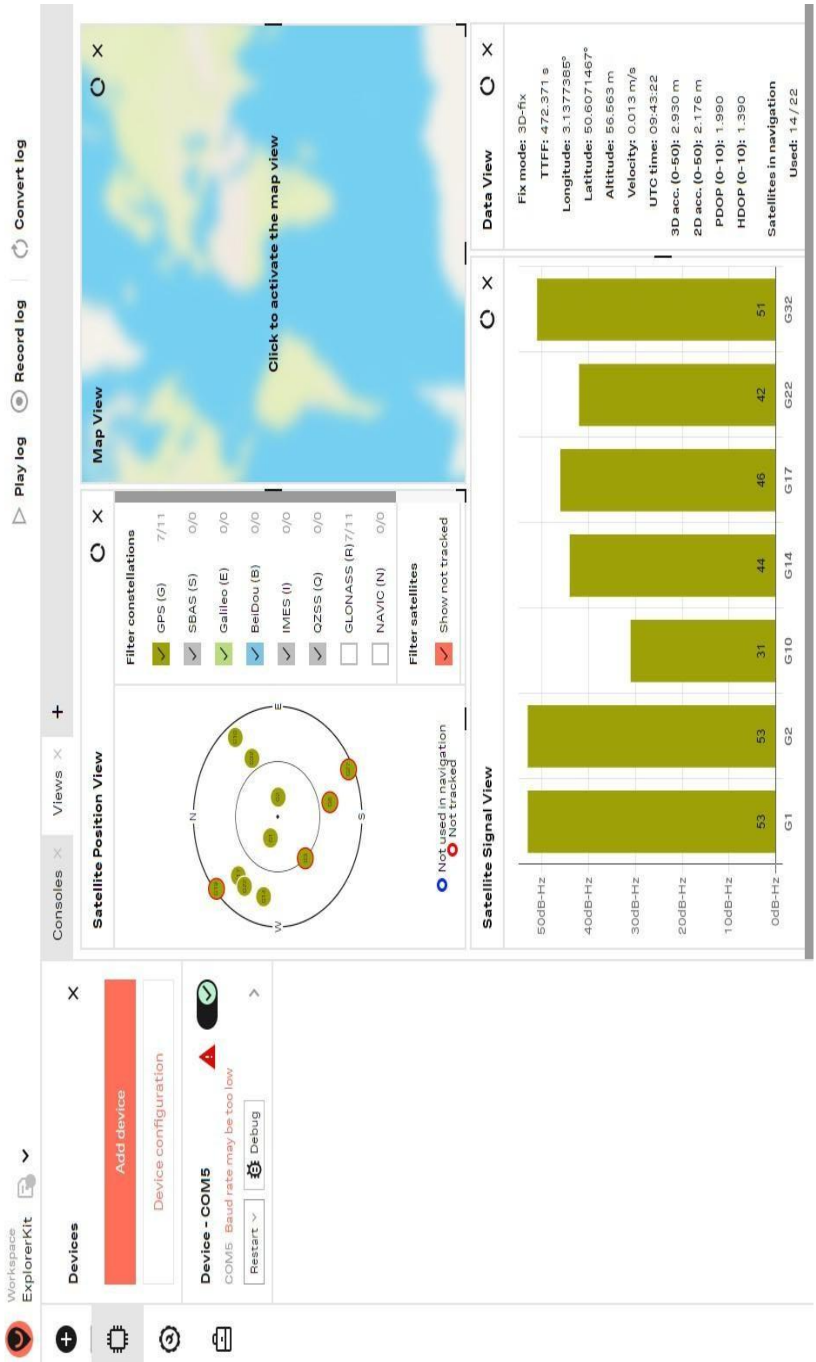


*Figure 3.6 GUI of UCentre2*

### 3.7.2 System Integration

The components are integrated into a signal chain that starts with the NovAtel antenna feeds, which feed the signal to the bias tee, which injects DC power into the coaxial line. The combined RF+DC signal is delivered to the USRP's RF input port, where it is downconverted, filtered, and digitised. The resulting I/Q samples are streamed to the host computer for storage and offline processing. In parallel, the U-blox M8T receives the same signal from the antenna via a splitter and provides an independent timing and navigation reference.

This type of architecture offers several advantages. First, it ensures repeatability: a dataset can be replayed indefinitely after it is recorded, allowing the testing of different algorithms or configurations under the same conditions. Secondly, it provides transparency, so that every internal variable, starting from correlator output to Doppler estimate outputs, can be examined from the result section. Lastly, it helps to understand anomalies like ill-conditioned geometry or tracking loop instability in detail, enabling targeted improvements to the receiver.

## 3.8 SOFTWARE DEFINED GNSS RECEIVER PROCESSING CHAIN

A software-defined GSS receiver is more than just a collection of algorithms. Unlike commercial GNSS receivers, which conceal their internal processing logic behind firmware, an SDR architecture makes every stage transparent, from satellite search to the final computation of Position, Velocity, and Time. This transparency is crucial not only for non-navigational tasks but also for explaining system behaviour. In this work, which studies the stability of Doppler-based velocity estimation, the ability to examine correlator outputs, tracking-loop behaviour, and navigation-matrix conditioning was essential.

### 3.8.1 Overview of the workflow

a*) Raw Data acquisition*

The process begins with the RF front end acquiring raw data from the satellites. This process converts the analogue radio signals into digital data, often represented as in-phase (I) and quadrature (Q) samples.

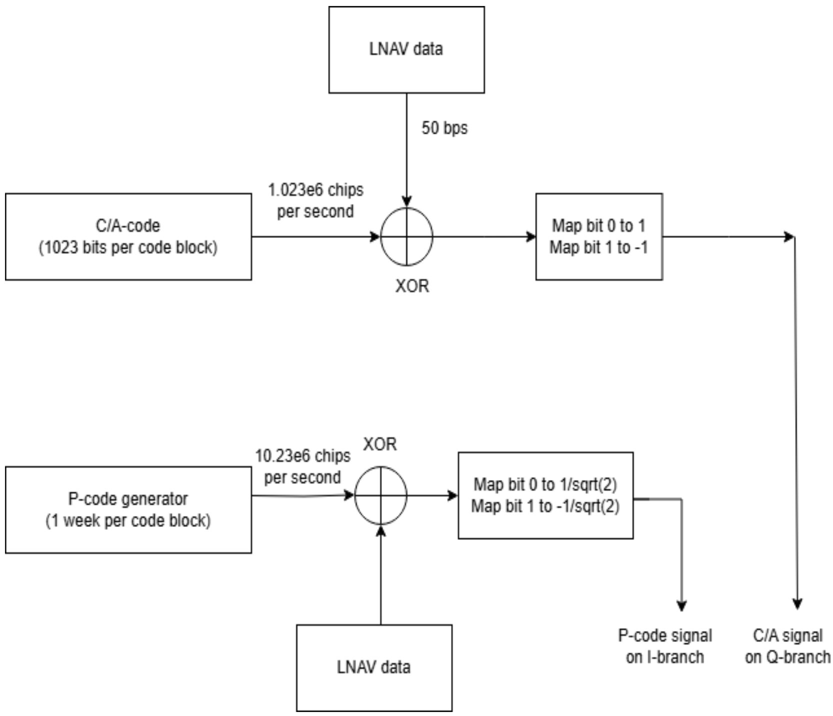


*Figure 3.7 GPS Legacy Signal Structure*

Raw IQ data consists of the unprocessed complex-valued baseband signal captured by the receiver's front end. This data is the most fundamental representation of the GNSS signal, as it is received from the satellites before any signal processing. When saved to a file, this data is typically stored as a binary stream of interleaved In-phase and Quadrature values, such as IQIQIQ…., to conserve storage space. The values can be written using either 16-bit signed integers or 32-bit floating-point numbers. For example, in the GPS legacy signal, the spreading codes are generated by placing the P-code waveforms on the I-branch and the C/A code on the Q-branch.

***GURSA Raw signal Acquisition MATLAB Software*** is used for IQ data recording, which can store IQ data in .dat format (representing raw GNSS data with IQs) and in complex integer-16 format. A Research engineer, Tmazirte, and a team from Gustave Eiffel University have designed this software.

The centre frequency is set to 1575.42 MHz, which is the frequency of the GPS L1 carrier signal. And the bandwidth is set by the Master clock rate and decimation factor. The master clock rate value for USRP 2950R is 200 MHz or 184.32 MHz [110]. The algorithm also generates a report on the acquisition, including the start time, the time the recording was stopped, the test location, whether a reference system was used, and so on (refer to Figure 3.8).

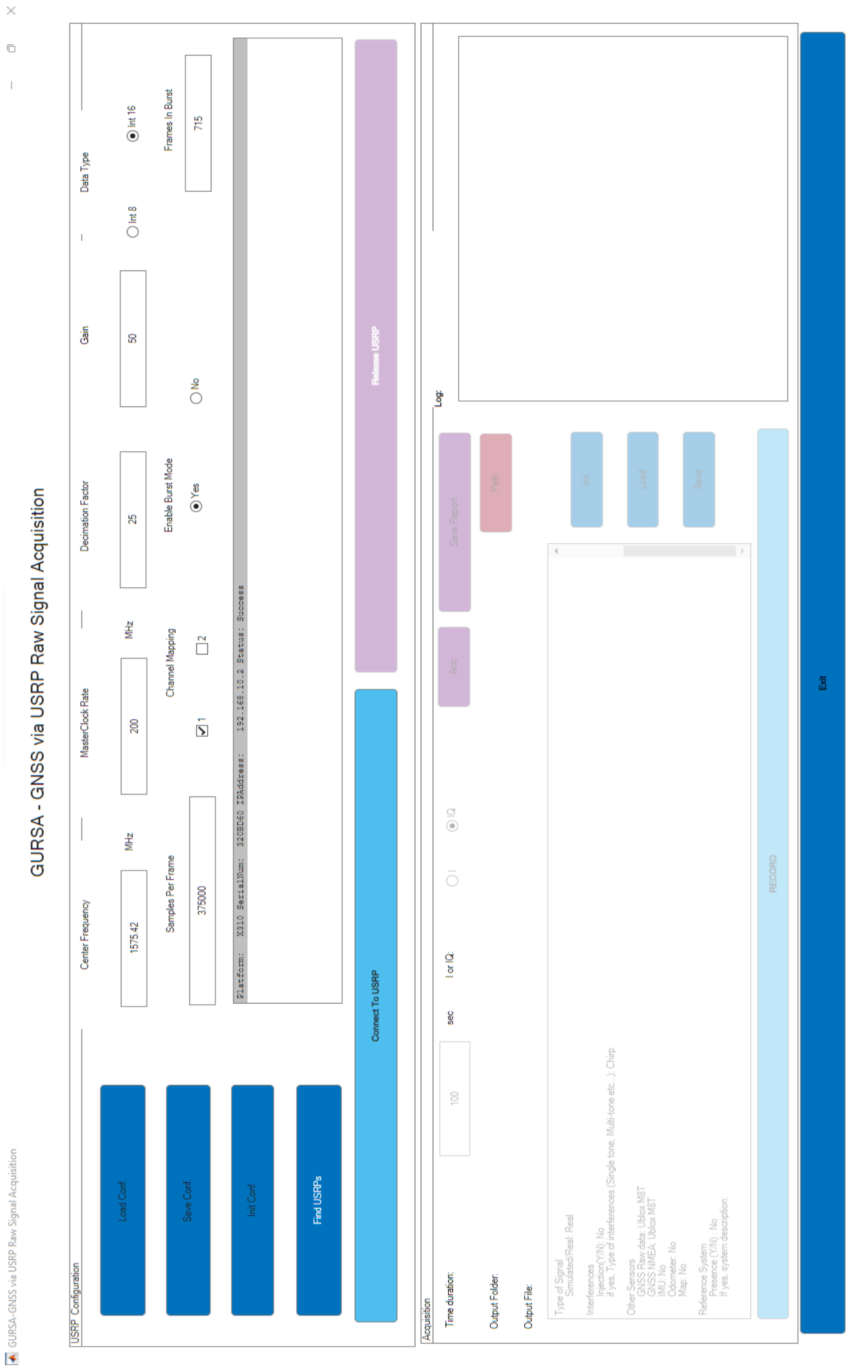


*Figure 3.8 Window for setting all the acquisition parameters*

```
Start Recording: 21 07 2025, 11:30:15.514
End Recording: 11:31:47.221
File Saved: 11:31:55.624
Saved Samples: IQ
Precision: Int16
Samples: 480000000
Duration: 60s
Repository: C:\Users\cristal\Desktop\Git_IQ_Project\iqproject\SoftGNSS\IQ_Samples\21072025\RawData_Acquisition_D21_07_2025_T_11_30_15_IQ_Int16.dat

Descrition

      Location
            City: Villeneuve d'Ascq
            Country: France

      Environnement
            OpenSky (Y/N): Yes
            Urban (Y/N): No
            SubUrban (Y/N): No
            Forests (Y/N): No
            Bridges (Y/N): No

      Type of Signal
            Simulated/Real: Real

      Interferences
            Injection(Y/N): No
            if yes, Type of interferences (Single tone, Multi-tone etc...): Chirp

      Other Sensors
            GNSS Raw data: Ublox M8T
            GNSS NMEA: Ublox M8T
            IMU: No
            Odometer: No
            Map: No

      Reference System
            Presence (Y/N) : No
            If yes, system description:


%%%%%%%%%%%%%%%%%%%%%%%%%%%%%%%%%%%%%%%%%%%%%%%%%%%%%%%
            Eventual overruns
%%%%%%%%%%%%%%%%%%%%%%%%%%%%%%%%%%%%%%%%%%%%%%%%%%%%%%%


%%%%%%%%%%%%%%%%%%%%%%%%%%%%%%%%%%%%%%%%%%%%%%%%%%%%%%%
            Acquired Satellites
%%%%%%%%%%%%%%%%%%%%%%%%%%%%%%%%%%%%%%%%%%%%%%%%%%%%%%%

Skip Step: 500ms
Acquition Time: 4ms
Skipped Time For Acquisition:       0ms

Number of SVs found: 6

            SV      SNR    DOPPLER   CODE_DELAY

             1    37.95     -1500         4116
             2    39.12       500         5428
            14    20.23       500         7221
            17    33.76     -3000         4903
            22    25.58      -500         2389
            32    36.46       500         2444

11:33:33.229 - Report Successfully Written
```

*Figure 3.9 Details about the tracked Satellites, the location, and other parameters*

The output plot of the raw signal acquisition is given in terms of the bandwidth used (Figure 3.10)

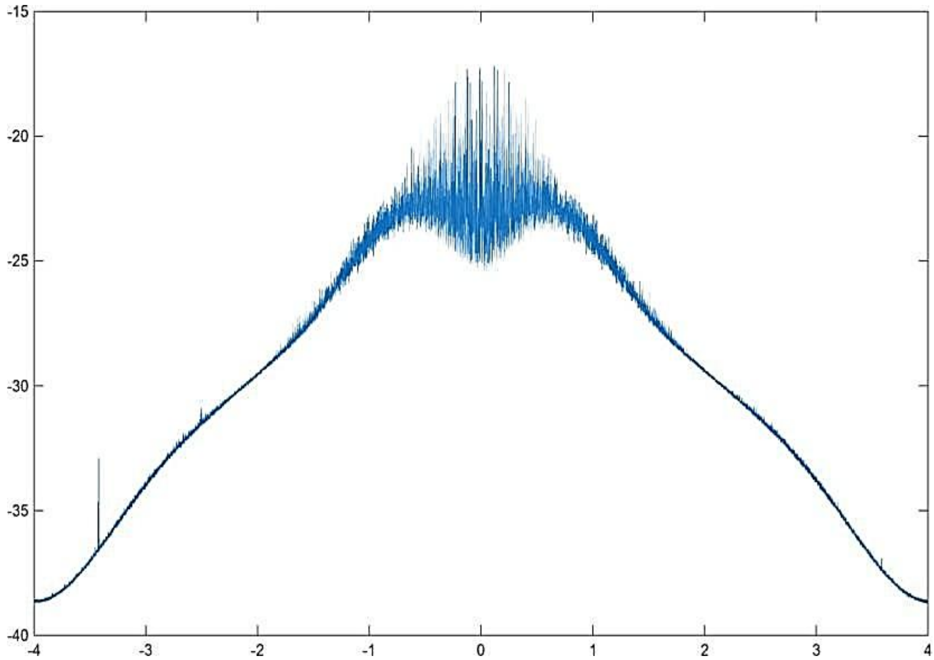


*Figure 3.10 Frequency domain plot with a sharp peak at the central component with a bandwidth of 8 MHz*

***b) Post-Processing Algorithm***

The post-processing algorithm is an open-source code by Prof. Xin Zhang [115]. The test bed's signal processing chain follows the classical structure of a GNSS receiver: Acquisition, Tracking and Navigation Processing, but it replaces the dedicated hardware with flexible software elements. This approach is widely adopted in academic research because it enables algorithmic experimentation, controlled testing that can be repeated, and detailed analysis of internal variables [105], [106]. The Software-defined implementation of these steps, with their established status in the literature [105], provides a level of analytic depth rarely possible with hardware receivers. Each test is described below, with a focus on the aspect relevant to velocity estimation and the detection of ill-conditioned solutions.

***1) Signal Acquisition***

The receiver's initial step, decoding the incoming raw I/Q samples, is known as Signal Acquisition. It tracks all visible satellites and provides a rough estimate of the two most important parameters.

- *Code Delay:* The time delay of the pseudorandom code
- *Doppler Delay:* The shift in the carrier frequency due to the relative motion of the receiver to the satellite.

The acquisition process is carried out in a two-dimensional grid, with components for code delay and Doppler delay. For GPS L1 C/A signals, the code delay spans one whole 1023-chip period, while the Doppler delay tries to cover $\pm 10$ kHz in steps of 500 Hz. The receiver tracks the incoming signal using the locally replicated PRN code and carrier. If they perfectly correlate with each other and the correlation exceeds the set detection threshold, it indicates that the satellite is present and can proceed to signal tracking.

Under clear-sky conditions, the acquisition stage typically identifies 4 to 8 GPS satellites with sufficient Carrier-to-Noise Density ($C/N_0$). Satellites with $C/N_0$ below 30 dB-Hz are not considered, especially those at low elevation angles or partially blocked by buildings and trees. The quality of the acquisition directly influences the performance of the tracking loops, which are entirely dependent on initial coarse Doppler and coarse code delays to converge and maintain the "lock on" with the satellite [111]-[114].

***2) Signal Tracking***

Once the satellite is acquired, the receiver proceeds to the tracking stage, where it continuously refines the signal to estimate fine-code and Doppler delays. Code tracking loop aligns the PRN code phase of the local replica of the incoming signal. The input to the code discriminator loop consists of the in-phase and quadrature components of the early and late signal alignments.

Tracking is performed using two tracking loops:

- *Delay Locked Loop (DLL)* for code tracking
- *Phase Locked Loop (PLL) or Frequency Locked Loop (FLL)* for carrier tracking.

These loops maintain the alignment between the received signal and the receiver-generated PRN.

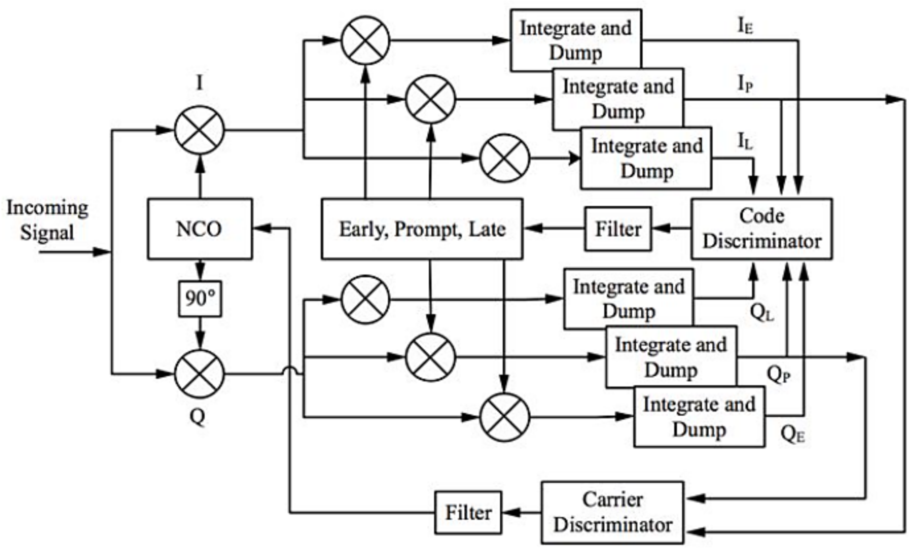


*Figure 3.11 Block diagram of tracking loops [111]*

The incoming signal is first mixed with a locally generated carrier produced by a Numerically Controlled Oscillator (NCO). It uses two branches, In-Phase (I) and Quadrature (Q), simultaneously. The I component is multiplied directly by the NCO signal, while the Q component shifts its phase by 90°. This operation removes most of the

Doppler and carrier frequency, producing the complex baseband signal *I(t)* and *Q(t)*. Then this baseband is sent for code correlation.

***Early, Prompt and Late Code correlation***

To track the code phase, the receiver generates three versions of the PRN code,

*Early (advanced by half a chip), Prompt (Exactly aligns), and Late (Delayed by half a chip).* Each code replica is then multiplied with both I and Q components, producing six correlation branches.

$$I_E,\ I_P,\ I_L \quad and \quad Q_E,\ Q_P,\ Q_L$$

These branches later pass through Integrate-and-Dump accumulators, which integrate over one code period (1ms for the GPS L1 C/A signal). The result is a set of low-rate correlator outputs that summarise the signal energy in each branch of both the In-phase and Quadrature components.

***Code Tracking Loop (DLL)***

The code-tracking loop, i.e., the Delayed Locking Loop, uses the Early and Late correlator outputs to estimate the code phase error. A widely used non-coherent discriminator is

$$\Delta_{code} = \frac{\sqrt{I_E^2 + Q_E^2} - \sqrt{I_L^2 + Q_L^2}}{\sqrt{I_E^2 + Q_E^2} + \sqrt{I_L^2 + Q_L^2}} \tag{3.7}$$

The output of this code discriminator then passes through the loop filter, which controls the loop bandwidth and the stability, and is followed by Code NCO [115], [116].

***Carrier Tracking Loop (PLL)***

The carrier loop uses the Prompt correlator's outputs, $I_P$ and $Q_P$, respectively. A common PLL discriminator is the arctangent phase detector:

$$\Delta_{carrier} = \tan^{-1}\left(\frac{Q_P}{I_P}\right) \tag{3.8}$$

The filtered output adjusts the Carrier NCO before refining the signal to obtain the carrier frequency and phase. The discriminators are coupled: the carrier loop provides Doppler estimates that stabilise the Code loop, while the code loop ensures proper alignment of the correlator outputs, improving carrier phase estimation.

***Doppler Extraction***

The carrier NCO frequency maintained by the loop is the primary observable for Doppler-based velocity estimation. At steady state, the NCO frequency is the sum of the Intermediate Frequency (IF) and the true Doppler shift.

$$f_{NCO} = f_{IF} + f_d \tag{3.9}$$

So, rearranging eqn (3.9) it to obtain the Doppler frequency shift, it becomes

$$f_d = f_{NCO} - f_{IF} \tag{3.10}$$

The Doppler estimate is available for each tracked satellite at each tracking update, typically every millisecond, providing a high-rate measurement of satellite-receiver range rate. The conversion of Doppler frequency to range rate is given in the formula

$$\dot{p}_i = -\lambda * D \tag{3.11}$$

Under favourable conditions, such as an open-sky view, satellites are more spread across the sky, reducing the residual Doppler to a few Hz, corresponding to a velocity precision of millimetre per second [117], [118].

Tracking loops are particularly vulnerable to multipath and non-line-of-sight signal reception, which can distort the received signal and cause the loop to lock onto a reflected path. Such distortions directly affect the Doppler estimate and can introduce biases or oscillations in the velocity solution.

***3) Navigation processing***

After stable tracking is achieved, the receiver demodulates the 50-bps navigation message, which contains satellite ephemeris parameters, satellite clock correction terms, Ionospheric model coefficients, and health and status flags. This data helps determine the satellite's position and velocity at any given epoch with cm-level accuracy. These are the variables that are important for estimating the receiver's position and velocity.

### 3.9 DOPPLER-BASED VELOCITY ESTIMATION

Velocity is one of the fine quantities that GNSS systems can provide. Unlike positions, which depend on solving a multi-lateration problem with layers of geometric sensitivity, velocity can be derived directly from the Doppler shift of the carrier signal. This makes the Doppler-based velocity estimation both clean and precise under the right conditions. Doppler measurements can outperform position-differencing methods by an order of magnitude, achieving cm-level accuracy in open-sky conditions [119], [120]. Yet the results showed that the same method can become unstable or even meaningless when satellite geometry degrades.

#### 3.9.1 Principles of Doppler

In GNSS systems, the satellite serves as the source, and the receiver as the observer. As the satellite approaches, the receiver's GNSS signal frequency is higher than the transmitted frequency, indicating a positive Doppler shift. On the other hand, when the satellite is receding from the observer, the received signal frequency is lower than the transmitted signal frequency, a phenomenon known as the negative Doppler shift.

The frequency shift is caused by the motion of the satellite and the receiver as they are moving relative to each other along the LOS, and the received frequency is given as follows:

$$f_r = f_s\left(1 - \frac{v_{rad}}{c}\right) \tag{3.12}$$

where,

$c$ is the speed of the light

$v_{rad}$ Is the relative radial velocity, which is precisely the rate of change of the range.

$$v_{rad} = (v_s - v_r).\hat{e}_i \tag{3.13}$$

Substituting equation (3.13) into equation (3.12), we get,

$$f_r = f_s\left(1 - \frac{(v_s - v_r).\hat{e}_i}{c}\right) \tag{3.14}$$

From equation (3.1), the Doppler is given as, $f_d = f_r - f_s$

$$f_d = f_r - f_s = -\frac{f_s}{c}(v_s - v_r).\hat{e}_i \tag{3.15}$$

Rearranging the equation (3.15) according to (3.13),

$$\Delta f = -\frac{v_{rad}}{c} * f_s \tag{3.16}$$

The Doppler shift of a satellite signal is directly proportional to the relative radial velocity, which is the instantaneous velocity component projected onto the Line of Sight between two elementsThe negative sign indicates that a positive radial velocity produces a negative frequency shift when satellites are moving away from the receiver.

The wavelength of the GPS L1 signal, which has a frequency of 1575.42 MHz, is 0.1903 m. This means a 1 Hz Doppler shift corresponds to a range-rate change of roughly 0.19 m/s. Since modern tracking loops can resolve Doppler shifts within a few Hz, and sometimes even a fraction of Hz, the precision of the receiver's velocity can reach the millimetre-per-second level under very favourable environmental conditions [106]. This is one of the reasons why Doppler-based velocity estimation is so valuable for smart mobility applications. But as later sections show, Doppler measurements are weak in poor satellite geometry.

### 3.9.2 Observation Model

By measuring the Doppler shift from multiple satellites simultaneously, the receiver can estimate its 3D velocity vector and clock drift. With four or more satellites, one solves the equation using the least-squares method or a Kalman filter for the velocity and clock rate. The fundamental of observables is pseudorange rate, which represents the derivative of the pseudorange measurements. For the i-th satellite, the pseudorange rate $\dot{p}_i$ can be expressed as,

$$\dot{\rho}_i = (v_s - v_r)^T . \hat{e}_i + c(\dot{\delta t}_r - \dot{\delta t}_s) + \xi \qquad (3.17)$$

where,

$v_r$ is the unknown receiver velocity vector (m/s)

$v_r$ is the satellite velocity vector (m/s)

$\dot{\delta t}_r$ is the unknown rate of change of the receiver clock bias (s/s)

$\dot{\delta t}_s$ is the rate of change of the satellite clock bias (s/s)

$\hat{e}_i$ is the LOS unit vector from satellite-i to the receiver

$r_i^s$ *and* $r_r$ are the positions of the satellite and the receiver, respectively.

Equation (3.17), states that the observed pseudorange rate is the projection of the relative velocity onto the line-of-sight, along with the term accounting for a receiver clock drift.

The range rate measurements required to derive the receiver's velocity information are collected within the GNSS receiver in two ways. The first method uses the raw Doppler measurements, which are the direct frequency-error outputs of the tracking loop discriminators, typically from the PLL or the FLL. The second way is more precise, the TDCP method, which calculates the rate of change of the integrated carrier phase.

To calculate the receiver velocity vector and the clock drift, we need observations from at least four satellites. This produces an overdetermined system of linear equations, which is typically solved using the LSE. In a complex real-time system, this velocity solution is often incorporated into a filtering architecture, such as Kalman Filtering or Extended Kalman Filtering. The quality of the Doppler-derived velocity solution is determined by two factors: Signal integrity and update rate. Some studies have found that dense multipath conditions significantly affect Doppler estimates and velocity solutions. Multipath signal affects the detected signal's PSD, implying that the tracking loop is attempting to lock onto a distorted, composite frequency tone rather than the true LOS Doppler shift. This distortion produces incorrect Doppler estimates and poorly derived Doppler velocity solutions, thereby limiting solution accuracy in urban and complex terrain. Along with this multipath error, several other errors must be considered, including clock errors, ephemeris errors, atmospheric delays, receiver noise, and the GDOPs.

Rearranging equation (3.17) to linearise the model, we obtain

$$\dot{\rho}_i = (v_s)^T . \hat{e}_i - (v_r)^T . \hat{e}_i + c\dot{\delta t_r} - c\dot{\delta t_s} + \xi \qquad (3.18)$$

Defining the corrected observation and moving the known quantities to one side, consistent with equation 3.6a in section 3.4, equation (3.18) changes as,

$$y_i = \lambda D - {v_s}^T . \hat{e}_i + c\delta\dot{t}_s \tag{3.19}$$

Substituting equation 3.19 in 3.18, the linearised observation becomes,

$$y_i = -\hat{e}_i . {v_r}^T + c\delta\dot{t}_r + \epsilon_\eta \tag{3.20}$$

The single satellite contains four unknowns, the receiver's 3D velocity vector $v_r$ and the $\delta t_r$.

$$x = \begin{bmatrix} v_x \\ v_y \\ v_z \\ c\delta\dot{t}_r \end{bmatrix} \tag{3.21}$$

where

$[v_x, v_y, and\ v_z]$ are the velocity of the receiver in the ECEF coordinate frame.

$\delta\dot{t}_r$ is the receiver clock bias.

Given the condition that four or more satellites should be available to estimate the r clock drift. Building the geometry matrix $H_v$ to estimate the vector $x$ using Least Squares Estimation (LSE), considering that four or more satellites, the linear system becomes,

$$y = H_v x + \xi_\eta \tag{3.22}$$

The geometry matrix $H_v$ contains the line-of-sight unit vectors and a column of $c$ for the clock drift term. The structure $H_v$ a central role in determining the stability of the velocity solution. When the satellites are spread across the sky, $H_v$ It is well-conditioned, and the velocity estimation is stable. When the satellites are clustered, $H_v$ becomes ill-conditioned, and the solution becomes sensitive to noise, resulting in erratic velocity.

$$y = H_v x \tag{3.22a}$$

Expanding it for multiple satellites, we get,

$$\begin{bmatrix} y_1 \\ y_2 \\ y_3 \\ y_4 \\ . \\ . \\ . \\ y_n \end{bmatrix} = \begin{bmatrix} -\hat{e}_{1,x} & -\hat{e}_{1,y} & -\hat{e}_{1,z} & c \\ -\hat{e}_{2,x} & -\hat{e}_{2,y} & -\hat{e}_{2,z} & c \\ -\hat{e}_{3,x} & -\hat{e}_{3,y} & -\hat{e}_{3,z} & c \\ & . & & \\ & . & & \\ & . & & \\ -\hat{e}_{n,x} & -\hat{e}_{n,y} & -\hat{e}_{n,z} & c \end{bmatrix} \begin{bmatrix} v_x \\ v_y \\ v_z \\ \delta t_r \end{bmatrix} \tag{3.23}$$

The standard approach to solving the velocity estimation problem is Ordinary Least Squares, given as,

$$\hat{x} = (H_v^{\wedge T} H_v)^{-1} H_v^{\wedge T} y \tag{3.24}$$

But the estimator is well-known for its vulnerability; it is extremely sensitive to the conditioning of the matrix $H_v^{\wedge T} H_v$. When the satellite geometry is poor, the matrix becomes nearly singular, and its inverse amplifies the measurement noise by several orders of magnitude. This can produce wildly unstable velocity estimates, including the extreme values observed in this study.

The sensitivity of the estimator to ill-conditioning is not unique to GNSS, but it is a fundamental property of the Least-Squares-Estimation (LSE). Several studies have mentioned the issue of inverting near-singular matrices, which can lead to solutions dominated by noise rather than the real signal [121], [122]. In GNSS, this issue is caused by the fact that satellite-receiver geometry isn't in the receiver's control and is unpredictable, especially in urban environments.

The test has been performed using the developed test bed under stationary conditions at the ESPIRIT building of the University of Lille, France.

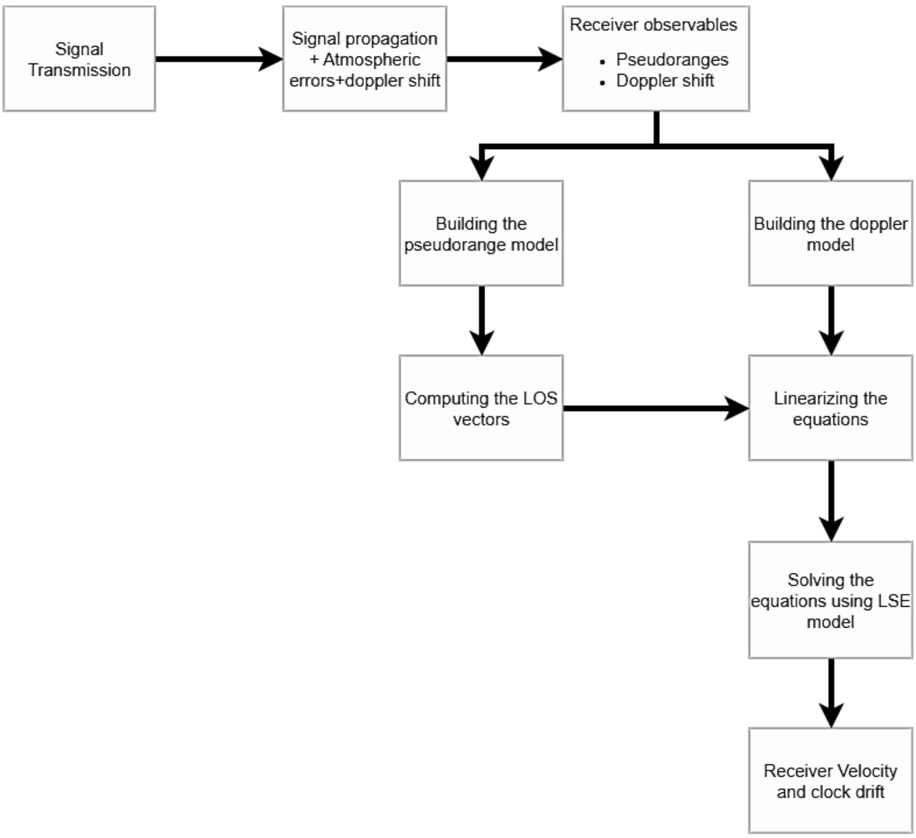


*Figure 3.12 Flowgraph for Doppler-based velocity estimation*

## 3.10 MEASUREMENT RESULTS

The frequency-domain plot (refer to Figure 3.13) provides a visual representation of the RF signal's energy distribution across the frequency range. The plot is wide, bell-shaped, and centred around 0 MHz. The second subplot is the Histogram of I and Histogram of Q components, respectively. The data clusters around two distinct values, which are roughly symmetrical across the y-axis.

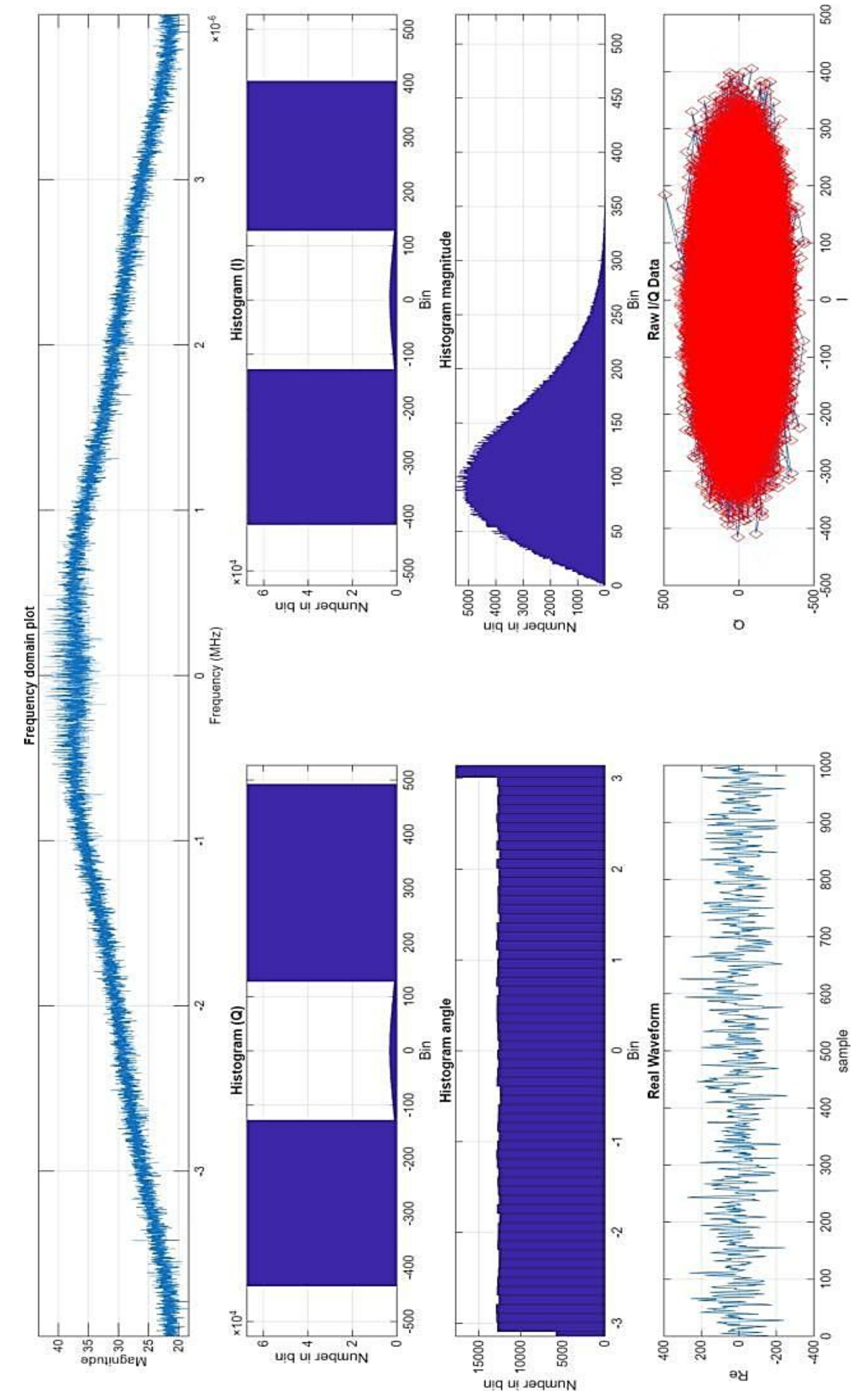


*Figure 3.13 Frequency Domain plot of GPS L1 Signal*

The histogram angle plot shows a relatively uniform distribution of the signal's phase. This is expected for a raw, undemodulated signal dominated by noise, since its components' phases will be randomly distributed. The histogram of magnitude plot displays a distribution with a peak near the origin that tapers off and is left-skewed, with a key signature of a magnitude-noisy signal. Raw IQ data is a scattered, dense, elliptical plot that visualises the I/Q data points in the complex waveform, with the I and Q components represented on the horizontal and vertical axes, respectively. The final subplot: Real waveform is the real part of the complex samples over time.

The acquisition plot covers PRNs 1-32. Each bar shows an acquisition metric for the corresponding PRN. Green bars indicate that the SV passed the detection threshold, meaning the satellites are just visible, while blue bars show satellites that did not. The green bars represent satellites with good C/N0, whereas the blue bars are either occluded satellites or missed due to low SNR.


*Figure 3.14 Acquisition results with 4 Satellites in visibility*

The plot (refer to Figure 3.15) delves into the tracking loops, correlation functions, and discriminator outputs that enable the receiver to maintain signal lock and precisely demodulate the navigation message. This phase is crucial for transforming coarse acquisition results into the precise measurements required for the position fix. This repeats for every visible or acquired satellite. In this case, tracking occurred for PRNs 1, 2, 17, and 32. The following is the figure for correlator outputs of Satellite ID PRN 2.

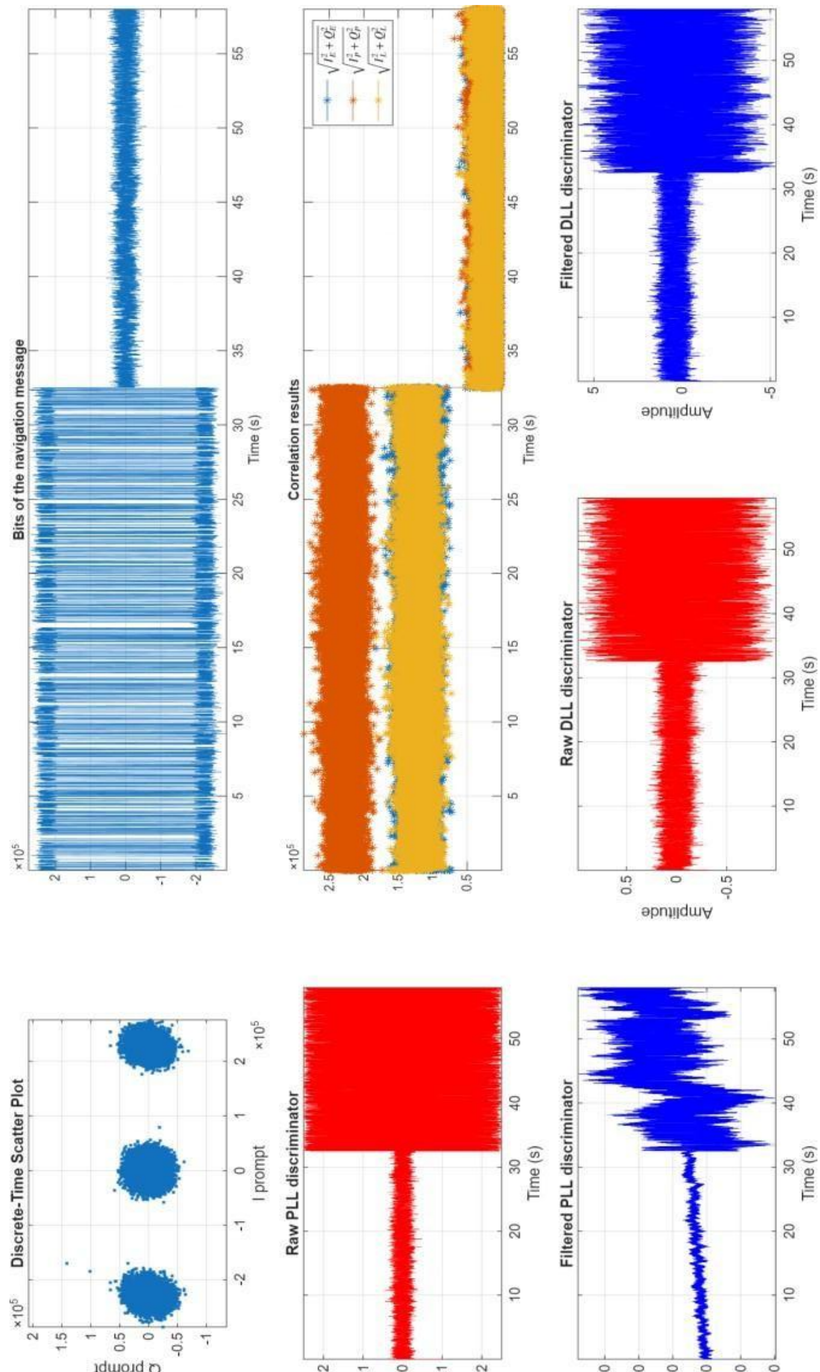


*Figure 3.15 Tracking Loop Outputs for PRN 2*

```
Command Window
                    ------------------------------

Probing data (RawData_Acquisition_D21_07_2025_T_11_30_15_IQ_Int16.dat)...
  Raw IF data plotted
  (run setSettings or change settings in "initSettings.m" to reconfigure)

Enter "1" to initiate GNSS processing or "0" to exit : 1

Starting processing...
   Acquiring satellites...
(01 02 . . . . . . . . . . . . . . 17 . . . . . . . . . . . . . . 32 )

*=========*=====*===============*===========*=============*========*
| Channel | PRN |   Frequency   |  Doppler  | Code Offset | Status |
*=========*=====*===============*===========*=============*========*
|       1 |   2 |  6.33240e+02 |     633    |     2576    |     T  |
|       2 |   1 |  -1.29700e+03 |   -1297   |      3878   |     T  |
|       3 |  32 |  7.32422e+02 |     732    |     5561    |     T  |
|       4 |  17 |  -3.01361e+03 |   -3014   |      3082   |     T  |
|       5 | --- |  ------------ |   -----   |    ------   |   Off  |
|       6 | --- |  ------------ |   -----   |    ------   |   Off  |
|       7 | --- |  ------------ |   -----   |    ------   |   Off  |
|       8 | --- |  ------------ |   -----   |    ------   |   Off  |
*=========*=====*===============*===========*=============*========*

   Tracking started at 21-Jul-2025 11:47:44
   Tracking is over (elapsed time 00:01:50)
   Saving Acq & Tracking results to file "trackingResults.mat"
   Calculating navigation solutions...
   Processing is complete for this data block
   Ploting results...
Post processing of the signal is over.
>>
>> |
```

*Figure 3.16 Command-line log about the status of the software-defined receiver*

Figure 3.16 is a command-line log that provides numerical and status data, confirming the successful execution of each stage of the receiver's operation. The channel column indicates the receiver's internal channel number and the corresponding PRN number for any detected satellites. It also gives an estimated frequency shift for each acquired signal.

Following this, the tracking started successfully, indicating that the acquisition phase is complete. It starts to fine-tune its synchronisation with the acquired satellite signal. The results of these stages generate plots of correlation results and PLL/DLL discriminators.

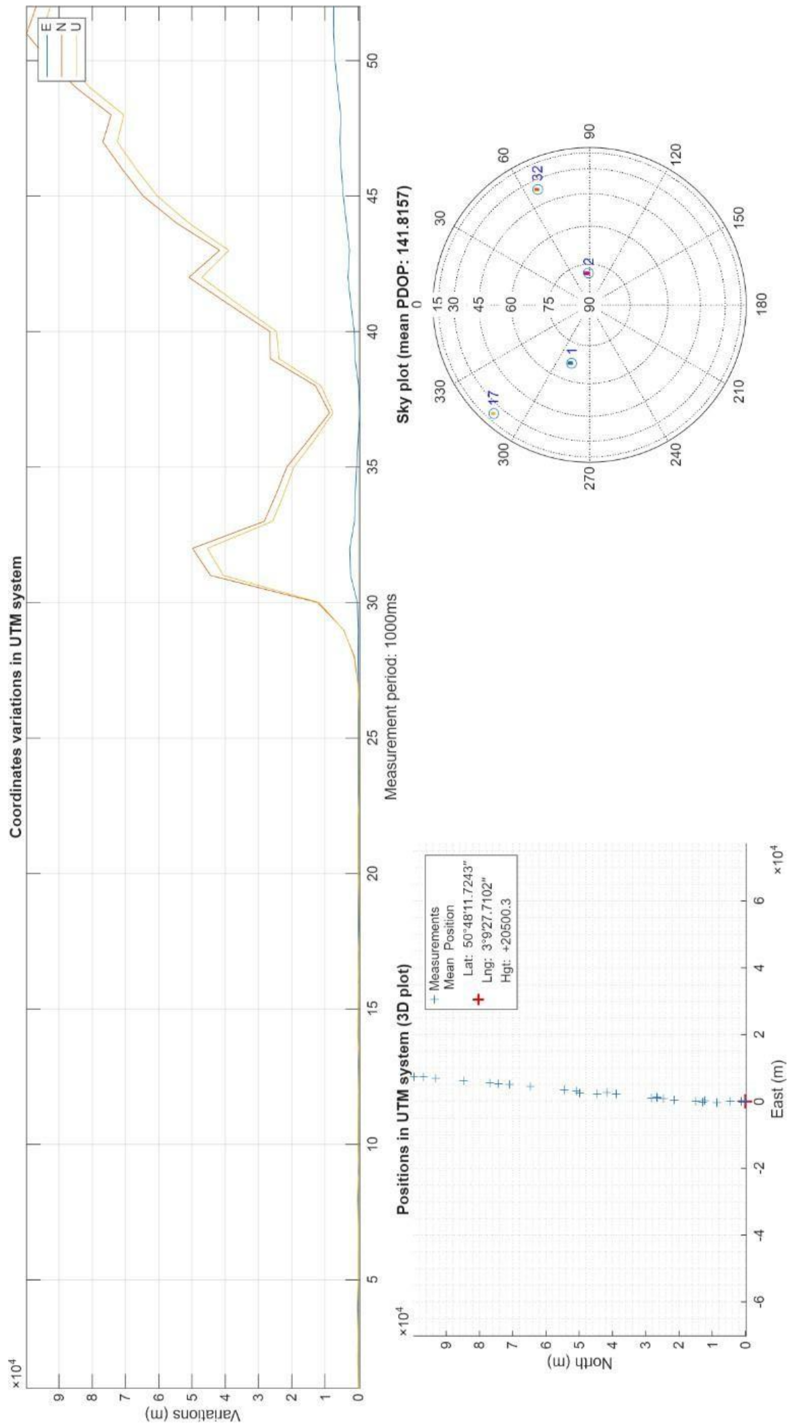


*Figure 3.17 Output plot of Navigation Processing*

Later, it starts computing and evaluating the navigation solutions (Figure 3.17), the final step of the post-processing algorithm. The receiver uses the pseudo range measurements from the tracking phase to solve for its Position, Velocity, and Time. This gives the final plot of the process, including the UTM position variations (expressed in meters as Easting-Northing values) and PDOP values. The sudden jump in position variations indicates a loss of signal for the tracked satellite (PRN 2). The sky plot is a visual representation of the spatial distribution of the visible satellites from the receiver's perspective.

The receiver next estimates the velocity components and the speed. Although position estimates are strongly influenced by variations in satellite-receiver geometry, velocity, particularly when derived from Doppler frequency shifts, is less sensitive to satellite geometry. But Doppler observation provides a linear constraint on the velocity vector, so Doppler measurements are not completely independent of geometry. The sensitivity matrix still depends on the LOS directions of all the available satellites. When PDOP becomes high, typically due to poor satellite distribution, the LOS vector becomes more aligned, reducing the geometric strength and leading to erratic velocity values (Refer to Figure 3.18). Even though the test was performed at the stationary position, the receiver velocity shows the highest values ($Vx$ = -4000 m/s; $Vy$ = -10000 m/s; $Vz$ = 0 m/s), which are due to a PDOP of around 141.8157.

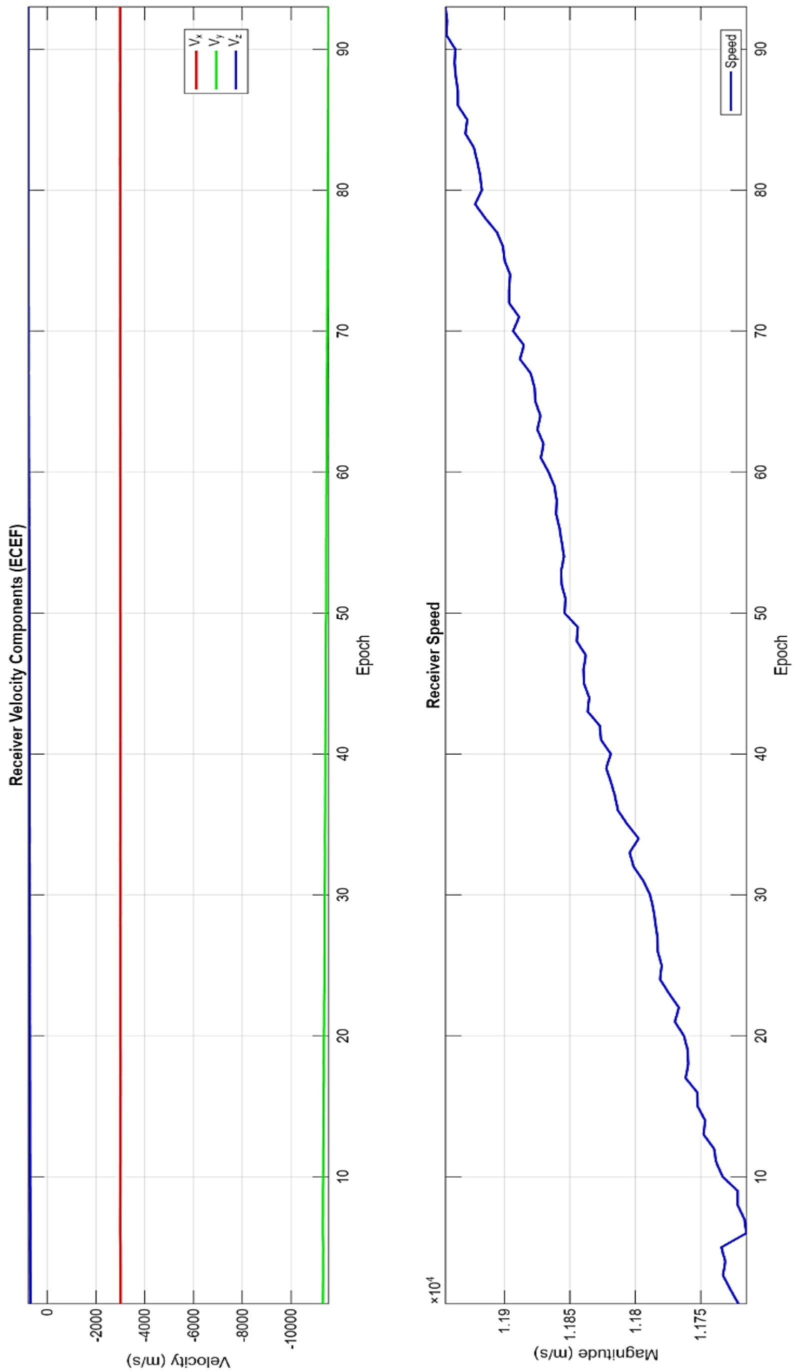


*Figure 3.18 Receiver velocity and receiver speed in the ECEF coordinate frame*

To recover the usable velocity estimate from this geometrically compromised data, one must abandon the requirement for an unbiased estimator in favour of a stable one. To address this, a Tikhonov regularisation term was introduced to stabilise the solution when the satellite geometry degrades. These regularisation techniques are well established in GNSS processing, particularly when the design matrix becomes ill-posed or satellite visibility is reduced. They help estimate parameters by amplifying noise.

It is an introduction of the regularisation term that imposes the a priori knowledge about the properties of the solution, specifically that the velocity of a physical receiver should be bounded and smooth, not erratic.

The standard LSE minimises the norm of the residuals:

$$\| H_v x - y \|^2 \tag{3.25}$$

But the Tikhonov regularisation adds a penalty term to the solution norm.

$$\| H_v x - y \|^2 + \alpha \, ||\Gamma x||^2 \tag{3.26}$$

where,

$\alpha$ Is the regularisation parameter.

$\Gamma$ is known as the Tikhonov matrix (Identity matrix)

So, the solution for the user velocity vector (2) becomes,

$$x_{Tikhonov} = (H_v{}^T * H_v + \alpha I)^{\wedge -1} H_v{}^T * y \tag{3.27}$$

By adding the $\alpha I$ To the LSE solution, the receiver can artificially inflate the diagonal elements. This transforms the nearly singular matrix into an invertible matrix. Although these terms introduce a small amount of bias into the results, they significantly reduce the variance in velocity estimates.

In this case, the regularised solution settled quickly, the velocity components returned to expected behaviour, with a velocity of 0 m/s, as expected for the receiver under stationary conditions, and the velocity solution was successfully stabilised. The results plot (Figure 3.19) shows consistent ECEF velocity components and a coherent speed magnitude, confirming that the regularisation strategy effectively mitigated the impact of high PDOP value. Instead of jumping by thousands of metres per second due to poor satellite geometry, the penalty term we introduced has constrained the solution to smooth, near-accurate values. Hence, the Tikhonov regularisation has successfully managed the ill-conditioned design matrix caused by poor PDOPs.

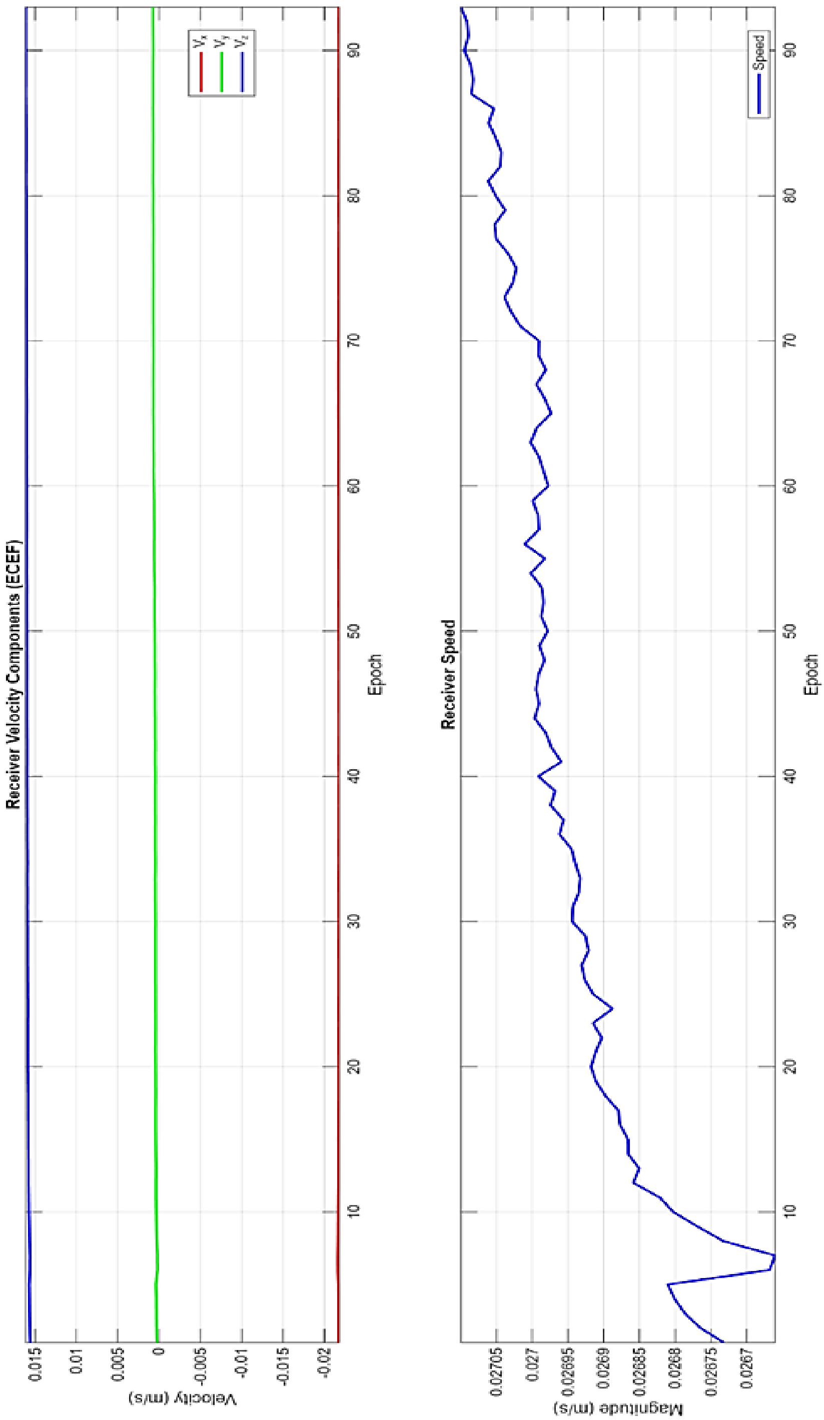


*Figure 3.19 Receiver velocity and speed after Tikhonov regularisation*

## CONCLUSION

The work in this chapter demonstrates how valuable a controlled SDR-based test can be for understanding GNSS-based speedometers. By recoding raw I/Q data and processing it in software, it was possible to observe the receiver's internal behaviour in ways a commercial receiver cannot. This helps reveal how Doppler-derived velocity performs under both ideal and challenging conditions. The temporary loss of PRN 2 and the high PDOP clearly showed that Doppler measurements can become unstable even when satellite geometry degrades. Introducing a regularisation term stabilised the solution and produced the expected velocity for a stationary condition. These findings highlight the importance of regularisation techniques when GNSS data is used in real mobility applications. Because improving the reliability of GNSS- and derived-speed data supports a wide range of sustainable mobility goals, from traffic monitoring to eco-driving to protecting VRUs. Strengthening the accuracy of these measurements can contribute to smarter, safer, and more sustainable transport systems.

# *CHAPTER 4*

# *EXPERIMENTAL CHARACTERISATION OF PEDESTRIAN VELOCITY USING GNSS RECEIVERS*

## 4.1 INTRODUCTION

The primary goal of smart mobility infrastructure is to safeguard vulnerable road users. Pedestrians are the most at risk in road accidents, particularly at intersections. In the UK, the Department for Transport reported, between the years 2004 and 2021, an average of 8 pedestrian deaths and 115 severe injuries per week in traffic crashes. Furthermore, 30% of deaths happen at a point of intersection.

This chapter aims to describe a contribution to the development of a sustainable, innovative mobility system that detects pedestrians at traffic junctions and signals alerts to an intelligent traffic system [123] developed during my PhD One of the many challenges the government faces is providing high-quality, environmentally friendly, and sustainable services to its residents. However, as saviours, intelligent solutions driven by advancements in Internet and Communication Technology (ICT) have transformed traditional cities into smart cities, thereby initiating the development of smart cities worldwide [124].

A smart city is an urban area that uses technologies such as the Internet of Things (IoT), sensors, and other digital solutions to manage resources and services without requiring extensive effort [125]. Several definitions of smart cities exist in the literature [125].

The idea of smart cities includes six essential components:

a) smart economy

b)smart governance

c) smart living

d) smart people

e) smart environment

f) smart mobility

Smart mobility encompasses smart streets, parking, pedestrian management, efficient transportation services, traffic management, and navigation systems [124], [125]. Pedestrian management involves reducing VRU-related accidents and ensuring smooth, seamless road crossings. The concept is to adjust the traffic signal based on the time of day and the number of pedestrians waiting to cross the road, thereby improving pedestrian traffic flow [124], [126]. So, this involves real-time monitoring of pedestrian velocity. This intelligent traffic control and management system optimises traffic flow and travel speed while ensuring the safety of pedestrians and other road users by monitoring smart vehicles, intelligent traffic systems, and smart incident management systems. The Smart Traffic Signal Control System (STSCS) employs Artificial Intelligence (AI) to adjust traffic signal timings based on current traffic conditions at intersections, promoting safe, smooth traffic flow [127]. This approach also helps decrease congestion and lower carbon emissions during vehicle stops.

This chapter examines the theoretical foundations, the implementation of a chosen specific algorithm, the experimental characterisation of a GNSS receiver embedded in smartphones, and the velocity estimation method for a pedestrian use case.

## 4.2 ROLE OF GNSS IN MEASURING THE VELOCITY OF THE PEDESTRIANS

Innovations and advancements in satellite-based positioning enable safer, more efficient transportation services and applications. GNSS systems play an essential role in the design of new Intelligent Transport Systems (ITS) infrastructure, due to their flexibility, rapid growth, low infrastructure costs, and long-term durability and sustainability [128]. Traffic signals change their lights according to set rules or timing. Some systems include a button that can trigger a traffic light change after a specific period since it was pressed. While this system is easy to install, it might not be accessible to people with disabilities.

The existing literature offers several ideas to address this issue and proposes solutions. One example is a proposal to automate traffic signal operations by detecting individuals who are crossing the road using video cameras [129]-[132]. Setting up video cameras at every traffic intersection isn't feasible because they are expensive and pose installation and setup challenges. Additionally, video quality, lighting conditions, and the cleanliness of the camera optics might affect the system's reliability.

In recent years, thanks to the improvements in communication technology and electronics, we have witnessed the broad adoption of smartphones. These handheld devices are equipped with a multiconstellation GNSS receiver that provides raw GNSS measurements for processing to obtain high-precision data [133],[134]. This enables the development of applications that do not need to rely on roadside infrastructure, such as video cameras, but instead run on smart devices, reducing costs and increasing scalability.

*The research aims to propose an application that can alert an intelligent traffic light indicating that a pedestrian is waiting to cross the road. This software continuously tracks the positions and velocities of pedestrians. So,* *when a pedestrian approaches an intersection, the smart traffic light communicates with it. If the pedestrian's velocity is zero, it indicates the pedestrian is waiting to cross the road, and the traffic light changes accordingly.*

Hence, accurate velocity measurement is crucial for this purpose. Several articles have analysed the performance of GNSS receivers embedded in smartphones to determine the user's PNT. It is essential to understand the operating principles of GNSS receivers for velocity estimation, the types available, and the best methods to apply for this work.

## 4.3 TDCP OBSERVABLE AND ITS MODEL

### 4.3.1 Carrier Phase observation model

The raw carrier-phase measurement for the single signal from satellite *s* the receiver *u* at epoch *t* is modelled as:

$$\varphi_u^s(t) = \frac{1}{\lambda}\left(\rho_u^s(t) + c(\delta t_u(t) - \delta t_s(t)) + T_u^s(t) + I_u^s(t)\right) + N + \epsilon_\eta(t) \quad (4.1)$$

where,

$\lambda$ is the carrier wavelength of the GNSS signal

$\rho_u^s(t)$ is the geometric range of the satellite receiver

$c$ is the speed of the light

$\delta t_u$ is the receiver clock error

$\delta t_s$ is the satellite clock error

$T_u^s$ refers to the tropospheric error

$I_u^s$ is the Ionospheric error

*N* is an integer ambiguity

$\epsilon_\eta$ measurement noise

### 4.3.2 Time Differencing Carrier Phase model

TDCP from [136] is formed by differencing two carriers at two epochs for the same satellite. and is represented by

$$\Delta\varphi_u^s = \varphi_u^s(t_2) - \varphi_u^s(t_1) \tag{4.2}$$

Assuming that there are no cycle slips and integer ambiguity $N_u^s$ is constant, and atmospheric delays and satellite clock are slowly varying in time, so they are negligible. Hence, the dominant term is the geometric range, which depends on the user's velocity as the position changes. Substituting 4.1 in 4.2, we get

$$\Delta\varphi_u^s = \frac{1}{\lambda}(\Delta\rho_u^s + c\Delta\delta t_u) + \Delta\epsilon_\eta \tag{4.3}$$

where,

$$\Delta\rho_u^s = (\rho_u^s(t_2) - \rho_u^s(t_1)) \tag{4.4}$$

$$\Delta\delta t_u = (\delta t_u(t_2) - \delta t_u(t_1)) \tag{4.5}$$

Multiplying the wavelength with the carrier phase,

$$\lambda\Delta\varphi_u^s = (\Delta\rho_u^s + c\Delta\delta t_u) + \Delta\epsilon_\eta \tag{4.6}$$

The geometric change also involves a change in the LOS direction from satellite to receiver. Even if the receiver is stationary, the satellite orbits the Earth at 3.9 km/s, which causes a rotation in the Line-of-Sight vectors, so the geometric change must include this term. $\Delta g$. Without this, the TDCP would misinterpret the LOS rotation as a receiver motion. So, $\Delta \rho$ has two components, $\Delta g$ and $\Delta D$. Rewriting equation 4.6 according to this, it becomes

$$\lambda \Delta \varphi_u^s = (\Delta \mathrm{D} - \Delta g + c\Delta \delta t_u) + \Delta \epsilon_\eta \tag{4.7}$$

The term $\Delta g$ represents a term that considers the variation of receiver-satellite geometry and $\Delta D$ is the variation in the distance between the receiver and the satellite, proportional to the average Doppler frequency shift due to their relative motion.

TDCP tries to estimate the receiver displacement vector $-a_x \Delta r_{ux} - a_y \Delta r_{uy} - a_z \Delta r_{uz}$., where $a_x$, $a_y$ and $a_z$ are the direction cosines of the receiver-satellite of two consecutive epochs, and $\Delta r_{ux}$, $\Delta r_{uy}$ and $\Delta r_{uz}$ These are the components of the receiver displacement between the epochs. The TDCP correct this rotation issue with the term $\Delta g$. The final TDCP equation is written as,

$$\lambda \Delta \varphi_u^s - \Delta D + \Delta g = -a_x \Delta r_{ux} - a_y \Delta r_{uy} - a_z \Delta r_{uz} + c\Delta \delta t_u + \Delta \epsilon_\eta \tag{4.8}$$

The unknowns of the TDCP are $\Delta r_{ux}$, $\Delta r_{uy}$ and $\Delta r_{uz}$ and the coefficients of the unknown are given as :

$$a_x = -\frac{x_s - x_u}{d} \qquad a_y = -\frac{y_s - y_u}{d} \qquad a_z = -\frac{z_s - z_u}{d} \tag{4.9}$$

where $x_s, y_s$ and $z_s$ are satellite coordinates and $x_u, y_u$ and $z_u$ are receiver coordinates.

The unknowns of the TDCP equations are four 3D receiver coordinates and a receiver clock bias. So, we need at least four equations like 4.8 to solve the receiver unknowns. The least squares estimation method can be applied when the measurements are redundant. The measurements are weighed according to the satellite elevation, and the weight associated with the i-th measurement is

$$w_i = \frac{sin^2(El_i)}{(\sigma_0)^2} \tag{4.10}$$

where $El_i$ is the elevation of the i-th satellite and $\sigma_0$ is a constant. The components of the receiver velocity are obtained by

$$[v_{ux}, v_{uy}, v_{uz}] = \left[\frac{\Delta r_{ux}}{\Delta t}, \frac{\Delta r_{uy}}{\Delta t}, \frac{\Delta r_{uz}}{\Delta t}\right] \tag{4.11}$$

where $\Delta t$ is the time interval between the two consecutive epochs.

Low error levels are a fundamental feature of the TDCP approach. It can provide velocity with an accuracy of a few mm/s when using high-quality receivers under open-sky conditions. Cycle slip can alter *N* and cause inaccuracies in the TDCP measurement. The RAIM algorithm implemented in this work can recognise and reject minor errors. Additionally, the GNSS receivers used in this test are low-quality chips embedded in smart devices, known for their noisy readings and high likelihood of cycle slip [123]. Therefore, RAIM is essential, and a brief introduction to this algorithm is provided in the following section.

## 4.4 RECEIVER AUTONOMOUS INTEGRITY MONITORING *(RAIM)*

It is essential for real-time GNSS-based navigation to assess the quality and safety of the system, which is commonly referred to as "integrity." RAIM has been developed to provide integrity services for civil aviation, issuing warnings when one or more systems are untrusted for navigation [137]. Beyond its application in aviation, RAIM has evolved into a general-purpose integrity measure for GNSS receivers, especially in contexts where measurement errors, such as multipath, satellite anomalies, or cycle slips, may compromise the accuracy and reliability of navigation solutions. Literature describes RAIM as a collection of statistical consistency-checking methods that operate directly on redundant satellite measurements to determine whether the observation set is self-consistent under the assumed noise model.

### 4.4.1 Principles of Fault Detection

RAIM detects faults using the least-squares residuals or the party space representation. After calculating a navigation solution, the receiver creates a residual vector from the observed and expected values. Under nominal conditions, these residuals have a known distribution specified by the measurement covariance. To identify the inconsistencies in a measurement set, a test statistic, usually a quadratic form of residuals, is compared to a threshold based on a chi-square distribution.

The ICAO's integrity guidance emphasises that at least five satellites are required for fault detection, since one redundant measurement is needed to perform the statistical test. Modern multi-constellation smartphone receivers typically have this redundancy.

### 4.4.2 Fault Detection and Exclusion

When at least six satellites are available, RAIM may conduct fault detection and exclusion (FDE). In this mode, the receiver methodically checks subsets of the measurement set to determine which observation is most likely the source of the discrepancy. The inaccurate measurement is then eliminated, and the navigation solution is recalculated using the remaining data.

According to the ICAO guidelines, this technique is crucial for ensuring the continuity during the single-.measurement problems, especially for users who expect uninterrupted service. A recent study suggests that FDE is particularly useful in multi-constellation systems, because the number of visible satellites increases the likelihood of isolating a wrong measurement without affecting the solution geometry.

## 4.5 MEASUREMENT SETUP

The experimental evaluation involves two commercially available smartphones, selected to represent contrasting levels of GNSS receiver capabilities embedded in smartphone and tablet devices. It uses TDCP-based velocity estimation under stationary conditions in urban environments. To determine how dependent the TDCP method's performance is on specific hardware platforms, parallel experiments have been conducted using two selected devices under the same urban conditions.

### 4.5.1 Device Specifications

The first device, "***Device 1***", is a *Samsung Galaxy Tab S6 Lite tablet* running on Android 13 OS and equipped with a Broadcom BCM47531 GNSS receiver chipset. This receiver supports signal reception from multiple satellite constellations, including GPS, BDS, GLONASS, QZSS and the Satellite-Based Augmentation System (SBAS) [138]. Multi-constellation reception increases the number of simultaneously visible satellites, improving geometric diversity and strengthening RAIM fault-detection capability [139].

The second device, "***Device 2***," is a *Xiaomi Mi 8 smartphone* running Android 10 with a Broadcom GNSS receiver chipset, model BCM47755. This chipset supports dual-frequency bands, including both the legacy L1 signal and the modern L5 signal. This makes Device 2 the first mass-market smartphone with a dual-frequency GNSS receiver. It is important to note that this chipset has an integrated sensor hub. Measurements from other sensors, such as accelerometers, gyroscopes, magnetometers, and others, are fused with GNSS measurements to provide highly accurate output [140]. The supporting constellations are GPS (L1 and L5), GLONASS (L1), BDS (B1), QZSS (L1 and L5), and Galileo (E1 and E5a).

The dual-frequency reception option significantly improves location and velocity accuracy in challenging conditions by enabling the creation of Ionosphere-free linear combinations that effectively eliminate first-order ionospheric delays [134].

### 4.5.2 Test conditions

The tests were carried out at three locations and under three conditions in urban environments in Cassino, Italy, representing a range of sky visibility and environmental complexity typical of different stages in pedestrians' approach to a road crossing. All tests took place on the same day (4 November 2023), ensuring consistency in satellite constellation geometry and atmospheric conditions across the three scenarios.

#### 4.5.2.1 Scenario 1

Scenario 1 was conducted on the rooftop of the School of Engineering building. This elevated, wide area offers an unobstructed sky view, free from building obstructions and significant multipath sources. It was used as a near-ideal reference state against which performance in more challenging environments could be benchmarked. Open-sky conditions for GNSS testing of this kind are widely used as a baseline for characterising receiver noise floors and validating processing algorithms in the existing literature [134], [135].

*Figure 4.1 Testbed at Scenario 1*

*Figure 4.2 Aerial View of Scenario 1*

#### 4.5.2.2 Scenario 2

The pedestrian crossing located on the access road in front of the School of Engineering building was considered as test scenario 2. This location directly mimics the operational use case of this work: pedestrians waiting at the junction and waiting for a green light before crossing the road. The environment is surrounded by buildings and trees, which introduce moderate multipath and partial blockage of satellite visibility, reflecting the conditions that practically deployed systems would regularly encounter in light-to-moderate urban settings (semi-urban areas) [142].

*Figure 4.3 Testbed at scenario 2*

*Figure 4.4 Aerial view of scenario 2*

#### 4.5.2.3 Scenario 3

The urban condition considered for scenario 3 is a signalised multi-lane intersection managed by traffic lights. This site was chosen to represent the most demanding conditions within the intended operational parameters. The proximity of taller buildings, a denser traffic environment, and a greater number of signal reflecting surfaces all contribute to more severe GNSS reception environments, characterised by increased multipath interference and more frequent satellite visibility blockages. This environmental condition has been extensively discussed in the GNSS urban canyon literature [135],[142].

*Figure 4.5 Testbed at scenario 3*


*Figure 4.6 Aerial view of Scenario 3*

## 4.6 DATA ACQUISITION

At each test condition, the chosen devices were placed nearby and operated simultaneously in a stationary configuration throughout the logging period. The purpose of this stationary condition is to simulate a pedestrian waiting at the curb and to evaluate accuracy without needing an independent reference tool, since the ground truth velocity is conceptually zero, and any non-zero velocity values produced by the TDCP estimator indicate the observable error. This approach mirrors the methodology used in a comparable smartphone GNSS performance characterisation study.

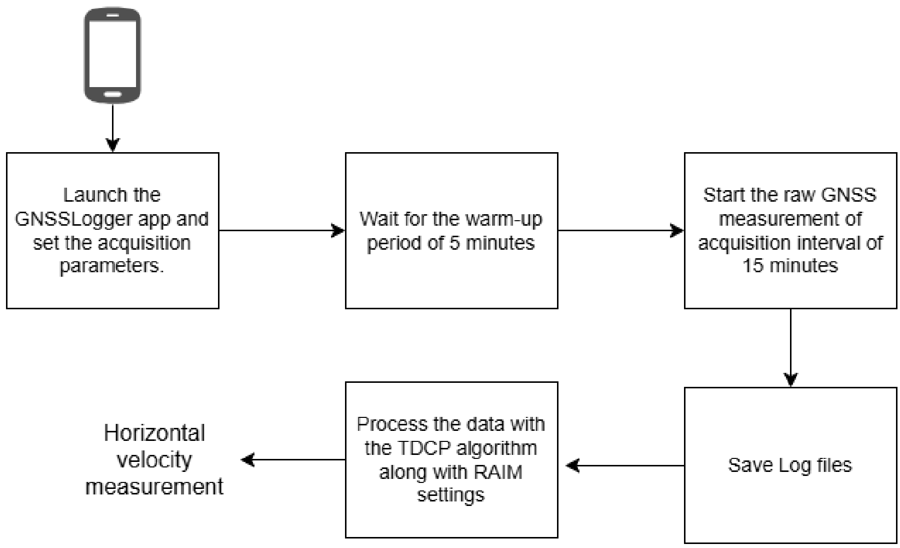


*Figure 4.7 Flowgraph of measurement method*

The measurement process followed a predefined set of instructions for each scenario (Refer to Figure 4.7). Once the device was turned on, GNSSLogger (an Android application) had to be launched with the required settings to enable NMEA, generate an RINEX observation file, log the GNSS receiver location, and record the measurements. A 5-minute warm-up period was then conducted to allow the device to reach its Time-to-First Fix. This warm-up period enables the receiver to download satellite broadcasts, Ephemerides, and Almanack data, complete signal acquisition, and stabilise the tracking loops, all of which are essential for reliable carrier-phase measurements [123]. The data logging period lasted 15 minutes at each test site, capturing data at 1 Hz. After the test, the raw GNSS observation files were stored and transferred for offline processing using the TDCP algorithm implemented in MATLAB. The GUI of the GNSSLogger is provided below:

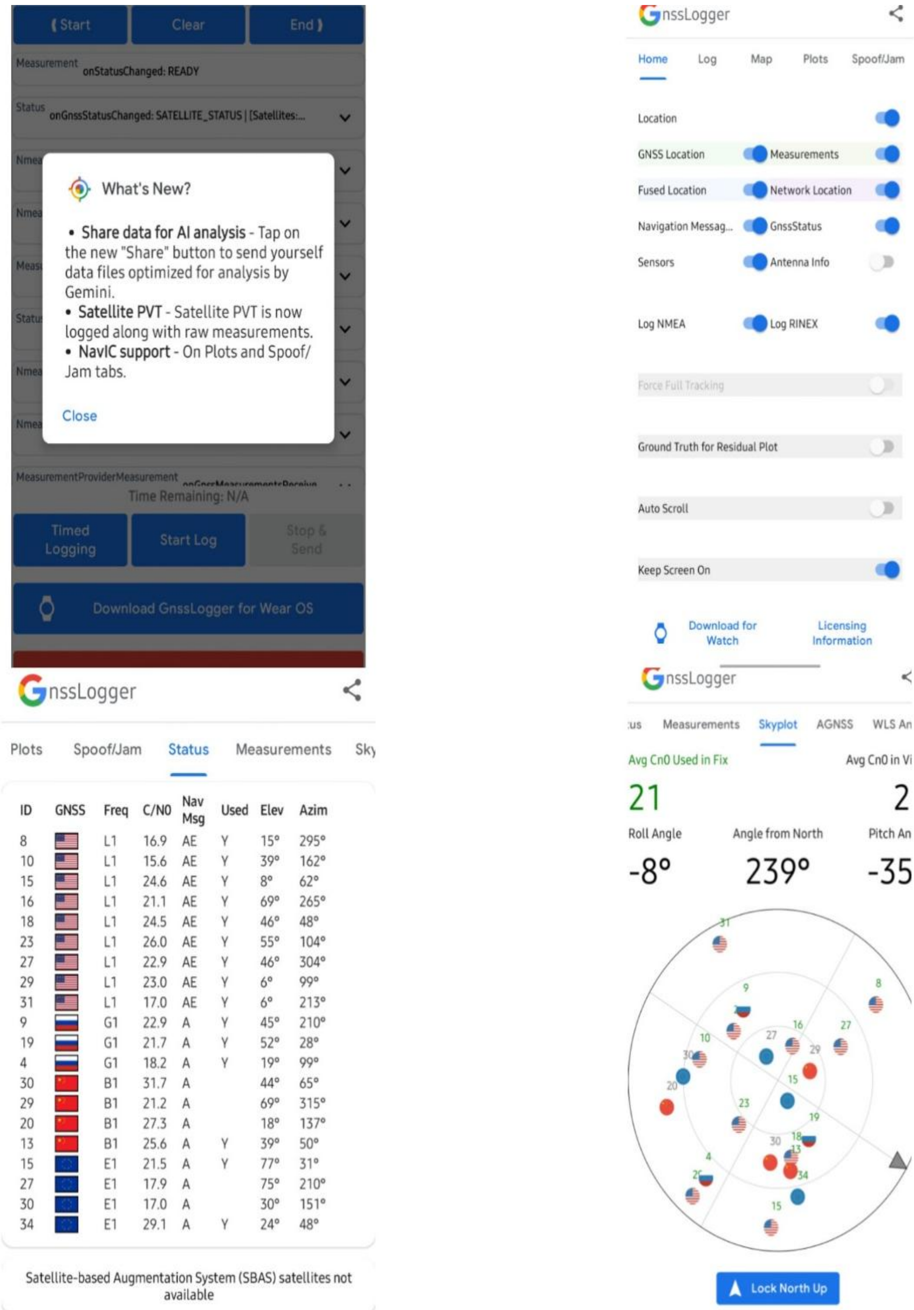


*Figure 4.8 GUI Windows of GNSS Logger*

## 4.7 RESULTS

Since all the data was logged in the stationary mode, the actual horizontal velocity is zero throughout the recording session. The estimated horizontal velocity magnitude at each epoch, therefore, represents the absolute error at that particular epoch. The results are provided in *Table 4.1* for the estimated mean velocity ($\mu$), which captures the systematic bias error of the estimator, the standard deviation ($\sigma$) represents the repeatability as the spread of results around the mean value; MAX represents the maximum observed value, which captures the worst-case error encountered during the session and reflects the tail behaviour of the error distribution. These statistics are summarised to characterise the performance of GNSS receivers using the TDCP approach across each scenario and device. These three quantities, taken together, provide a metrologically meaningful characterisation of the estimator, consistent with measurement and instrumentation norms [141],[143].

| **Test Scenarios** | **Horizontal Velocity [m/s]** | | | | | |
|---|---|---|---|---|---|---|
| | **Device 1** | | | **Device 2** | | |
| | $\mu$ | $\sigma$ | *max* | $\mu$ | $\sigma$ | *max* |
| Scenario 1 | 0.016 | 0.034 | 0.616 | 0.015 | 0.034 | 0.804 |
| Scenario 2 | 0.0112 | 0.0086 | 0.1159 | 0.016 | 0.031 | 0.426 |
| Scenario 3 | 0.018 | 0.023 | 0.238 | 0.017 | 0.029 | 0.589 |

*Table 4.1 Horizontal Velocity obtained from the TDCP estimator*

Another significant metric is the metrological compatibility of these two devices. The results are considered metrologically compatible at a specified coverage probability (68%) because their uncertainty intervals overlap [123]. This measurement compatibility between two distinct devices under identical environmental conditions suggests that the measurement outputs are predominantly influenced by the physical environment rather than device specifications.

### 4.7.1 Horizontal Velocity in Scenario 1

From the results in Table 4.1, for Scenario 1 (open-sky condition), both devices estimated the horizontal velocity magnitudes at 0.016 and 0.015 m/s, respectively. The standard deviation for Device 1 and Device 2 was 0.034, indicating similar measurement variability despite differences in chipset features**.** The maximum error across both devices was below 0.804 m/s, suggesting an isolated spike attributed to a cycle slip that evaded the RAIM_FDE algorithm's exclusion, either due to insufficient redundancy at that epoch or to geometrically challenging fault-detection conditions.

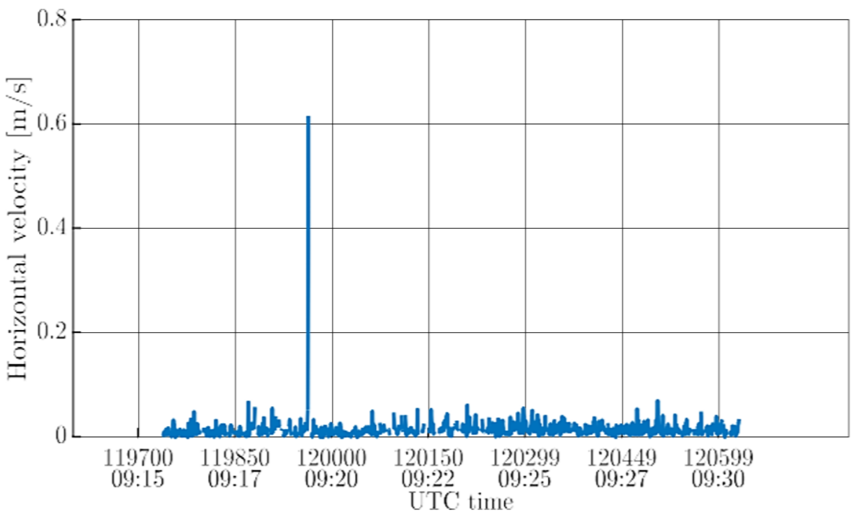


*Figure 4.9 Horizontal Velocity of Device 1*

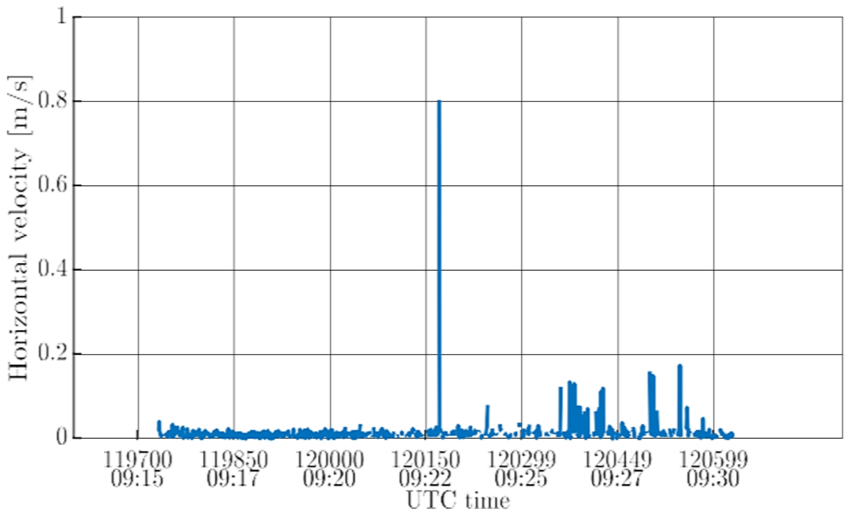


*Figure 4.10 Horizontal Velocity of Device 2*

Given the noticeable difference between the two devices in Scenario 1, the nominal difference in the chipset specifications was somewhat unexpected. The advantage of the dual-frequency setting in Device 2 is negligible under open-sky conditions, which makes the more capable chipset outperform the test. It demonstrates that, rather than multipath and atmospheric error, receiver tracking noise and cycle skips are the dominant errors in the given open-sky scenario.

The metrological compatibility of the two devices was confirmed at a coverage probability of 68%, establishing that the spread of results is consistent across both devices that observe the same quantity (Velocity) with comparable uncertainty. It validates the use of either device as an interchangeable platform for the application under open-sky conditions.

### 4.7.2 Horizontal Velocity in Scenario 2

In this Scenario, which replicates the pedestrian crossing environment, a notable performance difference between the two devices is observed. Device 1 in this scenario provided results that were improved compared to Scenario 1, with the mean falling to approximately 0.011 m/s and the standard deviation to approximately 0.009 m/s, and better repeatability than in the clear-sky condition.

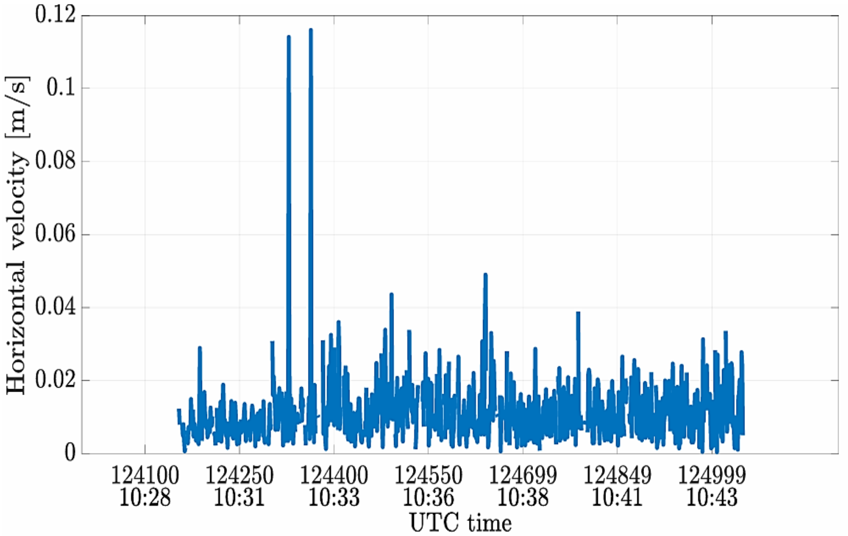


*Figure 4.11 Horizontal Velocity of Device 1*

Device 2 shows the highest maximum error compared to Device 1, with a spike of approximately 0.43 m/s, a mean of 0.016 m/s, and a standard deviation of 0.031 m/s. The spike is consistent with the cycle slip on one or more satellites that the RAIM-FDE algorithm failed to identify, either because the faulty measurement was aligned with the null space of the chi-squared detection test or because the available measurement redundancy was momentarily insufficient for the reliable fault detection and exclusion [144].

But the meteorological compatibility between the two devices was confirmed at a 68% coverage probability.

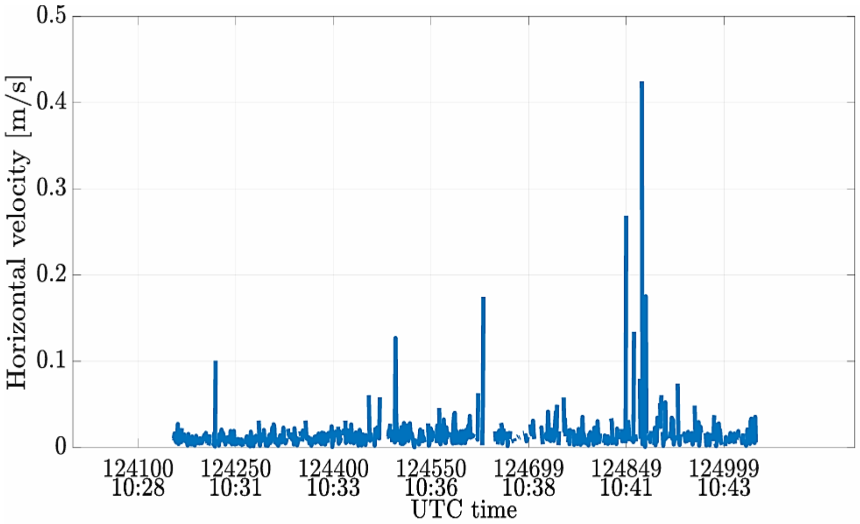


*Figure 4.12 Horizontal Velocity of Device 2*

### 4.7.3 Horizontal Velocity at Scenario 3

This is the most demanding test environment, as it is the traffic-signalised, multi-lane urban core intersection on the road. However, the devices produced results generally consistent with the other two scenarios, which, in itself, supports the feasibility of the intended application. The mean velocities for Device 11 and Device 2 were 0.018 m/s and 0.017 m/s, respectively. The standard deviations for both devices are 0.023 and 0.029, and the maximum errors are 0.238 m/s for Device 1 and 0.589 m/s for Device 2, with a coverage probability of 68%. These results are comparable to Scenario 1 and reflect the greater multipath intensity and more frequent satellite blockages that are common and expected at the urban intersection. In dense urban areas, the satellite signals reflected from buildings arrive at the receiver via multipath with different phase delays. This produces a composite phase observation that is a distorted version of the direct-path signal.

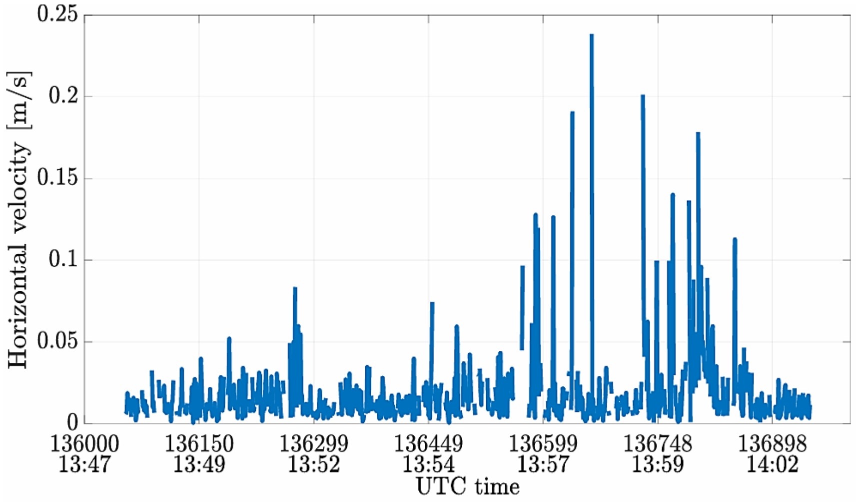


*Figure 4.13 Horizontal velocity of Device 1*

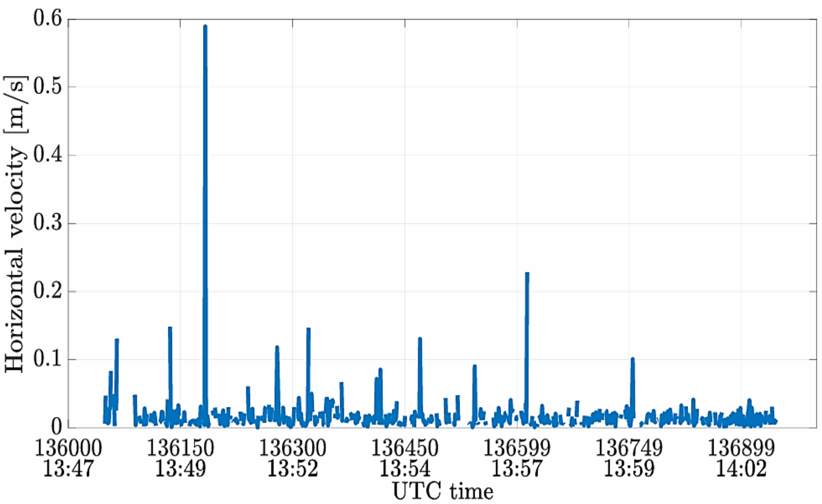


*Figure 4.14 Horizontal Velocity of Device 2*

Across all test Scenarios with the two devices, the best mean estimated velocity is 0.018 m/s, with a standard deviation of 0.034 m/s. This figure shows that the TDCP-RAIM estimator produces a velocity reading that is clustered chiefly around 0 m/s, as expected under stationary conditions [141]. The two devices' metrological compatibility was confirmed at 68% across all three test conditions, demonstrating that the method's performance is largely independent of the devices used with multi-constellation chipsets.

*CHAPTER 5*

# *A WIRELESS SENSOR NETWORK FOR CROWD SENSING: ARCHITECTURE AND EXPERIMENTAL CHARACTERISATION*

## 5.1 INTRODUCTION TO SMART ROAD SENSOR NETWORK

Urban road infrastructure is rapidly evolving to address city mobility needs but faces challenges such as congestion, road wear, air pollution, and climate change. These challenges are well recognised in global urban development reports, which stress the importance of resilient and inclusive transport systems. The UN aims for "access to safe, affordable, accessible, and sustainable transport systems for all" by 2030, as part of SDG 11 - Sustainable Cities and Communities, emphasising equitable mobility as essential for sustainable, liveable cities [145], [146].

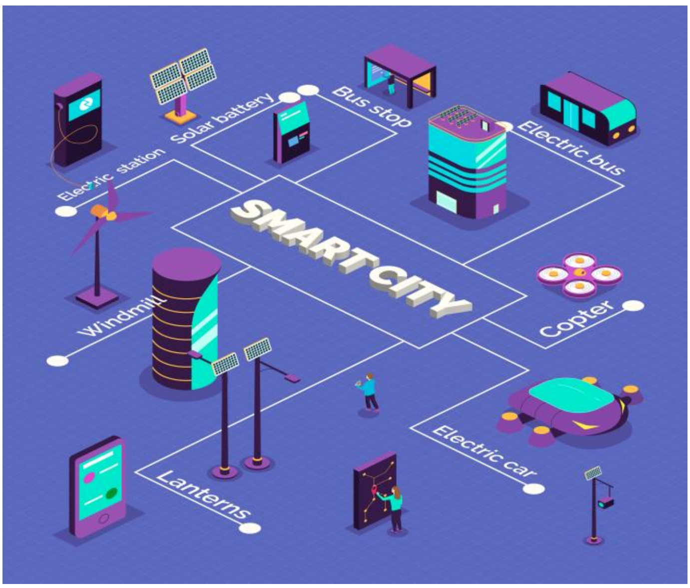


*Figure 5.1 Illustration of smart city eco-system*

Traditionally, asphalt and concrete focus on structural strength, but they are now becoming multifunctional platforms by incorporating sensors for communication, sensing, and energy harvesting [147]. This shift is driven by smaller sensors, wireless technology, and the Internet of Things (IoT), transforming pavements from static structures into active elements of Intelligent Transport Systems (ITS), integrating ICT with IoT [148],[149].

Smart cities provide the broader digital eco-system within which these developments occur. They rely on a group of sensors and actuators embedded across the urban infrastructure to support real-time monitoring, automation, and optimisation of services, including mobility [150].

### 5.1.1 Smart Road and ITS

Digital infrastructure-enhanced roads equipped with sensors, communication modules, and intelligent systems are referred to as Smart Roads. They facilitate real-time traffic monitoring, predictive maintenance, and Vehicle-to-Infrastructure (V2I) communication. Smart roads incorporate embedded sensors, wireless communication technologies, and digital traffic management systems to facilitate autonomous vehicle support, dynamic traffic optimisation, and infrastructure health monitoring [151]. Smart transportation, also known as the Intelligent Transportation System (ITS), refers to the application of ICT, IoT, AI, and Data Analytics to improve the safety, efficiency, and sustainability of mobility systems. These systems rely on a distributed sensor network and real-time data analytics to monitor the traffic conditions, vehicle speeds, and other environmental factors [152].


*Figure 5.2 Overview of integrated innovative technologies*

However, the performance of the ITS depends on the quality, density, and reliability of the underlying sensing infrastructure. This paved the way for intelligent road sensor networks, which serve as the technological foundation for both ITS and smart roads.


*Figure 5.3 Intelligent Transportation System*

### 5.1.2 Smart Road Sensor Networks

Smart Road sensor networks are the fundamental technology layer that enables innovative transport systems and smart roads to operate efficiently. These networks consist of distributed sensing devices such as magnetometers, accelerometers, strain sensors, GNSS-enabled devices, and IoT modules, deployed along roadways to collect traffic, environmental, and structural data [153]. An intelligent transport system is the mobility management of the urban-scale digital ecosystem that smart cities apply. They serve as the critical interface between the physical road infrastructure and the digital mobility management system that characterises modern cities.

Some of the existing innovative road projects are:

*Anas Smart Road (Italy)* – One of the significant initiatives globally covering 2500 kilometres of roads and integrating IoT, AI, big-data platforms and advanced sensor systems [154], [155]. It aims to digitally transform the network of networks for 6700 kilometres of roads by 2032.

*A2 Mediterranean Highway (Italy)* – Part of a broader Italian smart road initiative enables C-ITS (Cooperative Intelligent Transport Systems) for real-time communication between the road and connected vehicles (V2I) [154], [155].

*Cortina Smart Road(Italy)* – A testing ground for innovative mobility models, focusing on real-time data exchange on the SS 51 Alemagna highway to increase safety and sustainability [154].

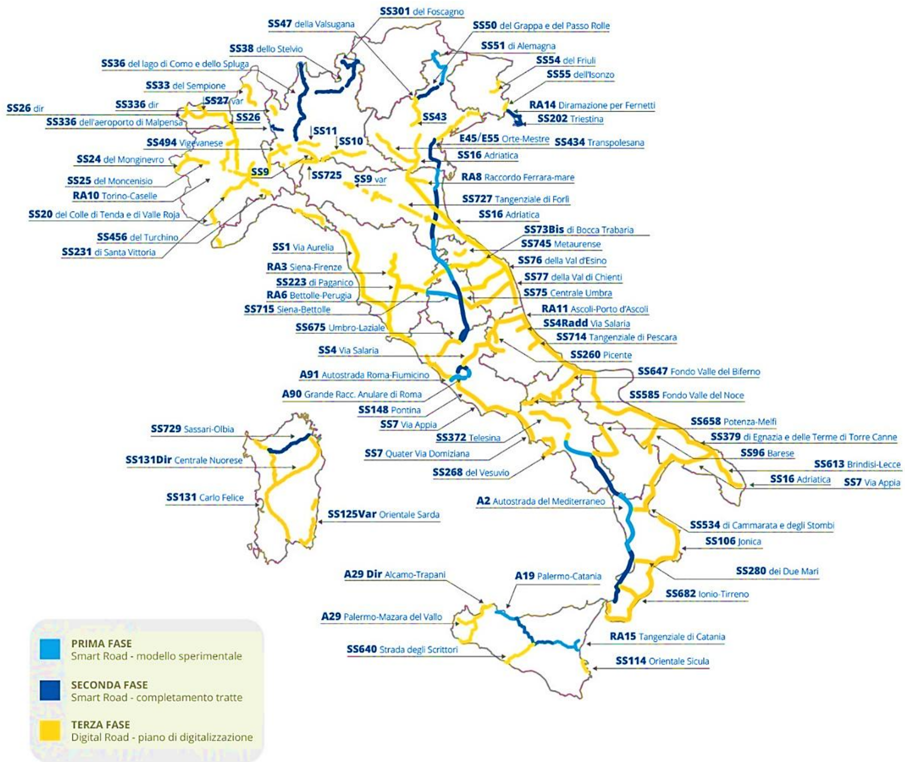


*Figure 5.4 use cases and the Smart Road app adopted from https://www.stradeanas.it/it/smart-road-smart-mobility*

### 5.1.3 Sensing Infrastructure on the Road Surface: Approaches and Limitations

As cities transition to a data-driven transportation system, the road surface becomes a crucial location for sensor equipment. Embedding sensors directly into pavements allows for continuous monitoring of traffic flow, vehicle behaviour, structural health, and environmental variables. This technique is consistent with the trends of "smart pavements", in which the road surface is no longer a passive structural layer but an active component of ITS [153],[156]. Vehicle-based sensing is becoming an acceptable replacement for embedded sensors. Road surface issues significantly affect vehicle performance and safety, resulting in economic losses and traffic delays. Hadj-Attou et al. [157] demonstrate that IoT sensors on vehicles can analyse vibration patterns to assess road conditions, providing an alternative to traditional infrastructure in some cases. Although this method lowers installation costs and avoids disruptive pavement work, it relies on extensive use across vehicles and steady data quality.

***Limitations of the installation of sensing systems on the road surface***

Though pavement-embedded sensors offer significant potential, they face several challenges. Installation and maintenance are key issues because embedding sensors in asphalt or concrete requires invasive construction, which can disrupt traffic and increase costs. Once installed, these sensors withstand harsh mechanical and environmental conditions, including heavy loads, moisture, freeze-thaw cycles in cold climates, and thermal expansion. Consequently, questions about their durability and longevity remain, as repairing or replacing embedded sensors is complicated and risks damaging the pavement structure.

Secondly, issues with data quality and calibration persist as ongoing challenges. The author [158] highlights that sensor drift, noise, and environmental interference can affect measurement accuracy, necessitating robust calibration methods and data-fusion algorithms to maintain reliability over time.

Third, scalability and costs continue to impede wider adoption. Although IoT technology has reduced sensor costs, establishing a large-scale pavement monitoring system still involves significant investments in installation, communication infrastructure, and data management. Incorporating smart-city technology into pavement infrastructure also demands careful coordination with broader urban digital strategies to ensure cost-effectiveness and compatibility [159]. Lastly, durability and lifecycle alignment pose structural challenges, as pavements are often resurfaced and rehabilitated periodically, which can damage or destroy embedded sensors. This mismatch between pavement repair cycles and sensor lifespans complicates long-term planning and increases costs. As a result, many cities and road agencies remain cautious about the large-scale deployment of embedded systems despite their technical advantages.

### 5.1.4 Heritage Constraints

Many European cities, especially historical centres in Italy, feature cobblestone streets, creating culturally and architecturally sensitive surroundings. These historical environments impose strict limitations on any form of physical intervention, including the installation of sensing hardware. While the existing literature on smart pavements focuses mainly on technical performance, it highlights the importance of minimising physical intrusion when installing sensor devices in built environments [160].

Non-invasive or minimally intrusive methods, such as surface-mounted devices, roadside units, or vehicle-based sensing, are becoming more common in IoT-based road monitoring systems because they rarely require structural changes to pavements and surrounding infrastructure [158]. In historical areas, where excavation, drilling, or any alteration of pavement is restricted, such non-intrusive sensing methods become essential [161]. Cities want to improve mobility, but they cannot disturb the historical centres they are trying to preserve.

Another challenge is that the hardware must naturally blend into the environment. Large roadside cabinets, poles, and solar panels are rejected because they disrupt the space's continuity [162], [163]. This makes the solution ultra-compact, low-profile devices or sensing methods that don't require pavement for installation [164]. Wired monitoring systems are sometimes impractical in heritage structures because installation requires invasive cabling and includes visible components that violate heritage conservation guidelines. As a result, the practical use of smart sensing in historical areas, such as old pavements and cobblestone streets, relies heavily on wireless communication technologies that require minimal supporting infrastructure and can operate for extended periods without maintenance [165]. Hence, long-life, low-power wireless nodes are required, and do not need repeated access to sensitive areas.

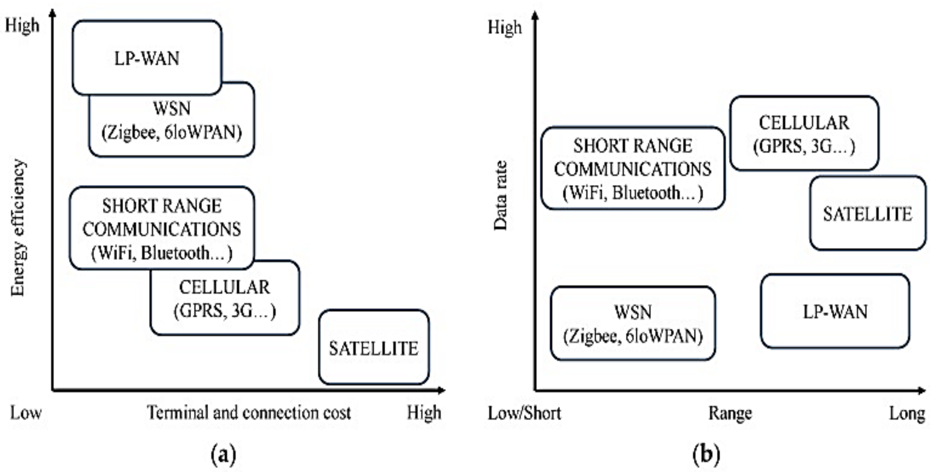


*Figure 5.5 Principal Characteristics of enabling IoT technologies*

*(a) Energy efficiency and cost;(b) Data rate and coverage range*

## 5.2 A WIRELESS SENSOR NETWORK FOR SMART ROAD AND SMART MOBILITY APPLICATIONS

In this framework, to overcome the above-reported critical limitations, the University of Cassino and Southern Lazio, which is involved in the National

Centre for the Sustainable Mobility (MOST), aims to develop an intelligent and distributed IoT sensor network that can be installed on road pavements of historic city centres for smart road and smart mobility applications.

### 5.2.1 Wireless Sensor Network Architecture

The architecture of the proposed IoT sensor network follows a two-tier star topology, consisting of

a) ***Sensor node*** - placed within a cobblestone-like enclosure that is responsible for measuring the environmental parameters at the road/sidewalk surface and transmitting the sensed data to the gateway wirelessly.

b) ***Central gateway*** that collects and forwards data to the higher-level traffic management infrastructure (e.g., ITS) for processing (refer to Figure 5.6).


*Figure 5.6 Proposed sensor network architecture*

The architecture is simple because there is no need for mesh networking or complex protocols, which reduces the computational burden on individual nodes, keeping power consumption low and making the network easy to scale if an extra sensor node is required. This was designed with five core objectives: low power consumption; scalability; reliability; compatibility with energy harvesting and low-power wireless connectivity [166].

### 5.2.2 IoT sensor node

A central feature of this work is the design of the sensor node enclosure, which can naturally blend into the environment using cobblestone or stone blocks. The enclosure (refer to Figure 5.7) was designed using a 3 cm-thick ceramic tile, which closely matches the texture and appearance of cobblestones commonly used in traditional European roads.

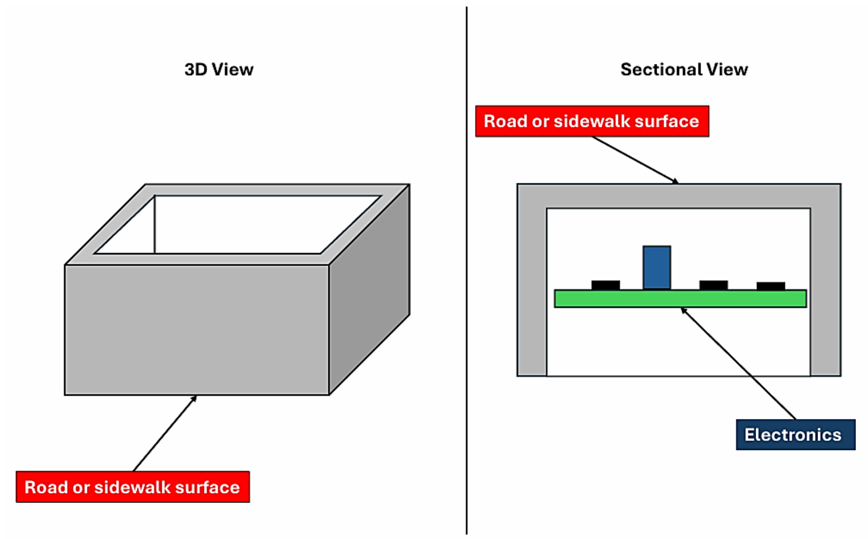


*Figure 5.7 3D and sectional view of the IoT sensor node*

These tiles were assembled to form a cuboid with dimensions (L x W x H) of 27 cm x 17 cm x 9.6cm [166]. The dimensions were chosen to match the typical proportions of the large cobblestones found in Italian city centres. It can easily host sensors and the most common microcontroller platforms, such as the ARDUINO UNO or those based on the ESP32 microcontroller, which typically have a transceiver and an integrated antenna that operate in the ISM 2.4 GHz band.

## 5.3 MEASUREMENT SETUP

To assess the feasibility of using communication standards operating in the ISM 2.4 GHz band for the development of this network and to evaluate the influence of the ceramic cobblestone on communication reliability, the University of Cassino and Southern Lazio conducted preliminary tests in its semi-anechoic chamber.

The semi-anechoic chamber attenuates external electromagnetic interference and multipath reflections, ensuring that any observable changes in the received signal power or packet loss can be attributed exclusively to the presence or absence of the cobblestone enclosure, rather than to environmental noise or fading. This helps in understanding the cause-and-effect conclusions to be drawn from the obtained results.

In particular, the study was based on the adoption of Bluetooth Low Energy (BLE) as a communication standard. It was chosen because BLE devices can operate for months or even years on a small battery. It has been designed for short, quick data exchanges that help conserve power by adopting short-burst communication techniques. Furthermore, BLE operates in the same 2.4 GHz ISM band as classic Bluetooth, enabling dual-mode devices to support both. It is commonly used in trackers and other IoT devices.

To this end, the sensor node placed inside the cobblestone was based on an ESP-32 microcontroller board with an embedded BLE transceiver and antenna. It was chosen for its widespread adoption and ease of programming. It was connected to a Bosch Sensortec BME280 [167] sensor, which measures temperature and relative humidity. Communication between the sensor and the microcontroller is established via the I2C bus. The entire sensor node was powered by a 5000 mAh lithium-polymer battery [166].

As the gateway, it was emulated using a LilyGo TTGO development board based on an ESP-32 and, as in this case, powered by a 5000 mAh lithium-polymer battery.

Two separate test configurations were designed for the feasibility study: one to assess the influence of the cobblestone on the received signal power, and the other to assess end-to-end link quality.

### 5.3.1 Testbed A: Influence of receiver signal power

The first test configuration shown in Figures 5.8 and 5.9 was designed to measure the effect of the ceramic enclosure on signal power at the receiving end. To eliminate the possibility of the gateway's own transmissions from interfering with the power measurements, the gateway was excluded from this setup. Instead of a gateway, a receiving antenna was placed 3 metres from the sensor node (Unit Under Test) and controlled by a calibrated Tektronix RSA306B Real-Time Spectrum Analyser in the room near the anechoic chamber. The UUT was mounted on a wooden turntable at a height of 90 cm.

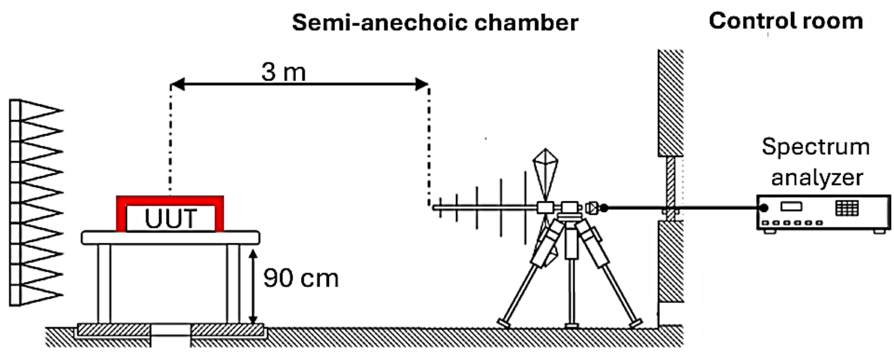


*Figure 5.8 Sensor node embedded in the cobblestone enclosure (Testbed A)*

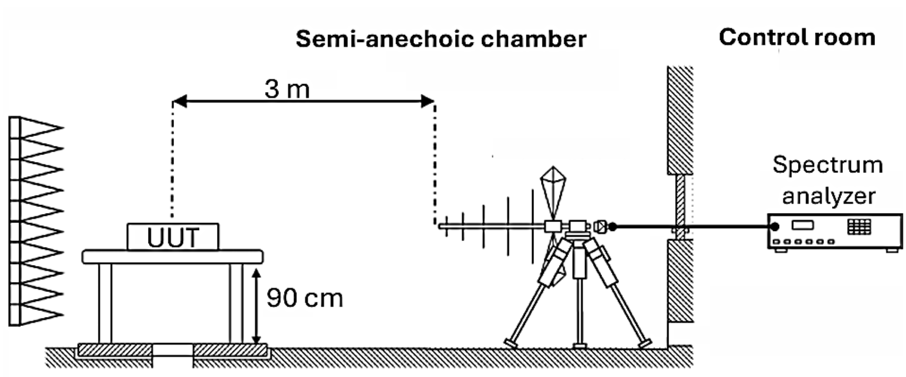


*Figure 5.9 Sensor node without the cobblestone enclosure (Testbed A)*

The directional nature of the antenna's radiation pattern was also taken into account, and to simulate a variety of orientations that a real deployed node might have relative to a street-mounted gateway, the turntable was rotated through four angular orientations: 0°, 90°, 180°, and 270°. Since the antenna's polarisation is also known to affect the received power, all the polarisation angle conditions were tested with the receiving antenna in both horizontal and vertical polarisation orientation, yielding a total of eight unique angle-polarisation combinations.

With each angle-polarisation combination, three measurements were taken. The first and third measurements were taken without the cobblestone enclosure, and the second measurement was taken with the sensor embedded inside it. By comparing the first and third measurement results, it is possible to conclude that the drop in the battery level between the tests has not altered the transmitter's output power. Each measurement lasted 5 minutes, and the spectrum analyser was set to Max Hold mode to capture the signal’s maximum peak level [166].

### 5.3.2 Testbed B: Influence of communication link quality

The second test configuration in Figures 5.10 and 5.11 included the entire system, including the actual gateway. This test bed allowed end-to-end link quality to be characterised under conditions that more closely resemble real-world deployment. The gateway was placed inside the semi-anechoic chamber at a distance of 5 m from the UUT, replacing the receiving antenna, which is chosen to represent a short-range deployment in the streets where a gateway will be installed.

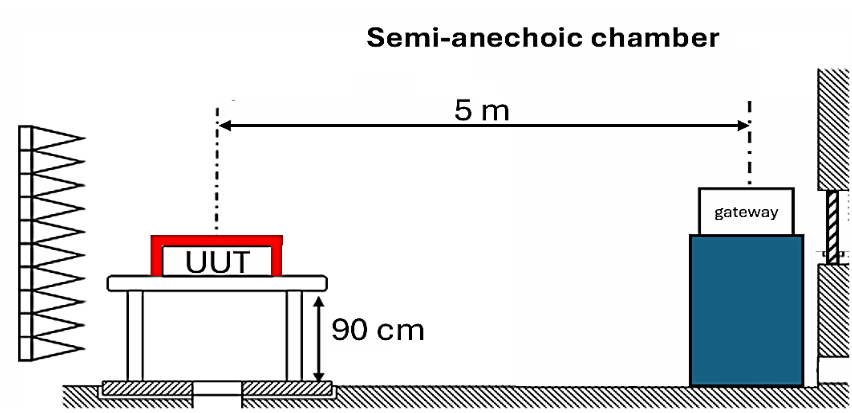


*Figure 5.10 Sensor node embedded in the cobblestone enclosure (Testbed B)*

The same four orientation angles used in Testbed A (0°, 90°, 180°, and 270°) were adopted here, and tests were run under both conditions: with and without a cobblestone enclosure surrounding the sensor node. As in the previous configuration, a final repeat of the battery influence test was included to confirm whether any differences had been observed between the with-cobblestone and without-cobblestone conditions.

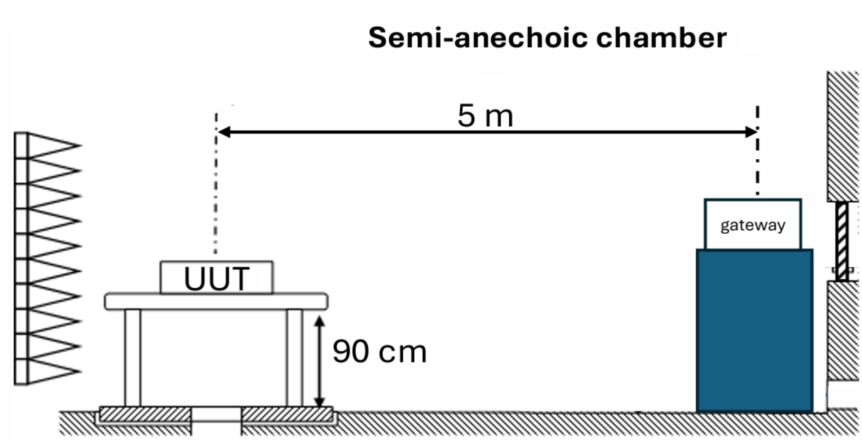


*Figure 5.11 Sensor without the cobblestone enclosure (Testbed B)*

The primary performance metric for this test of quality link was Packet Reception Rate (PRR). It is the percentage of data packets successfully received at the receiver side from the sender over a link in a network. PRR is calculated as the ratio between the total number of received packets and the total number of sent packets. This is crucial for evaluating the effectiveness of data reception over any communication channels. It is represented as,

$$PRR = \left(1 - \frac{\#packets_{sent} - \#packets_{received}}{\#packets_{sent}}\right) \quad (5.1)$$

A PRR of 100% indicates that every packet transmitted by the sensor node has been successfully received and decoded by the gateway, whereas a lower % indicates that packets have been lost due to signal distortion or interference. For each orientation angle and test conditions, exactly 5000 packets were transmitted.

## 5.4 MEASUREMENT RESULTS

### 5.4.1 Effect on the received power

The obtained results on the received power are reported in Figure 5.12. It reports the maximum received power levels for all tested orientations and for both the considered antenna polarisations.

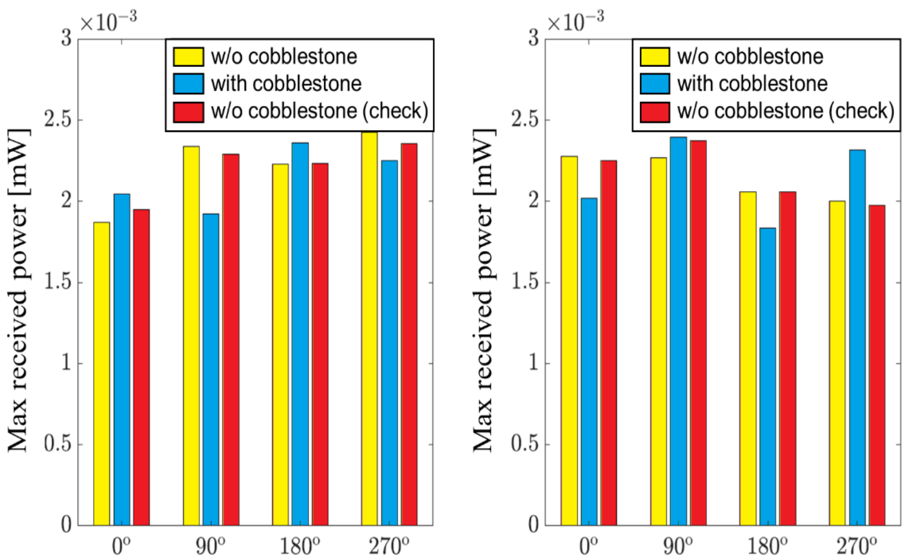


*(a) Horizontal polarisation (b) Vertical polarisation*

*Figure 5.12 Maximum received power levels*

Analysing the measurement results reported in this figure, it is possible to note that, although the results are not equal across all tested conditions, given the typical measurement uncertainties of the spectrum analyser used for these tests, they are compatible. Hence, the presence of the cobblestone has a negligible influence on the received power.

### 5.4.2 Effect on the Packet Reception Rate

The results of the PRR metrics are shown in Figure 5.13. The results show that across all four orientation angles and the test conditions (with and without a cobblestone enclosure), the PRR remained constant at 100%. It is worth noting that battery discharge didn't influence the results.

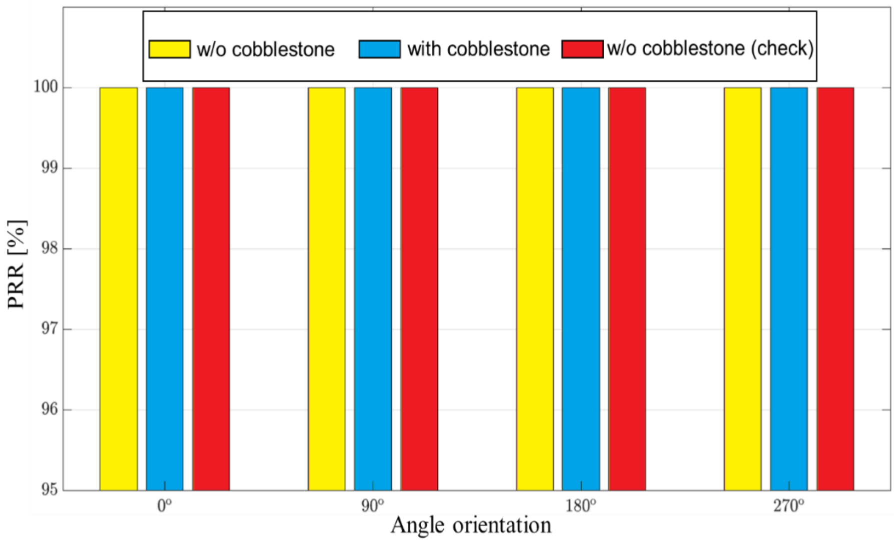


*Figure 5.13 Data communication test results*

## 5.5 A SENSOR NETWORK FOR THE PEDESTRIAN FLOW EXPOSURE

Since the beginning of the new millennium, the increasing impacts of natural disasters, often associated with rising pollution levels, have prompted nations to seek effective solutions. In particular, reducing environmental pollution, especially noise and air pollution generated by road traffic, has become a major priority. Consequently, researchers have increasingly focused on alternative mobility solutions, commonly referred to as sustainable mobility.

In response to these challenges, many policies have been developed to encourage people to shift away from private motor vehicles and adopt more sustainable modes of transportation. These policies promote multimodal mobility, which involves combining different modes of transport, such as public transit, cycling infrastructure, pedestrian pathways, and, where available, shared mobility services. Within this framework, walking plays a fundamental role, as it often represents the connecting element between different transport modes.

Despite its importance, the pedestrian component in urban mobility is frequently overlooked in infrastructure design. Many urban environments are poorly designed to accommodate pedestrian movement, leading to conflicts between pedestrians and vehicular traffic. Properly managing these interactions is therefore essential to improving safety and accessibility in urban areas.

For this reason, the design of road infrastructure must include an assessment of risk exposure. It is important to distinguish exposure from risk, which refers to the probability that a hazardous event will occur. Although closely related, these two concepts are not identical. For example, a high level of exposure, such as large numbers of pedestrians at a busy intersection, may correspond to relatively low risk if the infrastructure is properly designed and managed. Conversely, a location with low exposure, such as few pedestrians crossing a dangerous intersection, may still involve high risk and therefore a greater likelihood of harmful events. In the context of pedestrian safety, exposure is typically measured as the ratio of pedestrian accidents to pedestrian volumes.

More specifically, pedestrian exposure is the proportion of pedestrians who interact with potentially hazardous vehicular traffic. In practical terms, it can be measured as the annual number of vehicles–pedestrian collisions divided by the estimated annual pedestrian volume at a given intersection.

To estimate exposure accurately, it is first necessary to define the analysis's geographical scope. In the literature, study areas are generally categorised into two main types: facility-specific and area-wide analyses. Facility-specific studies focus on individual elements of the road system, such as points of location where traffic flows intersect, merge, or diverge, or segments, defined as portions of roadway between two points where traffic volumes and characteristics remain relatively constant.

By contrast, area-wide analyses consider broader spatial scales. These may include transport networks, which represent interconnected transport infrastructures within a medium-sized geographical area, or regions, which encompass all transport infrastructures within a defined political boundary.

The choice of geographic scale directly influences how exposure is measured and subsequently incorporated into risk assessment. Accordingly, different methodological approaches are used depending on the spatial level of analysis.

## 5.6 AN OVERVIEW OF COUNTING AND ESTIMATING TECHNOLOGIES FOR PEDESTRIANS

Pedestrian surveillance was mostly dependent on fixed, infrastructure-based sensing systems before the development of the Mobile Crowd Sensing (MCS). These approaches are still widely used in urban planning, road safety studies, and transportation engineering, but they have drawbacks in terms of cost, scalability, privacy, and environmental resilience. The rise in the popularity of smartphones and device-driven sensing techniques in recent years can be explained by an understanding of these limitations. A wide range of pedestrian-monitoring techniques exists in the literature, but this section focuses only on the most commonly and widely used methods [168], [169].

### 5.6.1 Manual Pedestrian Counts

It is one of the earliest and most popular methods of collecting data in transportation engineering. In this method, trained observers position themselves at key spots such as intersections, mid-block crossings, transit stations, or sidewalks, and document pedestrian movements using count sheets, mechanical clickers, or portable digital equipment. These methods require minimal equipment, can be deployed quickly, and remain standard practice for agencies conducting short-term traffic studies, safety audits, or the calibration of automated counting technologies [170].

***Advantages:***

This method is easy to organise, affordable, and does not require any specialised sensor equipment. Manual counts are especially effective in focused observational studies where human judgment is valuable, such as distinguishing between pedestrian types, identifying behavioural patterns, or documenting environmental factors like weather, obstructions, and even odd events. For these reasons, manual counting is often used as a ground truth reference for validating automated pedestrian detection systems.

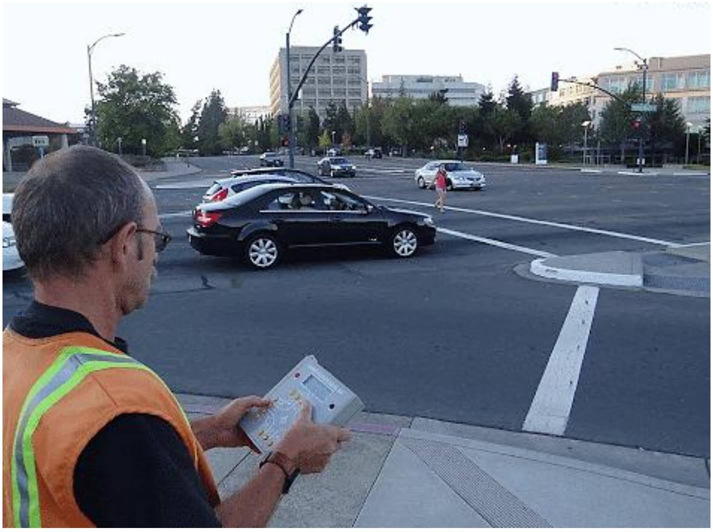

*Figure 5.14 An observer collecting real-time traffic and pedestrian data at an urban intersection*

***Limitations***

Manual counts have their limitations despite their ease of use. These methods are labour-intensive and time-consuming, often requiring numerous observers to cover a limited research area. This makes them unsuitable for continuous monitoring of large-scale installations. Human observers are also susceptible to fatigue, distraction, and subjective interpretation, which can lead to inconsistencies and inaccuracies in recorded data [170].

### 5.6.2 Video-based monitoring

This method is widely used in pedestrian studies, especially in metropolitan areas with an existing CCTV infrastructure. Traditional systems use fixed cameras to record the continuous video of pedestrian movement at junctions, crossings, transit hubs and other public spaces. Modern techniques improve these systems by incorporating computer vision algorithms that automatically recognise people, extract information about their trajectories, and analyse movement patterns. It is an effective tool for analysing pedestrian behaviour, evaluating safety, and enabling data-driven urban planning [171], [172].

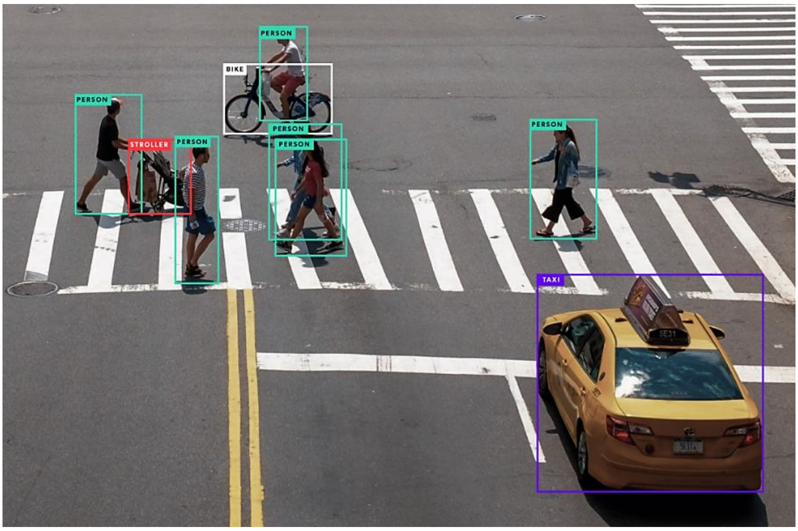


*Figure 5.15 Video-based recording for pedestrian counts*

***Advantages***

Video-based systems offer high spatial and temporal resolution, enabling precise surveillance of pedestrian movements. It captures detailed behavioural data, including the trajectories, speed, gap acceptance, and interactions with cars and people, unlike manual counts or sensor-based counters. It is also ideal for conflict safety analysis and safety investigations, as it provides precise movement data. Furthermore, once the camera is installed, the video systems can operate continuously and support effective analysis, allowing researchers to revisit the footage to analyse specific events or to validate automated outputs [171].

***Limitations***

The main limitation of video-based counting methods is the high cost of installing and maintaining the system, especially when cameras need to be mounted, powered, networked and calibrated for specific field circumstances. The performance can degrade significantly under bad weather, low-light conditions, or when the automobile or street objects block pedestrians.

Video captures identifiable imagery, raising privacy concerns and requiring strict compliance with data-protection regulations and ethical guidelines. Additionally, computer vision techniques require significant computational resources, especially for real-time processing and large-scale deployments, which may limit scalability [172].

### 5.6.3 Pressure-sensitive floors and smart carpets

They are often referred to as pressure mats or smart carpets. It uses the embedded force sensors to detect and estimate pedestrian presence, direction and counts. These carpets are often installed beneath flooring materials in building entrances, transit hubs, airport terminals, and other regulated indoor areas with high pedestrian traffic. When a human steps on the surface of this carpet, it detects changes in pressure distribution, allowing the system to determine footfall events and, in certain circumstances, fundamental movement patterns. Pressure-sensitive floorings are ideal for locations where video-based monitoring is not suitable or feasible due to privacy or architectural constraints [173].

*Figure 5.16 Example of a pressure-sensitive floor system used for footstep detection and pressure mapping*

***Advantages***

Pressure-sensitive carpets are highly accurate in small, controlled indoor areas where pedestrian movements occur in narrow entrances and hallways. These systems can also detect multiple simultaneous footsteps and operate continuously with minimal user interaction. In addition, pressure-sensitive carpets do not capture recognisable images like a camera-based system, thus providing a privacy-preserving alternative [173].

***Limitations***

Installing the sensors beneath the flooring surface is expensive, labour-intensive, and often feasible only during building construction or major renovations. The other factor to be considered is sensor maintenance, as constant foot traffic can cause wear and tear, leading to calibration drift or failure over time. Also, their detection range is limited, making them unsuitable for outdoor use and large-scale deployments. However, this system provides only limited behavioural information, such as footfall counts and estimates, and cannot extract information on trajectories, speeds, or other detailed interactions without additional sensing technologies.

### 5.6.4 Turnstile and Gate Counters

Turnstiles and automatic gate counters are among the most commonly used technologies for measuring pedestrian volumes in regulated environments such as metro stations, train platforms, stadiums, and some building entrances. These systems record each passing event when a person physically pushes through a mechanical barrier or passes through an electronic gate equipped with infrared or optical sensors. They can provide reliable, continuous data on pedestrian counts at entry and exit points, as they are incorporated into the access control infrastructure.

***Advantages***

Turnstile counters offer extremely high accuracy because each pedestrian must pass through a specific entrance point, eliminating inconsistencies in the count. They run continuously with minimal maintenance and are suitable for areas requiring access control. The data from the counter is linked to station management systems, enabling real-time monitoring of the individual's movements and supporting operational planning.


*Figure 5.17 Entry to a terminal showing automated turnstiles and access indicators*

*Limitations*

It is only applicable in controlled indoor environments and not suitable for open public areas and pedestrian lanes. These systems merely provide the aggregate entry and exit counts and do not record their trajectories. Their effectiveness depends on the assumption that all pedestrians who travel through the specific gates, which may not be true in all conditions, especially in uncontrolled entry areas.

## 5.7 IoT-BASED SENSING TECHNOLOGIES FOR MCS

Traditional pedestrian monitoring systems have their limitations; in particular, their dependence on fixed infrastructure, high deployment costs, and restricted spatial coverage have motivated the adoption of more flexible sensing approaches. MCS provides a feasible alternative to traditional methods by using data collected from users' mobile devices or IoT nodes. The adoption of low-cost IoT hardware and mobile crowdsensing systems has increased significantly, particularly for applications such as pedestrian flow monitoring and crowd dynamics analysis. Unlike traditional smartphones that rely on MCS techniques, IoT-based sensing systems utilise specialised sensor nodes that operate independently, continuously gathering and transmitting data without requiring human involvement or device ownership by those being observed. This section outlines the main enabling technologies for IoT-based crowd sensing: Bluetooth Low Energy (BLE), the ESP32 microcontroller platform, the MQTT protocol, and Wi-Fi for data transfer.

### 5.7.1 Proposal

Given that common people nowadays wear at least one device with a BLE interface, this research aimed to develop a wireless sensor network capable of estimating and quantifying pedestrian presence by counting the BLE interfaces detected in its monitoring area and providing a crowd index

### 5.8 SENSOR

The system developed in this thesis is a lightweight, privacy-preserving sensing pipeline that uses low-cost IoT nodes to estimate pedestrian presence in real time. The design focuses solely on counts, ensuring no personal information is stored or communicated.

*Figure 5.18 Sensor placed inside a cobblestone enclosure*

The core of the sensing system is the ESP32 microcontroller, which continuously scans for BLE advertisements from nearby smartphones and wearable devices. Once each scan duration is complete, the ESP32 collects the detected counts and transmits them to a central server using the MQTT publish protocol, implemented via the Mosquitto broker. MQTT is widely used in IoT applications because of its low bandwidth requirements and is also suitable for constrained devices operating over Wi-Fi networks. In this system, the two installed ESP32 nodes publish their count data to a dedicated MQTT topic via the university's Wi-Fi, enabling real-time data collection without additional communication hardware. Then, MQTT messages are received and logged in Excel-compatible datasets, enabling direct analysis of temporal patterns, pedestrian flow variations, and peak-hour dynamics.

### 5.8.1 ESP32 system

The sensor node in this system is based on the ESP32, a small and affordable microcontroller commonly used in IoT applications for its combination of wireless connectivity and modest processing capabilities. Its integrated Wi-Fi and Bluetooth options enable short-range sensing and network connectivity on a single chip, making it ideal for dispersed pedestrian monitoring applications that prioritise cost and simplicity [174]. In this context, the ESP32 is set to perform passive BLE scanning, listening for advertising packets from nearby smartphones and wearables.

The ESP-IDF framework controls the scan interval and window, allowing the device to balance the responsiveness and energy usage based on the monitoring needs. During each scan cycle, the ESP32 counts the number of detected devices, and when the scanning interval completes, it prepares the count for transmission. It can immediately forward data without interrupting the sensing process, as it is connected to Wi-Fi, and it can maintain the connection while scanning. This ability to simultaneously communicate over Wi-Fi and scan BLE is one of the reasons the ESP32 has become a widely used option in monitoring and smart-application research. The node then published the count to the central server using the MQTT pipeline described in detail in the following section.

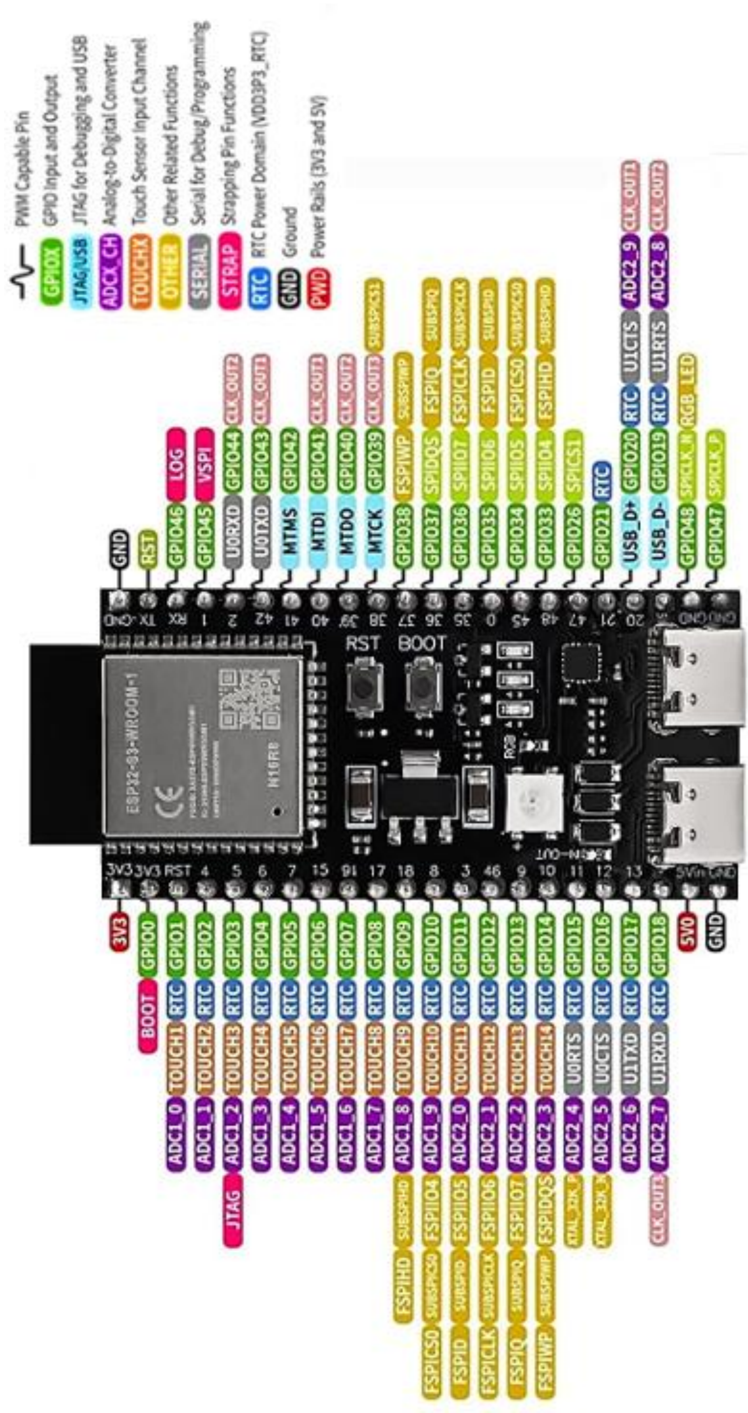


*Figure 5.19 Pinout diagram of the ESP32 module*

### 5.8.2 MQTT communication pipeline

Once each sensing interval is complete, the collected BLE measurements are transmitted to the server using the MQTT publish-subscribe protocol. It is widely used in IoT systems due to its lightweight, event-driven architecture and suitability for devices with limited processing and energy resources. Its low packet overhead and asynchronous communication approach make it ideal for distributed sensing deployments in which nodes deliver brief updates instead of continuous data streams.

In this system, each ESP32 node serves as an MQTT publisher, providing count data to a specific topic hosted by a Mosquitto broker. Mosquitto broker is an open-source MQTT implementation widely used in research and commercial settings for its reliability, minimal configuration requirements, and compatibility with limited devices. The ESP32 connects to the university network via Wi-Fi, allowing for instant message publication after each scan cycle without disrupting the sensing process [175].

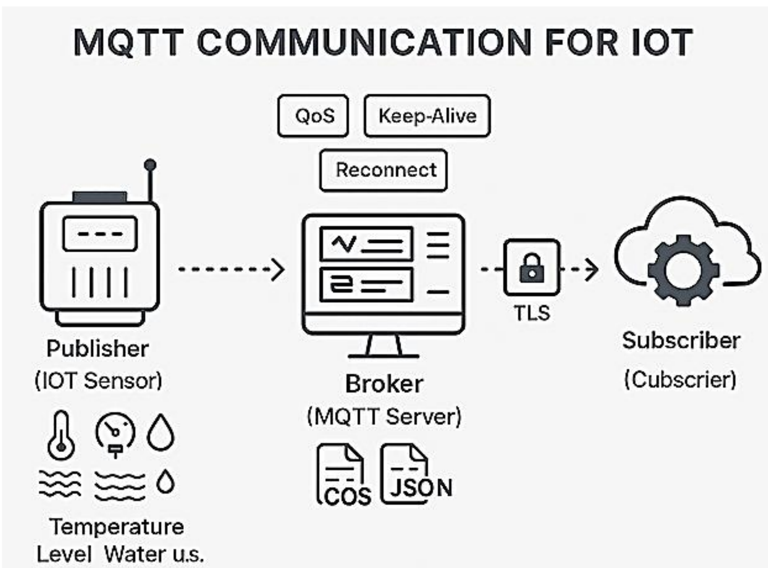


*Figure 5.20 Secure IoT telemetry pipeline using MQTT*

An MQTT subscriber on the server listens to the selected topics and records the messages that arrive. Each message stores the scan interval timestamp and device counts in an Excel file for further analysis. This basic logging pipeline enables quick data evaluation and integration with typical analytical tools, while keeping the system simple to maintain and extend.

MQTT ensures the communication layer remains efficient even when multiple sensor nodes are deployed. Because MQTT separates publishers and subscribers, new nodes can be added without changing server settings, making the architecture naturally scalable. This approach is consistent with IoT communication norms, as MQTT is a commonly used protocol [175]-[177].

### 5.8.3 Ground Truth installation

To validate the BLE-based pedestrian flow, a video camera was placed in the campus atrium to monitor the pedestrian movement. The camera was positioned to provide the maximum coverage of the atrium's main pedestrian flow area. The video footage was captured synchronously with the ESP32 sensor data collection, using the test session's common time duration. Pedestrian counts were derived from the camera using an algorithm, and then later, the correlation between the two data sets (ESP32 and the ground truth) was performed to understand the temporal alignment between the two data streams.

It should be noted that the camera's field of view only includes a portion of the physical space monitored by the ESP32 sensor. The scan range is not restricted to the camera's field of view, allowing the sensor to identify BLE devices from humans outside the camera's field of view. This spatial mismatch between the BLE scanner's sensing and visual coverage is an inherent feature of the experimental setting and is accounted for when processing the results.

### 5.9 A PRELIMINARY CHARACTERIZATION

Since precise characterisation has been carried out, testing the quality of the communication link using the sensor node as a transmitter requires that it be able to sense the BLE network interfaces; as a consequence, it must be tested as a receiver.

To this aim, a new test campaign in the semi-anechoic chamber has been designed and carried out. The designed test-bed is similar to that reported in Figure 5.10, but in this case, instead of the gateway, a smartphone equipped with a BLE interface is used to detect it. It was positioned at 4 different distances from the sensor node: 1 m, 2 m, 3 m, and 4 m, respectively.

For each distance, 8 different orientations have been considered: 0°, 45°, 90°, 135°, 180°, 225°, 270°, 315°. For each combination of distance and angle, the sensor was set to acquire data for 1 minute. In particular, the value of the Received Signal Strength Index (RSSI) has been saved. At the end of each test, the mean value and the standard deviation of the acquired RSSI values have been calculated.

The following picture shows the polar diagram of the measured RSSI.

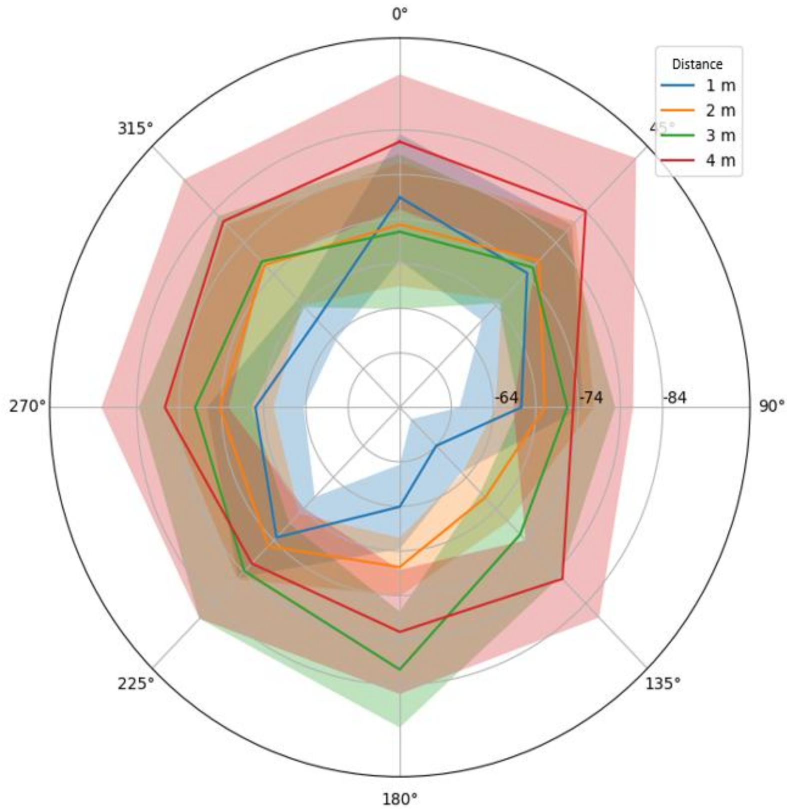


*Figure 5.21 RSSI polar diagram*

As expected, the received signal decreases as the smartphone moves farther from the UUT. Furthermore, the results across different orientations are very similar, except for those at 90°. In this case, the RSSI is higher.

## 5.10 MEASUREMENT RESULTS IN REAL OPERATING CONDITIONS

### 5.10.1 Deployment locations of the sensor

The experimental test was carried out at the University of Cassino and Southern Lazio campus.

***University Atrium:***

The deployment location was the university atrium, which is a semi-open test environment and a high-traffic indoor facility that serves as a key circulation and meeting place. The atrium experiences variable and less predictable pedestrian flow compared to the conference room, with both stationary and moving individuals contributing to the crowd at different times. This setting is more typical of real-world crowd-sensing challenges, such as dynamic and diverse device populations, shifting geographic distributions of individuals, and higher levels of environmental RF interference.

### 5.10.2 Test Event

The test sessions were conducted over two consecutive days (10.02.2026 and 11.02.2026) during the University's Open Day, a scheduled institutional event that attracts a large number of visitors, potential students, and accompanying individuals to the campus. This day was purposely chosen because it has an increased and changing pedestrian density, making it ideal for testing the BLE-based sensor system's response to real-world crowd dynamics. On event day, the atrium and conference room experienced periods of high occupancy during presentations, waiting time, and general circulation, and a low density of people during the transition between sessions and at the conclusion of the event day. This fluctuation in crowd density is essential for accurately determining the BLE device count signal in response to variations in real pedestrian presence.

### 5.10.3 Data acquisition and processing

At each test site, the ESP32 sensor node was powered with a power adapter and connected to the university Wi-Fi network before the test session. Once the MQTT connection to the local broker was confirmed, BLE scanning and data publishing began and continued throughout the session. The ESP32 node performed continuous passive BLE scanning and detected advertising packets from discoverable BLE devices within its scan range. After each scanning session, the device count was sent to the broker. The broker recorded all incoming messages and their timestamps, resulting in a comprehensive time-series record of BLE device counts for each test location.

After data collection, the raw MQTT logs and video annotation records were pre-processed prior to the final analysis. It includes temporal alignment, in which the sensor data timestamps and video recording timestamps are aligned to a common time reference (5 seconds in this case) to ensure that the BLE device counts and ground truth pedestrian counts match at each time step.

## 5.11 RESULTS AND ANALYSIS

To evaluate how well the ESP32 BLE sensor reflects actual pedestrian activity, the device count data collected from the sensor placed in the university atrium was directly compared with the pedestrian counts extracted from the video camera, which served as ground truth. The results from both days are presented below, with the observation drawn directly from the time-series plot of the two datasets.

***Day-1 (10.02.2026)***

The first session ran from 09.20 in the morning to 12:43 in the afternoon, providing a total observation window of over 5 hours. The figure below shows the side-by-side time series of the BLE sensor-detected device count (Orange) and the video-based pedestrian count (Blue).

The spiky behaviour observed in the plot is typical of BLE scanning in busy environments, where 100-125 devices were present, with the highest recorded value of 143 around 11 AM. After that, the sensor count started to elevate, oscillating between 30 and 135 devices.

The blue line, representing pedestrian counts from the video recordings, is also almost consistent with the orange line, indicating that despite the clear numerical gap between them, they move together. The correlation coefficient between these two series quantifies how closely the sensor's device counts track the actual pedestrian count over time. The X-axis represents time (hh:mm: ss) during the test. The y-axis represents counts, with values for both pedestrians (video ground truth) and the sensor output. The Pearson correlation coefficient $r$ was 0.814317, indicating a strong positive linear correlation.

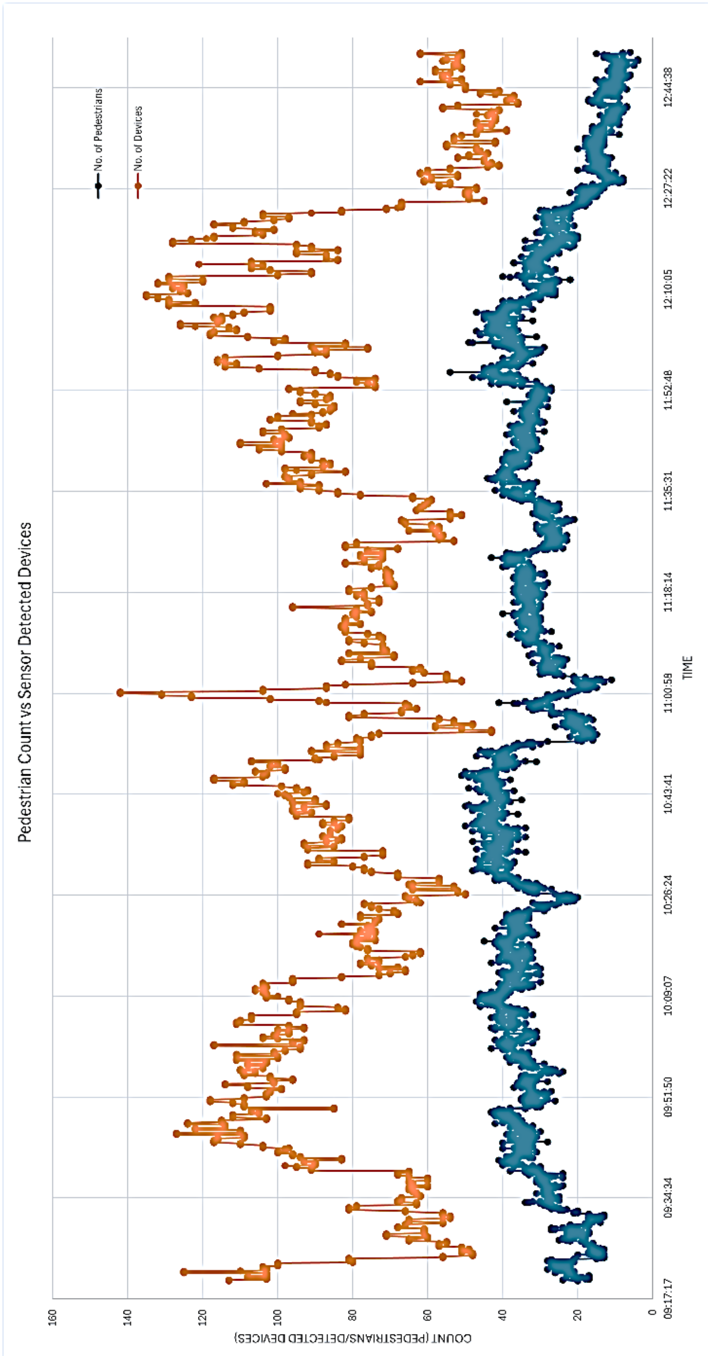


*Figure 5.22 Pedestrian count from the Video ground truth and the number of devices detected by the ESP32 sensor*

***Day-2 (11.02.2026)***

The second test session, shown in the following figure, started at 10:27 in the morning, spanned a longer window, and continued till 13:46 in the late afternoon. Between the start of the session and 11:30, the device count has been fluctuating between 40 and 137. Later, at 11:28, the sensor count began to rise more consistently, building a clear peak from 12:05 to 12:20, with a maximum of 163 devices detected, making it the highest recorded device count. After midday, the graph starts to decline.

Even in this case, there is a strong correlation between the pedestrians shown in the video and the number of devices detected by the sensor, with the Pearson correlation coefficient $r$ of 0.827454. However, the number of devices detected exceeds the actual pedestrian count. This discrepancy arises primarily from multiple BLE-enabled devices per individual and from fixed infrastructure devices that continuously advertise Bluetooth signals.

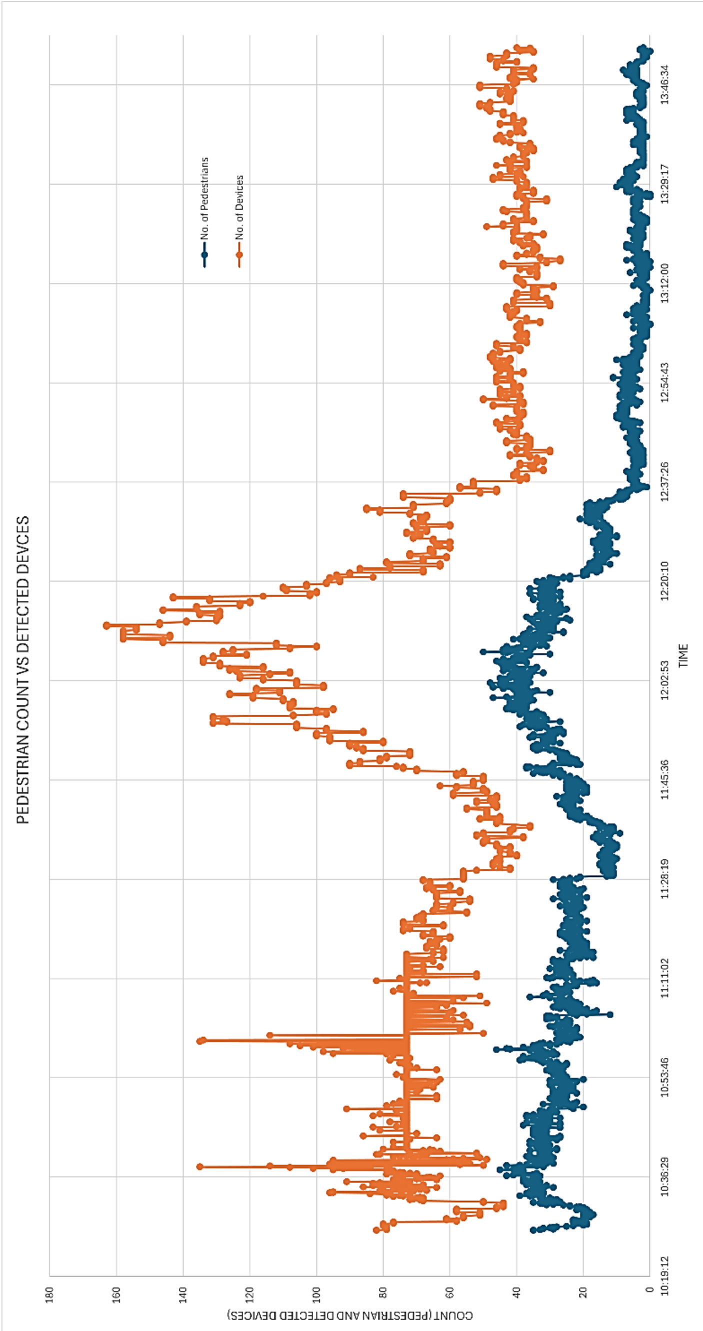


*Figure 5.23 Pedestrian count from the Video ground truth and the number of devices detected by the ESP32 sensor*

Additionally, the overnight test confirmed a stable baseline, with the sensor consistently detecting about 3 to 5 devices even when no people were present in the room. These baseline results are from static BLE-emitting devices in the environment.

From a methodological standpoint, BLE device counts should be seen as an indirect indicator of multiple devices rather than a direct count of individuals. Multiple devices per person can introduce a systematic bias in the measurements, but this bias tends to stay relatively consistent in the same environment. Consequently, even though the absolute numbers may vary, the pattern of BLE detections over time aligns with pedestrian flow dynamics. This explains the strong correlation observed, supporting the use of BLE sensing for monitoring relative changes in pedestrian density. It is important to note that the main operational benefit of this system is tracking changes in pedestrian activity over time, rather than providing exact counts at every moment. The strong correlation between the BLE index and ground-truth data confirms this.

In the future, a calibration-based approach could enhance the estimation of actual pedestrian counts from BLE measurements by modelling the link between BLE detections and true pedestrian data, while accounting for systematic biases like multi-device ownership and background infrastructure signals.

## *CONCLUSION*

This thesis investigated how sensing technologies can support smart mobility by characterising motion and pedestrian activity measurements. The study demonstrated that various mobility applications require different types of sensing: some require accurate velocity estimation, while others require monitoring changes in pedestrian flow.

One key conclusion is that while GNSS-based velocity estimates may be highly useful for mobility applications, the processing technique and measurement conditions significantly affect their reliability. The results demonstrated that, even in a stationary setting, poor satellite geometry can make the Doppler-based estimate unstable. Tikhonov regularisation also increased the solutions' stability, demonstrating that these restrictions can be relaxed with appropriate signal processing.

In addition, the thesis showed how smartphone-based GNSS sensing can be applied to pedestrian-related tasks, such as identifying a pedestrian waiting at a junction to cross the road. The viability of this method is supported by the TDCP-based findings, which remained near zero in open-sky, semi-urban, and dense-urban settings. The overall results indicate that consumer smart devices can also provide useful speed information to pedestrian smart mobility systems.

The BLE-based crowd-sensing study concludes that it was able to track changes in pedestrian activity over time, with strong correlation with ground truth. This means the system is better suited for monitoring trends and variation in crowd presence than for precise pedestrian counting. Even so, this is valuable for real-world smart mobility applications, where understanding how pedestrian activity changes over time can support better planning and management. Additionally, biases like multi-device effects and background BLE signals were identified. A calibration-based method is proposed as future work to enhance pedestrian count estimates from raw BLE data.

The thesis concludes that practical smart mobility sensing must be judged not only by technical accuracy but also by its deployment flexibility. While the BLE work focused on simplicity, scalability, and applicability to real-world situations, the GNSS-based analysis focused on the measurement behaviour and reliability under controlled conditions. When taken as a whole, these studies show that mobility sensing systems must be both inexpensive and reliable enough for use in a real-world environment. This balance is crucial for applications involving pedestrians, since sensing must frequently operate in constrained urban areas and with limited tolerance for, or the cost of, invasive hardware.

This thesis's main scientific contributions are: 1) experimental characterisation of Doppler-based GNSS velocity estimation in controlled lab settings, considering satellite geometry and regularisation; 2) validation of TDCP-based velocity estimation for low-dynamic pedestrian use with consumer smartphones; 3) assessment of BLE-based sensing as an indicator for tracking temporal changes in pedestrian activity indoors.

### *FUTURE WORK*

Regarding GNSS-based velocity estimation, future research could explore adaptive methods for selecting the Tikhonov regularisation parameter in real time, using an instantaneous PDOP as a trigger rather than relying on a fixed value during post-processing. This approach would enable the estimator to adapt dynamically to geometry degradation without manual adjustment. Additionally, expanding the SDR testbed to handle simultaneous multi-constellation signals could help determine whether increased geometric diversity across constellations reduces the likelihood of ill-conditioned matrices in dense urban environments and canyons.

The current work of the second contribution evaluates only stationary conditions. A natural extension is to characterise TDCP performance under actual low-speed walking dynamics, thereby determining whether the zero-velocity threshold remains robust as a pedestrian slowly decelerates towards a junction. Additionally, testing across a broader set of chipsets that lack an integrated sensor hub would clarify whether the metrological compatibility result is dependent on the internal IMU fusion present in one of the tested devices.

Future work on BLE-based crowd sensing should aim to create a calibration model that converts device counts into more precise pedestrian estimates. This involves gathering ground-truth data across diverse settings, such as outdoor pedestrian zones, narrow urban streets, and transit hubs, to understand how the relationship between device counts and real pedestrian density varies across contexts. Furthermore, integrating BLE-based occupancy sensing with GNSS-derived pedestrian velocity into a single framework could facilitate more responsive smart mobility solutions, such as adaptive lighting control systems.

## *BIBILIOGRAPHY*


1 A. Pojani and D. Stead, "*Sustainable Urban Transport in the Developing World: Beyond Megacities*", Sustainability, vol. 7, no. 6, pp. 7784-7805, 2015.

2 J. Rodrigue, "*The Geography of Transport Systems*", 5th ed. New York, NY, USA: Routledge, 2020.

3 F. Creutzig, M. Franzen, R. Moeckel, et al., *"Leveraging digitalisation for sustainability in urban transport*", Global Sustainability, vol. 2, e14, 2019.

4 European Environment Agency, "*Transport and Mobility*", EEA, 2025 [Online]

5 H. Ritchie, V. Samborska, and M. Roser, "*Urbanisation*", Our World in Data, 2024.

6 Population Reference Bureau, "*Percent of population living in urban areas*", International Data, 2024. [Online]

7 United Nations, "*Department of Economic and Social Affairs, Population Division*, World Urbanisation Prospects: The 2025 Revision", United Nations, 2025.

8 European Environment Agency, "*Greenhouse gas emissions from transport in Europe*", EEA, 2025. [Online]

9 European Environment Agency, "*Sustainability of Europe's mobility systems: Climate*", EEA 2024. [Online]

10 World Health Organisation, "*Transport: Sectoral solutions for air pollution and health*", WHO reference no. B09368, 2025. [Online].

11 World Health Organisation, "*Global status report on road safety 2023*", WHO, Geneva, 2023. [Online]

12 World Health Organisation, "*Road traffic injuries: Key facts*", WHO, 2023. [Online]

13 World Health Organisation, "*Global road safety report: Data tables 2021*", WHO, Geneva, 2021. [Online]

14 European Transport Safety Council, "*2025 Annual PIN report*", ETSC, Brussels, 2025.

15 European Commission, "*The European Green Deal*", Brussels, 2020. [Online]

16 European Environment Agency (EEA), "*Premature deaths due to exposure to fine particulate matter in Europe*", 2025.

17 European Environment Agency (EEA), "*Air quality status report*", 2025.

18 Commission of the European Communities, "*Green Paper on the Impact of Transport on the Environment: A Community Strategy for Sustainable Mobility*", COM(92) 46 final, 20 Feb. 1992.

19 E. Holden, G. Gilpin, and D. Banister, "*Sustainable Mobility at Thirty*", Sustainability, vol. 11, no. 7, p. 1965, 2019.

20 D. Angarita-Lozano, D. Hidalgo-Guerrero, S. Diaz-Marquez, M. Morales-Puentes and M. A. Mendoza-Moreno, "*Multidimensional Evaluation model for Sustainable and Smart Urban Mobility in Global South Cities: A Citizen-Centred Comprehensive Framework*", Sustainability, vol. 17, no.10, p. 4684, 2025. doi: 10.3390/su17104684.

21 F. Filippi, "*A Paradigm Shift for a Transition to Sustainable Urban Transport*", Sustainability, vol. 14, no. 5, p. 2853, 2022.

22 European Commission, "*Mobility Strategy",* Mobility and Transport, European Union. [Online].

23 European Commission, "*Sustainable & smart mobility*", Mobility and Transport, 2024.

24 World Health Organisation, "*Pedestrian Safety: A Road Safety Manual for Decision Makers and Practitioners*". Geneva, Switzerland: WHO, 2013.

25 World Health Organisation, "*Cycling Safety: an information resource for decision-makers and practitioners*". Geneva, Switzerland: WHO, 2020.

26 R. Cervero and C. Radisch, "*Travel choices in pedestrian versus automobile-oriented neighbourhoods*", Transport Policy, vol. 3, pp. 127-141, 1996.

27 R. Arroyo, L. Mars, and T. Ruiz, "*Perceptions of Pedestrians and Cyclist Environments, Travel Behaviours, and Social Networks*", Sustainability, vol. 10, no. 9, p. 3241, 2018.

28 City of Copenhagen, "*Copenhagen City of Cyclists: Bicycle Account 2022*". Copenhagen, Denmark: Technical and Environmental Administration, 2022.

29 City of Amsterdam, "*Long-term Bicycle Plan 2017-2022*". Amsterdam, Netherlands: Municipality of Amsterdam, 2017.

30 City of Vienna, "*Urban Mobility Plan Vienna*". Vienna, Austria: Municipal Department 18- Urban Development and Planning, 2015.

31 International Transport Forum, "*Cycling Safety*". Paris, France: ITF, 2018.

32 European Commission, "*Quality of Life in European Cities 2020*". Brussels, Belgium: Publications Office of the European Union, 2020.

33 O. Yusuf, A. Rasheed, and F. Lindseth, "*Leveraging Big Data and AI for Sustainable Urban Mobility Solutions*", Urban Science, vol. 9, no. 8, 2025.

34 European Commission Expert Group on "*Inclusive and sustainable future of urban mobility in Europe*", 2025.

35 M. V. Sanchez-Sepulveda, J. Navarro, D. Amo-Filva, D. Fonseca, F. Antúnez-Anea, and A. Barranco-Albalat, “*A data-driven approach to enhance urban infrastructure for sustainable mobility and improved quality of life in highly populated cities. Case study: Barcelona*,” Frontiers in Built Environment, vol. 10, art. 1439700, 2024.

36 European Commission, “*Sustainable and Smart Mobility – Putting European Transport on Track for the Future*”. Brussels, Belgium. 2020.

37 United Nations Economic Commission for Europe (UNECE), “*Intelligent Transport Systems for Sustainable Mobility*”, Geneva, Switzerland, 2012.

38 J. Lee, “Introduction to Navigation Systems”, 2018. doi: 10.5772/intechopen.71047

39 Wikipedia, “Navigation”, Jan. 1 2026. Accessed Jan. 7, 2026[Online].

40 M. K. Pandey, P. K. Srivastava, and G. P. Petropoulos, “Future pathway for research and emerging applications in GPS/GNSS”, in GPS and GNSS Technology in Geosciences, Elsevier, 2021. doi: 10.1016/B978-0-12-818617-6.00006-8

41 P. Misra and P. Enge, “Global Positioning System: Signals, Measurements, and Performance”, 2nd ed., Ganga-Jamuna Press, 2011.

42 E. D. Kaplan and C. J. Hegarty, “Understanding GPS/GNSS: Principles and Applications”, 3rd ed., Artech House, 2017.

43 P. J. G. Teunissen and O. Montenbruck,”Springer Handbook of Global Navigation Satellite Systems”, Springer, 2017.

44 U.S. Coast Guard Navigation Centre, “IS-GPS-200 Navstar GPS Space Segment/Navigation User Interfaces,” IS-GPS-200N, Aug. 1, 2022.

45 European Union Agency for the Space programme, “Galileo Open Service Signal-In-Space Interface Control Document (OS SIS ICD), Issue 2.2”, Nov. 2025.
46 China Satellite Navigation Office, “BeiDou Navigation Satellite Systems Signal-in-Space Interface Document” (Open Service Signal B1C version 1.0), 2017.
47 International Civil Aviation Organisation, “Annex 10 to the Convention on International Civil Aviation, Volume I: Radio Navigation Aids”.
48 RTCA, “DO-229D: Minimum Operational Performance Standards for Global Positioning System / Wide Area Augmentation System Airborne Equipment”, RTCA, 2006.
49 B. Hofmann-Wellenhof, H. Lichtenegger, and E. Wasle, “GNSS: Global Navigation Satellite Systems: GPS, GLONASS, Galileo, and More”, Springer, 2008.
50 W. A. Ahmed et al., “Evolution of GNSS/GPS technology and its applications from ancient times to the present”, New Res., 2025. doi: 10.1016/j.nexres.2025.100387.
51 P. Fernandez and H. J. Spiers, “Wayfinding across ocean and tundra: What traditional cultures teach us about navigation”, Trends in Cognitive Science, vol. 28, no.1, pp. 56-71, 2024.
52 P. Zabalegui et al., “A review of the evolution of the integrity methods applied in GNSS”, IEEE Access, vol. 8, pp. 45813-45824, 2020. doi: 10.1109/ACCESS.2020.2977455.
53 European Space Agency, “GNSS Augmentation Systems Overview” Navipedia. [Online]
54 International Civil Aviation Organisation, “Global Navigation Satellite Systems (GNSS) Manual”.

55 European Space Agency, "SBAS Fundamentals", Navipedia. [Online]
56 SKYbrary, "Satellite Based Augmentation Systems (SBAS)", SKYbrary Aviation Safety. [Online].
57 C. Hegarty and R. Munro, "An Introduction to GNSS: A Primer in Using Global Navigation Satellite Systems for Positioning and Autonomy". NovAtel Inc., 2023.
58 W. Gao, L. Chen, F. Lv, X. Zhan, L. Chen, Y. Liu, Y. Dai, and Y. Jin, "Initial Design for Next-Generation BeiDou Integrity Subsystem: Space–Ground Integrated Integrity Monitoring," Remote Sensing, vol. 16, no. 22, p. 4333, 2024. doi: 10.3390/rs16224333.
59 European Space Agency, "GBAS Fundamentals", Navipedia. [Online]
60 S. Basak et al. "Ground Based Augmentation System (GBAS)", Istanbul Aydin Univ. J., vol. 11, pp.205-215, 2019. doi: 10.17932/IAU.IAUD.m.13091352.2019.2/42.205-215.
61 S. Gaglione and M. Vultaggio, "GBAS-Ground Based Augmentation System, an Italian Experience", in Proc. ENC, 2006.
62 Federal Aviation Administration, "GBAS(Ground Based Augmentation System) – How it works", 2023 [Online]
63 European Space Agency, "Aviation Applications", Navipedia, 2011.
64 International Civil Aviation Organisation, "Performance-Based Navigation (PBN) Manual", 2007.
65 EUROCONTROL, "GNSS Elements", ePBN Portal, 2024.
66 J. Sanz Subirana, J. M. Juan Zornoza, and M. Hernández-Pajares, GNSS Data Processing: Volume I: Fundamentals and Algorithms, ESA TM-23/1, European Space Agency, Noordwijk, The Netherlands, 2013.

66 J. Sanz Subirana et al., "GNSS Signal", Navipedia, 2011.

67 U.S. Coast Guard Navigation Centre, "NAVSTAR GPS Space Segment/Navigation User Segment Interfaces", IS-GPS-200N, Aug. 2022. [Online].

68 C. Hegarty, "Overview of the Global Navigation Satellite Systems (GNSS)", Workshop on GNSS Data Application to Low Latitude Ionospheric Research, May 2013.

69 U.S. Naval Observatory, "Global Positioning System Overview".

70 J. A. Avila-Rodriguez, "GPS Signal Plan", Navipedia, 2011.

71 J. Sanz Subirana et al., "GPS Navigation Message", Navipedia, 2011

72 J. Van Sickle, "GPS for Land Surveyors", 4th ed., CRC Press, 2015.

73 A. Darya et al., "GPS carrier-to-noise density predictions using regression trees", Proceedings of the International Astronautical Congress, IAC, 2022.

74 European Space Agency, "Generic Receiver Description", Navipedia, 2011.

75 M.S. Braasch and A. J. Van Dierendonck, "GPS Receiver architecture and Measurements", TU Delft OpenCourseWare, 2009.

76 European Space Agency, "Front End", Navipedia, 2025.

77 H. N. Htay, Z. M. Lwin, and T. Hla, "Implementation of Signal Acquisition and Tracking for GPS-Based Software Defined Radio Receiver," International Journal of Geoinformatics, vol. 19, no. 2, pp. 55–64, 2023. doi: 10.52939/ijg.v19i2.2567

78 European Space Agency, "Digital Signal Processing", Navipedia, 2011

79 W. Ding and J. Wang, “Precise velocity estimation with a stand-alone GPS receiver”, Journal of Navigation, vol. 64, 2011, doi: 10.1017/S0373463310000482.
80 T. Suzuki, “Precise position estimation using smartphone raw GNSS data based on two-step optimization”, Sensors, vol. 23, no. 3, art. 1205, 2023.
81 Q. Liu, R. Ying, Z. Dai, Y. Wang, J. Qian, and P. Liu, “Multi-phase fusion for pedestrian localization using mass-market GNSS and MEMS sensors”, Sensors, vol. 23, no. 7, 2023.
82 V. Gikas and H. Perakis, “Rigorous performance evaluation of smartphone GNSS/IMU sensors for ITS applications”, Sensors, vol. 16, no. 8, 2016.
83 A. Angrisano, M. Vultaggio, S. Gaglione, and N. Crocetto, “Pedestrian localisation with PDR supplemented by GNSS”, in 2019 European Navigation Conference (ENC), 2019, pp. 1-6.
84 L. Ji, R. Sun, Q. Cheng and J. Wang, “Evaluation of the performance of GNSS-based velocity estimation algorithms”, Satellite Navigation, vol. 3, no. 1, p. 18, 2022.
85 Y. Li, L. Wang, J. Liu, P. Zhang, and Y. Lu, “Accuracy Evaluation of Multi-GNSS Doppler Velocity Estimation using Android Smartphones”, International Archives of Photogrammetry, Remote Sensing and Spatial Information Sciences, vol XLVI-3/W1-2022 7th Intl. Conference on Ubiquitous Positioning, Indoor Navigation and Location-Based Services (UPINLBS 2022), 18–19 March 2022, Wuhan, China
86 Z. Dong, Y. Wu and J. Wang, "Kalman Filter and Extended Kalman Filter: Theory, Numerical Applications and Performance Analysis," 2025 5th International Symposium on Computer Technology and

Information Science (ISCTIS), Xi'an, China, 2025, pp. 532-538, doi: 10.1109/ISCTIS65944.2025.11065026.

87 D-J. Jwo and A. Biswal, “Implementation and Performance Analysis of Kalman Filters with Consistency Validation”, Mathematics, vol. 11, no. 3, 2023. doi: 10.3390/math11030521

88 P. Freda, A. Angrisano, S. Gaglione, and S. Troisi, “Time-differenced carrier phases technique for precise GNSS velocity estimation,” GPS Solutions, vol. 19, no. 2, pp. 335–342, 2015.

89 F. Van Graas and A. Soloviev, “Precise Velocity Estimation Using a Stand-Alone GPS Receiver,” Navigation, vol. 51, no. 4, pp. 283–292, 2004.

90 M. Petovello and S. Gaglione, “How does a GNSS receiver estimate velocity?” pp.38–41, 2015.

91 Z. Chen, F. Guo, and L. Luo, “Vehicle speed measurement technologies in Intelligent Transportation Systems: current status, challenges, and future directions”, Artificial Intelligence and Autonomous Systems, vol. 1, no. 2, 2024, Art. No. 0004, doi: 10.55092/aias20240004

92 L. Mooren, “Safe System Speed Management”, Journal of Injury and Violence Research, vol. 11, no. 2, 2019.

93 European Parliamentary Research Service, “Sustainable and Smart Mobility Strategy”, European Parliament, Brussels, Belgium, Briefing, 2021.

94 J. Oskarbski, T. Kaminski, K. Kyamakya, J. C. Chedjou, K. Zarski, M. Pedzierska, “Assessment of the speed management impact on road safety on the sections of Motorways and Expressways using simulation methods”, Sensors, vol. 20, no.18, art. 5057, 2020.

95 A. Angrisano, G. Capaldo, S. Del Pizzo, and S. Gaglione, “Time-Differenced Carrier Phase Technique for Precise Velocity Estimation

on an Android Smartphone", Sensors, vol. 22, no. 21, art. no. 8514, Nov. 2022. doi: 10.3390/s22218514.

96 X. Xiao, X. Ren, and H. Li, "An Interial Sequence Learning Framework for Vehicle Speed Estimation via Smartphone IMU", arXiv:2505.18490, May 2025.

97 B. Or, "CarSpeedNet: A Deep Neural Network-Based Car Speed Estimation from Smartphone Accelerometer", arXiv:2401.07468, 2024.

98 Y. Jiang et al., "Accurate Vehicle Manoeuvre Analysis Using Smartphone GNSS Carrier-Phase Measurement", TechRxiv, 2023.

99 J. Wan et al., "Mobile Crowd Sensing for Traffic Prediction in Internet of Vehicles", Sensor, vol. 16, no. 1, 88, Jan 2016. doi: 10.3390/s16010088.

100 J. Xue, Y. Xu, W. Wu, T. Zhang, Q. Shen, H. Zhou, and W. Zhuang, "Sparse Mobile Crowdsensing for Cost-Effective Traffic State Estimation with spatio-temporal transformer graph neural network", IEEE Internet of Things Journal, vol.11, no.9, 2024. doi: 10.1109/JIOT.2024.3356554

101 L. Ji, R. Sun, Q. Cheng, and J. Wang, "Evaluation of the performance of GNSS-based velocity estimation algorithms", Satellite Navigation, vol. 3, 2022, art. 18. doi: 10.1186/s43020-022-00080-4

102 Y. Gao, Y. Jiang, B. Liu, and Y. Gao, "Integrity monitoring of multi-constellation GNSS-based precise velocity determination in urban environments", Measurement, vol. 222, 2023, Art.no. 116676. doi: 00.1016/j.measurement.2023.113676

103 S. Li, R. Yang, and X. Zhan, "Characterisation of multi-band GNSS multipath in urban canyons using the 3D ray-tracing method", GPS Solutions, vol. 28, Art. no. 49, 2024. doi: 10.1007/s10291-023-01590-7

104 L. Zhang, G. Chang, C. Chen, S. Zhang, and T. Zhu, "GNSS velocimeter by adaptively combining carrier phase and Doppler measurements", IET Science, Measurement and Technology, vol. 14, no. 7, pp. 823-832,2020. doi: 10.1049/iet-smt.2018.5674.

105 K. Borre, D. M. Akos, N. Bertelsen, P. Rinder, and S. H. Jensen, "*A Software-Defined GPS and Galileo Receiver: A Single-Frequency Approach*". Boston, MA, USA: Birkhäuser, 2007

106 E. Kaplan and C. Hegarty, "Understanding GPS/GNSS: Principles and Applications, 3rd ed., 2017.

107 NovAtel Inc., "GPS-702-GG Antenna Specifications", product datasheet.

108 Global Positioning Systems Directorate, *Navstar "GPS Space Segment/Navigation User Segment Interfaces"*, IS-GPS-200N, Aug. 2022

109 National Instruments, "USRP-2950R Specifications", technical documentation

110 MathWorks, "Baseband Sample Rate in NI USRP Radios", Wireless Testbench Documentation. [Online].

111 European Space Agency, "Tracking Loops", Navipedia.

112 H. Bao, "Delay Lock Loop Assisted Phase Lock Loop for GNSS signal Tracking", Journal of Communications, vol. 11, no. 5, pp. 471-477, 2016. Available: https://www.jocm.us/uploadfile/2016/0524/20160524043245528.pdf

113 X. Zhang, X. Zhan, and J. Shen, "An open-source real-time software vector tracking GNSS receiver: Design, tests, and results", Proc. 2013 Int. Tech. Meeting Inst. Navig., 2013. pp. 351-358.

114 TMBOC, “SoftGNSS: Open-source MATLAB GNSS Software Receiver”, GitHub repository. Available: https://github.com/TMBOC/SoftGNSS
115 P. Ward, “GPS receiver tracking loop performance”, in Proc. ION GPS 1996, 1996.
116 D. Borio and G. Lachapelle, “A non-coherent architecture for GNSS digital tracking loops”, Annals of Telecommunications, vol. 64, nos. 9–10, pp. 601–614, 2009, doi: 10.1007/s12243-009-0114-1.
117 M. L. Psiaki, “Block acquisition of weak GPS signals in software receiver”, ION GPS 2001, 2001.
118 P. D. Groves, Principles of GNSS, Inertial, and Multisensor Integrated Navigation Systems, 2nd ed. Boston, MA, USA: Artech House, 2013.
119 M. Petovello, “Real-time integration of a tactical-grade IMU and GPS for high-accuracy positioning”, UCGE Report 20209, Univ. of Calgary, 2003.
120 P. Misra and P. Enge, Global Positioning System: Signals, Measurements, and Performance, 2nd ed., 2011.
121 A Bjorck, Numerical Methods for Least Squares Problems. Philadelphia, PA, USA: SIAM, 1996.
122 G. H. Golub and C. F. Van Loan, Matrix Computations, 3rd ed. Baltimore, MD, USA: Johns Hopkins Univ. Press, 1996.
123 A. Angrisano, L. Ferrigno, S. Gaglione, G. Miele, and K. Velusamy, "GNSS–Based Velocity Measurement for Smart Mobility Systems," 2024 IEEE International Symposium on Measurements & Networking (M&N), Rome, Italy, 2024, pp. 1-6, doi: 10.1109/MN60932.2024.10615589.
124 R. M. Savithramma, B. P. Ashwini and R. Sumathi, "Smart Mobility Implementation in Smart Cities: A Comprehensive Review on State-

of-the-Art Technologies," 2022 4th International Conference on Smart Systems and Inventive Technology (ICSSIT), Tirunelveli, India, 2022, pp. 10-17, doi: 10.1109/ICSSIT53264.2022.9716288.

125 F. Moura and J.de Abreu e Silva, “Smart Cities: Definitions, Evolution of the Concept and Examples of Initiatives”, in Smart cities: Concepts, Methodologies, Tools and Applications, Cham, Switzerland: Springer, 2021, ch. 6, doi: 10.1007/978-3-319-95873-6_6.

126 G. Pau, T. Campisi, A. Canale, A. Severino, M. Collotta, and G. Tesoriere, “Smart pedestrian crossing management at traffic light junctions through a fuzzy-based approach,” Future Internet, vol. 10, no. 2, Art. no. 15, 2018, doi: 10.3390/fi10020015.

127 R. M. Savithramma and R. Sumathi, “Road traffic signal control and management system: A survey,” in Proc. 3rd Int. Conf. Intelligent Sustainable Systems (ICISS), 202, pp. 104–110, 2020, doi: 10.1109/ICISS49785.2020.9315970.

128 European GNSS Service Centre (GSC), “EGNOS and Galileo for ITS and Road Transport”, version 01.00, 2017.

129 O. Jafari, S. Kolosov, N. Vo, A. T. Magar, J. Heikkonen, and R. Kanth, "Intelligent Traffic Light Solution for Green and Sustainable Smart City," 2023 12th Mediterranean Conference on Embedded Computing (MECO), Budva, Montenegro, 2023, pp. 1-5, doi: 10.1109/MECO58584.2023.10154954.

130 M. S. Ali Muthanna, Y. T. Lyachek, A. M. Obadi Musaeed, Y. Ahmed Hazzaa Esmail, and A. B. M. Adam, "Smart System of a Real-Time Pedestrian Detection for Smart City," 2020 IEEE Conference of Russian Young Researchers in Electrical and Electronic Engineering (EIConRus), St. Petersburg and Moscow,

Russia, 2020, pp. 45-50, doi: 10.1109/EIConRus49466.2020.9039333.

131 A. Kanungo, A. Sharma, and C. Singla, "Smart traffic lights switching and traffic density calculation using video processing," 2014 Recent Advances in Engineering and Computational Sciences (RAECS), Chandigarh, India, 2014, pp. 1-6, doi: 10.1109/RAECS.2014.6799542.

132 S. Ransubhe, M. A. Mughni, C. R. Shiralkar, and B. Ratnaparkhi, "Smart Traffic Light Switching and Traffic Density Calculation Model using Computer Vision," 2023 IEEE 8th International Conference for Convergence in Technology (I2CT), Lonavla, India, 2023, pp. 1-5, doi: 10.1109/I2CT57861.2023.10126240.

133 Q. Liu, R. Ying, Z. Dai, Y. Wang, J. Qian, and P. Liu, “Multi-phase fusion for pedestrian localization using mass-market GNSS and MEMS sensors”, Sensors, vol. 23, no. 7, Art. no. 3624, 2023.

134 V. Gikas and H. Perakis, “Rigorous performance evaluation of smartphone GNSS/IMU sensors for ITS applications”, Sensors, vol. 16, no. 8, Art. no. 1240, 2016.

135 L. Ji, R. Sun, Q. Cheng, and J. Wang, “Evaluation of the performance of GNSS-based velocity estimation algorithms”, Satellite Navigation, vol. 3, no. 1, p. 18, 2022.

136 P. Freda, A. Angrisano, S. Gaglione, and S. Troisi, “Time-differenced carrier phase technique for precise GNSS velocity estimation,” GPS Solutions, vol. 19, no. 2, pp. 335–342, 2015.

137 M. A. Sturza, “Navigation System Integrity Monitoring Using Redundant Measurements,” Navigation, vol. 35, no. 4, pp. 483–501, 1988.

138 Broadcom Inc., “BCM47531: GNSS/GPS SoCs”, Broadcom.

139 P. J. G. Teunissen and O. Montenbruck, Eds., Springer Handbook of "Global Navigation Satellite System", Cham, Switzerland: Springer, 2017.

140 Broadcom Inc., "BCM4775X: GNSS receiver with integrated sensor hub", Broadcom

141 A. Angrisano, G. Cappello, S. Del Pizzo, and S. Gaglione, "Time-Differenced Carrier Phase Technique for Precise Velocity Estimation on an Android Smartphone," Sensors, vol. 22, no. 21, Art. no-8514. 2022.

142 R. Hatch, "The synergism of GPS code and carrier measurements", in Proc. 3rd Int. Geodetic Symposium Satellite Doppler Positioning, New Mexico State University, 1983, vol. 2, pp. 1213-1232.

143 A. Bernieri, G. Iannitti, M. Laracca, G. Miele, and S. Sangiovanni, "A test bed for in-laboratory calibration of optical-based speedometers," in 2023 IEEE International Instrumentation and Measurement Technology Conference (I2MTC), 2023, pp. 1–6.

144 S. Hewitson and J. Wang, "GNSS Receiver Autonomous Integrity Monitoring (RAIM) for multiple outliers", European Journal of Navigation, vol. 4, 2006.

145 United Nations, "Sustainable Development Goal 11: Make cities inclusive, safe, resilient and sustainable", UN Department of Economic and Social Affairs (UN DESA).

146 United Nations, "SDG Target 11.2: Access to safe, affordable, accessible and sustainable transport systems", UN DESA.

147 A. Pompigna and R. Mauro, "Smart roads: A state of the art of highway *innovations in the Smart Age*", Engineering Science and Technology, an International Journal, vol. 25, art. 100986, 2022.

148 A. K. M. H. Hossein, A. Golroo, and M. Akhoundzadeh, "*Smart embedded technologies and materials for enhanced pavement*

*management systems: A review*," Construction and Building Materials, vol. 168, art. 105865, 2024.

149 A. Di Graziano, V. Marchetta, and S. Cafiso, "*Structural health monitoring of asphalt pavements using smart sensor networks: A comprehensive review*," Journal of Traffic and Transportation Engineering (English Edition), vol. 7, no. 5, pp. 639–651, 2020.

150 O. Arshi, and S. Mondal, "Advancements in sensors and actuators technologies for smart cities: a comprehensive review", Smart Construction and Sustainable Cities, vol. 1, 2023.

151 S. Trubia, A. Severino, S. Curto, F. Arena, and G. Pau, "Smart Roads: An overview of what future mobility will look like", Infrastructures, vol. 5, no. 12, p.107, 2020.

152 D. Oladimeji, K. Gupta, N. A. Kose, K. Gundogan, L. Ge, and F. Liang, "Smart Transportation: An Overview of Technologies and Applications," *Sensors*, vol. 23, 2023.

153 M. Barriera, S. Pouget, B. Lebental, and J. V. Rompu, "*In Situ Pavement Monitoring: A Review*", Infrastructures, vol. 5, no. 2, art. 18, 2020.

154 Anas S.p.A., "Smart Road and Smart mobility", Anas – Innovation and Research.

155 Global Infrastructure Hub. " ANAS Smart Road Project", Quality Infrastructure Database, Jan. 2021.

156 A. H. Alavi, P. Jia, W. Buttlar, and N. Lajnef, "Internet of Things-Enabled Smart Cities: State-of-the-Art and Future Trends". Measurement, vol. 129, pp. 589-606, 2018.

157 A Hadj-Attou, Y. Kabir, and F. Ykhelf, "IoT-Based Road Surface Condition Monitoring Using Spatiotemporal Feature Learning", in Advances in Computing Systems and Applications, Springer, 2024, pp 245-254.

158 K. Micko, P. Papcun and I. Zolotova, “Review of IoT sensor systems used for monitoring the Road Infrastructure”, Sensors, vol. 23, no. 9, Art. no. 4469, 2023.

159 L. S. Furtado, I. S. Bessa, N. O. Gurjao, and J. B. Soares, “*Integrating smart city technologies for sustainable pavement infrastructure*”, Canadian Journal of Civil Engineering, vol. 52, no. 5, 2025.

160 UNESCO World Heritage Centre, “Historic Centre of Florence”, UNESCO, 2024.

161 A. Moropoulou, K. Labraopoulos, E. Delegou, M. Kaoglou, and A. Bakloas, “Non-destructive techniques as a tool for the protection of built cultural heritage”, Construction and Building Materials, vol. 48, pp. 1222-1239, 2013.

162 ICOMOS, “Principles for the Analysis, Conservation and Structural Restoration of the Architectural Heritage”, ICOMOS, Paris, 2003.

163 UNESCO World Heritage Centre, “Operational Guidelines for the Implementation of the World Heritage Convention”, 2021.

164 A. Shtayat, S. Moridpour, B. Best, A. Shroff, and D. Raol, “*A review of monitoring systems of pavement condition in paved and unpaved roads,*” *Journal of Traffic and Transportation Engineering (English Edition)*, vol. 7, no. 5, pp. 629–638, 2020.

165 F. D'Amato, P. Gamba and E. Goldoni, “Monitoring heritage buildings and artworks with Wireless Sensor Networks”, 2012 IEEE Workshop on Environmental Energy and Structural Monitoring Systems (EESMS), Perugia, Italy, 2012, pp. 1-6

166 G. Betta, D. Capriglione, L. Ferrigno, G. Miele and K. Velusamy, "*On the Feasibility of LoRaWAN Communication in a Smart Road Sensor Network*," 2025 IEEE International Workshop on Metrology for Automotive (MetroAutomotive), Parma, Italy, 2025, pp. 103-108.

167 Bosch Sensortec GmbH, BME280 Data Sheet, document no. BST-BME280-DS001-23, rev. 1.23, Jan. 2022.

168 C. Han, P. Seshadri, Y. Ding, N. Posner, B. W. Koo, A. Agarwal, A. Lerch, and S. Guhathakurta, "*Understanding pedestrian movement using urban sensing technologies: the promise of audio-based sensors*", Urban Informatics, vol. 3, no. 1, 2024.

169 S. Liu, C. Higgs, J. Arundel, G. Boeing, N. Cerdera, D. Moctezuma, E. Cerin, D. Adlakha, B. Giles-Corti, and M. Lowe, "*A generalised framework for measuring pedestrian accessibility around the world using open data*," Geographical Analysis, vol. 54, no. 3, 2022.

170 R.Schneider, L Arnold, and D. Ragland, "*A methodology for counting pedestrians at intersections: Using automated counters to extrapolate weekly volumes from short manual counts,*" Transportation Research Record: Journal of the Transportation Research Board, vol. 2140, 2009.

171 L. H. Barrero-Solano, A. Sánchez-Pilonieta, A. Forero-Guzmán, J. A. Quiroga-Sepúlveda, N. S. Romero-Barreto, F. C. Calderon-Bocanegra, S. Felknor, and L. A. Quintana-Jiménez, "*Video-based assessment of pedestrian behaviour: Development and testing of methods*", Revista de Salud Publica, vol. 19, no. 2, pp. 182-187, 2017.

172 U. Gawande, K. Hajari, and Y. Golhar, "*Pedestrian Detection and Tracking in Video Surveillance System: Issues, Comprehensive Review, and Challenges*," IntechOpen, 2020.

173 R. Hoffmann, H. Brodowski, A. Steinhage, and M. Grzegorzek, "*Detecting Walking Challenges in Gait Patterns Using a Capacitive Sensor Floor and Recurrent Neural Networks*" Sensors, vol. 21, no. 4, 2021.

174 Espressif Systems, ESP32-S3-WROOM-1 & ESP32-S3-WROOM-1U Datasheet.

175 J. O. Agyemang, J. J. Kponyo, J. D. Gadze, H. N. Mensah and D. Yu, "*A Lightweight Messaging Protocol for Internet of Things (IoT) Devices*," Technologies, vol. 10, no. 1, art. 21, 2022.

176 N. S. Alotaibi, H. I. Sayed Ahmed, S. O. M. Kamel, G. F. ElKabbany, "*Secure Enhancement for MQTT Protocol Using Distributed Machine Learning Framework*", Sensors, vol. 24, no.5, art. 1638, 2024.

177 C. D'Ortona, D. Tarchi, and C. Raffaelli, "*Open-Source MQTT-Based End-to-End IoT System for Smart City Scenarios*", Future Internet, vol. 14, no. 2, art. no. 57, 2022.